

Pressure induced phase transitions in PbTiO_3

Muhtar Ahart (maihaiti@ciw.edu), Maddury Somayazulu, Ho-kwang Mao,
R. J. Hemley, R. E. Cohen
Carnegie Institution of Washington
5251 Broad Branch Rd., NW, Washington DC 2005

First-principles computations[1, 2] reveal that lead titanate PbTiO_3 (PT), one of the simplest ferroelectrics with the perovskite structure, undergoes successive phase transitions from tetragonal to monoclinic to rhombohedral under pressure at low temperatures. To confirm such phase transition indeed occur in PT, we employed the high-energy high resolution and energy dispersive x-ray diffractions (APS, Argonne National Laboratory) to investigate the lead titanate behavior under pressure at 10 K.

The powder samples of lead titanate were loaded into stainless steel gaskets in a diamond anvil cell (DAC) with neon as the pressure medium. In addition, small ruby chips, and Au powder were loaded together with samples for pressure determination. The DAC was loaded into a cryostat for low temperature measurements at 10 K. Figure 1 shows the typical energy dispersive diffraction pattern at selected pressures. It exhibits major changes in Bragg peak intensities around 10, 16 and 20 GPa, respectively. This indicates the presence of structural phase transitions at these pressures. Additional high-energy high-resolution angular dispersive diffraction experiments confirmed such changes. In Fig. 2, we show the data obtained from our high-resolution diffraction scans. The fits to the data are made by constraining the peak widths using the gold pressure standard. The results allow us to distinguish the specific characteristics of each phase. In particular, the monoclinic phase exhibits unique features that cannot be accounted for by either of the other phases. The monoclinic phase in fact exists from 10 to 16 GPa.

Comparison of our experimental results with the theoretical calculations of Wu and Cohen [1] brings out several interesting features. These authors calculated the free energy differences between tetragonal, monoclinic, and rhombohedral phases of PT as a function of pressure, at 0 K. They found that the tetragonal phase is most stable below 10 GPa, the monoclinic phase has lowest free energy between 10 and 12 GPa, and the rhombohedral phase is the stable phase above 12 GPa. Our experimental results show that below 10 GPa, the $\langle 100 \rangle$ and $\langle 110 \rangle$ Bragg peaks exhibit tetragonal distortion consistent with the low pressure phase of lead titanate. The tetragonal to monoclinic phase transition takes place around 10 GPa. The high-resolution x-ray diffraction results show splitting of (110) Bragg peak into a triplet between 10 and 16 GPa. Such a splitting is consistent with the monoclinic distortion.

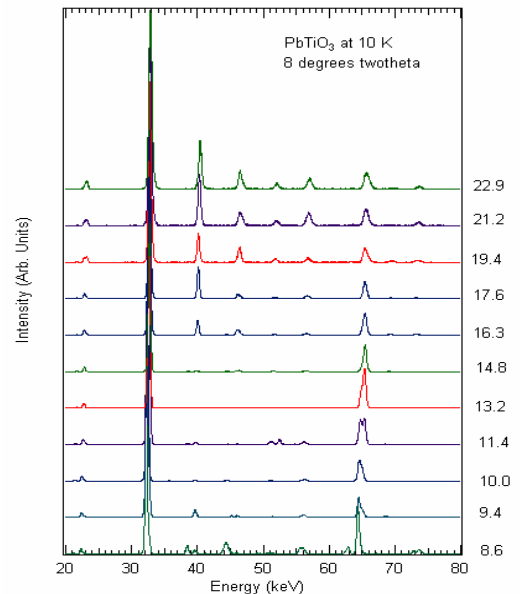


Fig. 1. Energy dispersive x-ray diffraction spectra at selected pressure.

Experimentally, the rhombohedral ($R3m$) distortion appears in the diffraction pattern above 16 GPa. Our recent Raman scattering measurements indicate that rhombohedral $R-3c$ is more favorable above 20 GPa.

At ambient pressure, lead titanate has a free energy with minima along $\pm[001]$ and along the 8 $[\pm 1\pm 1\pm 1]$ directions, with the $\pm[001]$ being deepest due to the large lattice strain. Under pressure the spontaneous strain decreases, and the minima become shallower, leading to a series of phase transitions. Thereby a morphotropic phase boundary arises in PT under pressure at low temperatures and consequently the polarization can easily rotate between different symmetries.

In conclusion, x-ray diffraction experiments revealed that PT undergoes a successive phase transitions from tetragonal to monoclinic at 10 GPa, monoclinic to rhombohedral ($R3m$) at 16 GPa, and rhombohedral ($R3m$) to rhombohedral ($R-3c$), at 20 GPa. These findings will have broad implications in the field of ferroelectrics. For example, the MPB with monoclinic symmetry is a common feature in the

compositional phase diagram of relaxor ferroelectrics such as PZN-PT, or PZT. This feature can be readily understood from the lead titanate phase diagram. Since lead titanate itself possesses the monoclinic phase in its P-T phase diagram, when it is mixed with other compounds, relaxor ferroelectric phases such as PMN or PZN or PZO are realized. The second component plays the role of chemical pressure, which tunes the transition temperature to room temperature. In addition, the large lattice strain in lead titanate results in superior piezoelectric properties in these materials.

This work was sponsored by the Office of Naval Research under Grants No. N00014-02-1-0506, N00014-97-1-0052, and N00014-99-1-0738. Support also was received from the Carnegie/Department of Energy Alliance Center (CDAC, DE-FC03-03NA00144).

References:

1. Z. Wu, and R. E. Cohen, Phys. Rev. Lett., **95**, 37601 (2005).
2. I. A. Kornev, L. Bellaiche, P. Bouvier, P.-E. Janolin, B. Dkhil, and J. Kreisel, Phys. Rev. Lett., **95**, 196804 (2005).

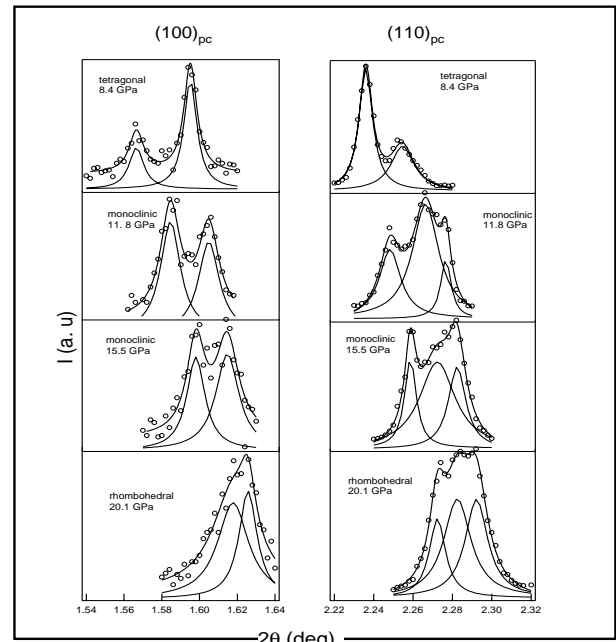


Fig. 2. (001) and (110) Bragg peaks from high-energy high-resolution beam line. Points are data and solid lines are fit.

Ferroelectric Nanoscale Domain Structures computed by Finite Element

D. Albrecht^{1,2}, D. Aubry², L. Bellaïche³, B. Dkhil¹

¹Laboratoire Structures, Propriétés et Modélisation des Solides (SPMS), UMR CNRS 8580

²Laboratoire de Mécanique des Sols Structures et Matériaux (MSSMAT), UMR CNRS 8579, Ecole Centrale Paris, 92295 Châtenay-Malabry Cedex, France

³Department of Physics, University of Arkansas, Fayetteville, Arkansas 72701, USA

Phone : +33 1 41 13 15 06; Fax : +33 1 41 13 14 37; e-mail: david.albrecht@ecp.fr

Physicals properties of ferroelectric materials mainly arise from the fact that the polarization is strongly influenced by strain and/or electrical boundary conditions -- which may change its orientation and magnitude. At small scales, this influence is even stronger and unusual domain-like structures are produced (vortices, stripes, etc...). For the calculation of domain structures, at small scales, Hamiltonian-based models are widely used whereas at higher scales, continuum model are predominant [1]. Nevertheless, in between there is no computational method connecting both scales. Therefore our goal is to develop and build new approaches in order to bridge these two separated scales.

Our model stems from classical Hamiltonian phenomenological formulation [2] where the total energy is separated into five terms as follows.

$$E\{u, \varepsilon\} = E^{Self}\{u, \varepsilon\} + E^{elas}\{u, \varepsilon\} + E^{int}\{u, \varepsilon\} + E^{Short}\{u\} + E^{dipole-dipole}\{u\}$$

Where u and ε are the local mode and the elastic deformation respectively. Each energy term is then formulated through a continuous description. Difficulties arise from short and long range terms that are non local, since in this approach solvers are optimized for local terms. The short term interaction energy is transformed via an equivalent partial differential equation [3] which gives rise to two terms: a gradient and a local dependency as:

$$E^{Short}(u) = K_1.u \otimes u + (G. \nabla u \otimes \nabla u)$$

On the other hand, the electrostatic long-range energy is formulated using its similarity with the Maxwell description of the electrostatic field. The difference between both descriptions is a classical Lorentz local field. Again the local long range part of the energy may be expressed by the sum of a gradient of a potential and a local dependency as:

$$E^{Dipole-Dipole}(u) = -u. \nabla V + L.u \otimes u$$

where $4.\pi. \nabla V = \int_{R^3} \frac{Z^{*2}}{\epsilon^\infty} \cdot \frac{uj - 3.d.(uj.d)}{|d|^3} dVol(uj)$

allowing a suitable expression of the potential V for a continuum space computation.

Finally within a variational principle, we can easily compute the total energy description in the continuum space by using finite elements. The equations introduced are:

$$\begin{aligned} \nabla.(G. \nabla u) - (K_1+L).u - A.u \otimes u \otimes u \otimes u - Q.u \otimes \varepsilon + E^{applied} - \nabla V &= \mu \partial u / \partial t \\ \nabla.(C. \varepsilon - I/2.Q.u \otimes u) &= 0 \\ \nabla.(-\epsilon \nabla V + u) &= 0 \end{aligned}$$

And the free boundary conditions are:

$$\begin{aligned} n.(G. \nabla u) &= 0 \\ n.(C. \varepsilon - 1/2. Q. u \otimes u) &= 0 \\ n.(-\varepsilon \nabla V + u) &= 0 \end{aligned}$$

All the coefficients are taken from *ab-initio* computation. K_I which comes from the short interactions appears then to be positive. On the other side L which comes from the long range part is negative. We therefore reconstructed a Landau-like model [4].

With such approach, starting from a nanoscale computation and expanding its size to access to the domain organization, changes can be easily done with finite elements. Preliminary results are very promising since we are already able to obtain the vortices obtained by atomistic Hamiltonian calculations [5] with this presently proposed approach (see fig. 1)

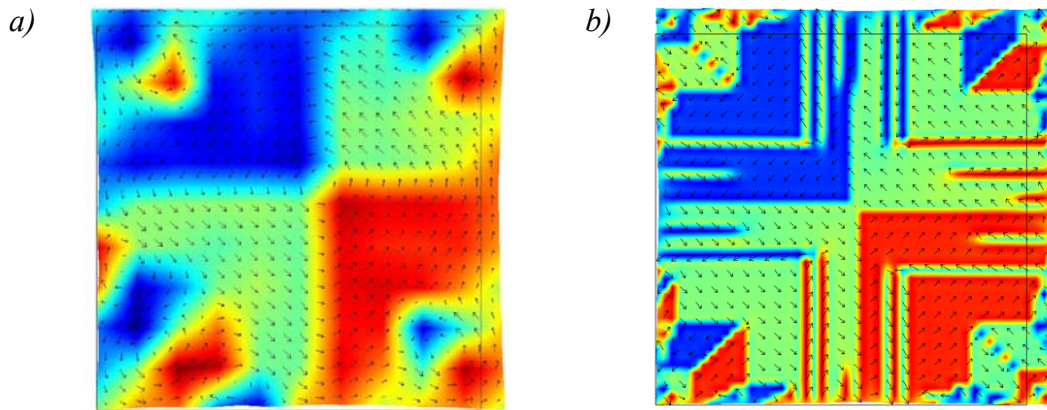


Fig 1 – 0K simulation of BTO dots after a relaxation from a up down initial configuration and free boundary conditions. Arrows and colors are related to the local mode. a) is for 10x10 cells and b) for 50x50 cells.

In this presentation, we will show our recent results obtained for both dots and thin films. This original approach will be illustrated by the case of different boundary conditions, such as stress originating from a substrate, electrodes or free conditions. The influence of different scales on the ferroelectric domain pattern will also be discussed.

References

- [1] Su, Y. and C.M. Landis, *Continuum thermodynamics of ferroelectric domain evolution: Theory, finite element implementation, and application to domain wall pinning*. Journal of the Mechanics and Physics of Solids, 2007. **55**(2): p. 280.
- [2] Zhong, W., D. Vanderbilt, and K.M. Rabe, *First-principles theory of ferroelectric phase transitions for perovskites: The case of BaTiO₃*. Physical Review B (Condensed Matter), 1995. **52**(9): p. 6301.
- [3] R. D. Mindlin, *Elasticity, piezoelectricity and crystal lattice dynamics*. Journal of Elasticity, 1972. v. 2, p. 217-282.
- [4] Zhang, W. and K. Bhattacharya, *A computational model of ferroelectric domains. Part I: model formulation and domain switching*. Acta Materialia, 2005. **53**(1): p. 185.
- [5] Naumov, I., L. Bellaiche and H. Fu *Unusual phase transitions in ferroelectric nanodisks and nanorods*. Nature (London), 2004, **432**: p. 737.

Experimental Evidence of Ferroelectricity in BaTiO₃ Films Below 10 Layers

A.P. Baddorf,¹ Junsoo Shin,^{1,2} V.B. Nascimento,^{1,2} A.Y. Borisevich,¹ E.W. Plummer^{1,2} and
S.V. Kalinin¹

¹Oak Ridge National Laboratory, Oak Ridge, TN 37831

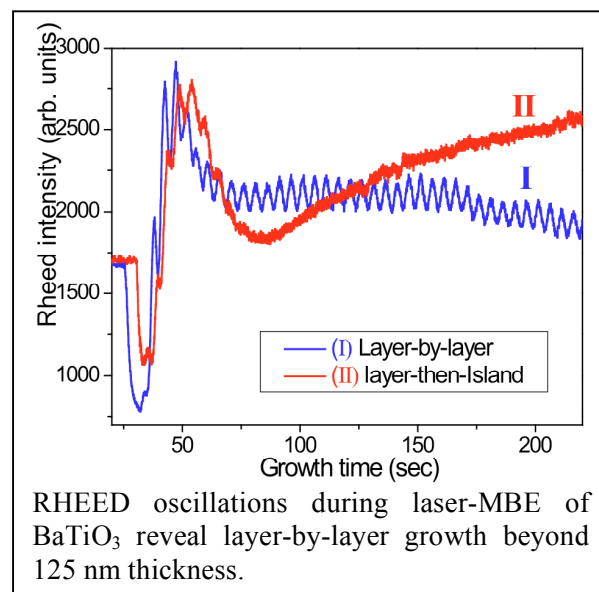
²The University of Tennessee, Knoxville, TN 37996

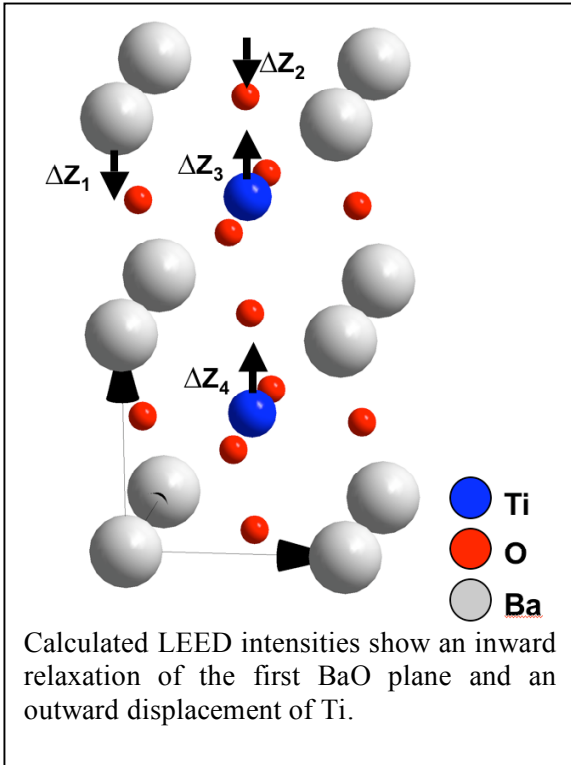
phone: 865 574-5241; fax: 865 574-1753; e-mail: baddorfap@ornl.gov

Predictions for the minimum critical film thickness for ferroelectricity have continuously decreased, reflecting new understanding of ferroelectric domains and cultivating hopes for terabit data storage. For BaTiO₃, ferroelectricity has previously been observed experimentally down to 12 layers and predicted by first-principles calculations in 6 layer films. We have examined BaTiO₃ ultra-thin films grown on SrRuO₃/SrTiO₃ using laser-MBE in high oxygen pressures and report evidence of a ferroelectric state at room temperature by in-situ characterization of structure, using low energy electron diffraction (LEED I-V) and by scanning tunneling spectroscopy (STS).

High quality, low defect films of BaTiO₃ on SrTiO₃ are difficult to produce due to a large lattice mismatch (2.28%) which promotes Stranski-Krastanov growth and islanding. Layer-by-layer growth has been achieved with low background oxygen pressures (i.e. below 1 mTorr), but films probably have oxygen vacancies. We have achieved layer-by-layer growth at 10 mTorr oxygen pressures by employing rapid island nucleation with laser ablation and suppressing island formation kinetically with an average growth rate (0.2 ML/s) higher than previously employed. This approach has allowed us to grow BaTiO₃ films on SrTiO₃ beyond 125 nm, with RHEED oscillations for each layer, and with AFM and STEM revealing low roughness and defect density respectively.

We have employed these growth conditions to produce high quality, ultrathin layers of BaTiO₃ on a thin (10-20 nm) conducting layer of SrRuO₃ on a SrTiO₃ substrate. Films produce sharp (1x1) LEED patterns, indicating a well-ordered tetragonal phase structure. Observed intensities of 8 independent diffraction beams from 4 and 10 layer films at 130 and 300 K were compared to calculated intensities between electron energies between 40 and 380 eV. Best fits were obtained for a model with the





outermost Ba-O plane relaxed inward and the central Ti atom displaced outward, corresponding to a polarization consistent with compressive strain. The intensities are not consistent with a centrosymmetric or laterally displaced Ti.

Ferroelectricity, that is reversible polarization switching, below 10 ML is suggested by abrupt transitions in local tunneling I-V in STM spectroscopy.

Electron tunneling into or out of the BaTiO₃ films follows smooth, continuous I-V characteristics except at +/- 2.5 V where the current jumps discontinuously. A discontinuity is consistent with a voltage dependent polarization change in the film.

Research was sponsored by the Division of Materials Sciences and Engineering and the Center for Nanophase Materials Sciences, Office of Basic Energy Sciences, U.S. Department of Energy with Oak Ridge National Laboratory, managed and operated by UT-Battelle, LLC.

Controlling Polarization Dynamics by Piezoresponse Force Microscopy in a Liquid Environment: Transition from Localized to Macroscopic Switching

Brian J. Rodriguez, Stephen Jesse, A. P. Baddorf, and Sergei V. Kalinin¹

Materials Science and Technology Division and The Center for Nanophase Materials Sciences, Oak Ridge National Laboratory, Oak Ridge, TN 37831

In the last decade, Piezoresponse Force Microscopy (PFM), based on direct probing of local electromechanical coupling in a piezoelectric material using a periodically biased tip,^{1,2} has emerged as a powerful tool for the characterization of ferroelectric materials. Application of a positive (negative) dc bias pulse to a conductive PFM tip in contact with a positively (negatively) polarized domain, results in a highly-localized electric field, which induces the nucleation and subsequent growth of a domain of opposite polarization. Measurements of domain radii as a function of the amplitude and duration of voltage pulses yields domain growth kinetics and bias dependence of the domain wall velocity. When performed in ambient, the rapid $1/r$ decrease of the electric field with distance from the tip-surface junction results in the nucleation of a single domain located below the tip. In other words, due to the high field concentration, the tip acts as the dominant nucleation center. When the switching field is nearly uniform, as is the case in PFM measurements of ferroelectric capacitors, defects are thought to act as nucleation centers. However, in this case the spatial resolution is limited and the switching behavior is strongly mediated by the presence of the top electrode and macroscopic strain fields, which hinders the conclusive identification of defect sites.

Here, we explore PFM imaging and polarization dynamics in a liquid environment as a means to control the mechanism of the switching process. Previously, we have demonstrated PFM *imaging* in liquid, which in certain cases enables high spatial resolutions approaching that of the intrinsic domain wall width. This is made possible by mobile ions within the solution that screen the ac tip bias at high frequencies and thus minimize electrostatic interactions.³ Here, we explore the effects of the conductive properties of the liquid on the switching behavior by using alcohols with variable alkyl chain lengths to control the concentration and diffusion length of the mobile ions and thereby vary the spatial extent of the potential distribution in the solution, and hence spatial distribution of electric field in the film.

In an ambient or non-polar liquid environment, the biased tip establishes a highly-localized electric field that decays rapidly with distance from the tip-surface junction. This field results in highly localized polarization switching above a certain threshold value, generating well-defined 2D domains that grow in area with time and pulse length, Fig. 1(a). In this case, domain dimensionality is controlled by the field structure and is unaffected by large-scale disorder. In liquid, the PFM contrast is strongly mediated by the presence of mobile ions that result in an increase of the effective area affected by the tip field. For solvents with intermediate polarities, the electric field is localized to the tip surface junction, but the characteristic length scale is significantly larger than the tip size and is mediated by pulse length via the mobile ion diffusion length. The switching in this case results in the formation of irregular fractal domains with scale-dependent dimensionality determined by the relationship between the domain size and characteristic length scale of the frozen disorder,

¹ Corresponding author, sergei2@ornl.gov

Fig. 1 (b). In conductive solvents, the solution is uniformly biased, resulting in a homogeneous electric field across the film thickness (similar to ferroelectric capacitors), as shown in Fig. 1 (c). In this non-local case, switching is dominated by the frozen disorder in the film, since the driving force for switching is independent on the position of the tip. Variation of the pulse length and magnitude in this case allows the regions where the switching is most likely to happen, i.e. the nucleation centers, to be visualized. The evolution of the switching mechanism with solvent and bias parameters is illustrated in Fig. 1 (d). Notably, high resolution *imaging* is possible even in polar solvents because of the much higher excitation frequencies, minimization of the diffusion paths, and high localization of the strain that transmit predominantly through the mechanical (rather than electrical) contact area. This allows *imaging* domains independently on whether the switching is non-local or local.

PFM switching in liquids provides novel opportunities for high-resolution studies of polarization dynamics and the dimensionality of the switching process, and the role of disorder on polarization reversal, ultimately providing insight into the spatial distribution of nucleation centers and the interplay between domain growth and frozen and thermal disorder.

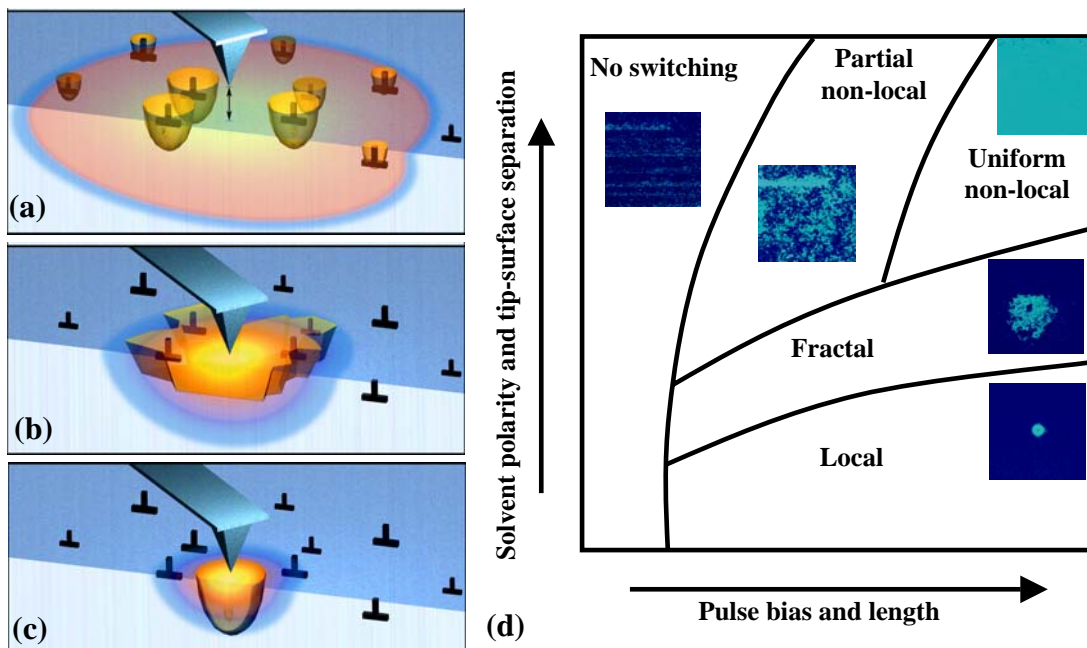


Fig. 1. Schematics of switching in (a) local, (b) fractal, and (c) non-local cases. Depending on the characteristic spatial extent of electric field vs. length scale of disorder, local, non-local, fractal, and partial and uniform non-local switching regimes are possible. (d) Schematic parameter diagram of possible switching mode vs. solvent nature and pulse parameters.

Research supported by the U.S. Department of Energy Office of Basic Energy Sciences Division of Materials Sciences and Engineering at Oak Ridge National Laboratory operated by UT-Battelle, LLC.

References

- ¹ P. Günther and K. Dransfeld, *Appl. Phys. Lett.* **62**, 1137 (1992).
- ² M. Alexe and A. Gruverman (Ed.), *Nanoscale Characterization of Ferroelectric Materials*. Springer, Berlin, Germany, 2004.
- ³ B.J. Rodriguez, S. Jesse, A.P. Baddorf, and S.V. Kalinin, *Phys. Rev. Lett.* **96**, 237602 (2006).

DIELECTRIC BEHAVIOUR OF NANOGRAIN PMN POWDERS

Juras Banys¹, Robertas Grigalaitis¹, Maksim Ivanov¹, Julie Carreaud², J.M. Kiat^{2,3}

¹Laboratory of Phase Transitions Dielectric Spectroscopy, Faculty of Physics, Vilnius University, 9 Sauletekio str., 10222 Vilnius, Lithuania

²Laboratoire Structures, Propriétés et Modélisation des Solides, Ecole Centrale Paris, Grande Voie des Vignes 92295 Chatenay-Malabry Cedex, France

³Laboratoire Léon Brillouin, CE Saclay, 91191 Gif-sur-Yvette Cedex, France

Phone : +37052366001 ; FAX: 37052366003; e-mail: juras.banys@ff.vu.lt

The anomalies in the physical properties of nanomaterials, namely nanoparticle powders, nanograin ceramics and thin films are attracting great interest due to numerous current and potential applications of ferroelectrics materials in the modern technology and engineering. The most important size effect for ferroelectric nanomaterials is known as vanishing of transition from ferroelectric phase to paraelectric one at some critical size. Despite the attempts to describe this phenomenon by various models no conclusive results has been achieved so far and size effect attracts a great attention to scientists not only as technological but also as a fundamental physical problem.

Pb(Mg_{1/3}Nb_{2/3})O₃ (PMN) is a well known relaxor ferroelectric exhibiting a huge, diffusive anomaly of dielectric permittivity around the room temperature. Although the dielectric properties of bulk PMN are widely studied, there is a lack of information about nanograin PMN properties. Since the pioneering work of Papet et al. [1], only one recent study on reduction of size in powder and ceramics has shown a vanishing of dielectric relaxation as the size of the grains reaches typical sizes of the polar nanoregions (PNRs) [2]. To explore the dielectric properties of nanograin PMN we performed dielectric permittivity studies of several PMN nanopowders with different mean grain size from 15 nm to about 1000 nm (Fig. 1). Obtained dielectric spectra for all grain sizes of nanopowders show peaks of dielectric permittivity at lower temperatures than bulk crystal [3]. The decrease of region of dielectric dispersion is evident when reducing the grain size of nanopowders from 143 nm to 38 nm and almost disappears in 15 nm grain size nanopowders. This result in good agreement with previous works [1,2] can be attributed to the weakening of the correlation between PNRs whose size reaches the size of the grain as it diminishes. The size dependence of maximum value of dielectric permittivity extracted from these results at 1.2 kHz frequency (Fig. 2) shows the almost linear decrease from bulk crystal to about 64 nm (except 1000 nm). The sharp drop of T_{\max} is observed when the size of nanopowders diminishes below 64 nm. The possible explanation of such behaviour can be the decrease of PNRs itself (not only the correlation between these) due to the decrease of grains of nanopowders. This is confirmed by the vanishing of the dipole freezing temperature (Fig. 3) obtained from fitting of the frequency dependences of PMN nanopowders with Vogel-Fulcher relationship to almost 0 K.

References

- [1] Papet P. , Dougherty J.P. and ShROUT T.R., *J. Mater. Res.* **5**, 2902 (1990).
- [2] Carreaud J., Gemeiner P., Kiat J.M., Dkhil B., Bogicevic C., Rojac T., Malic B. *Phys. Rev. B* **72**, 174115 (2005).
- [3] Grigalaitis R., Banys J., Kania A. and Slodczyk A. *J. Phys. IV France* **128**, 127–131 (2005).

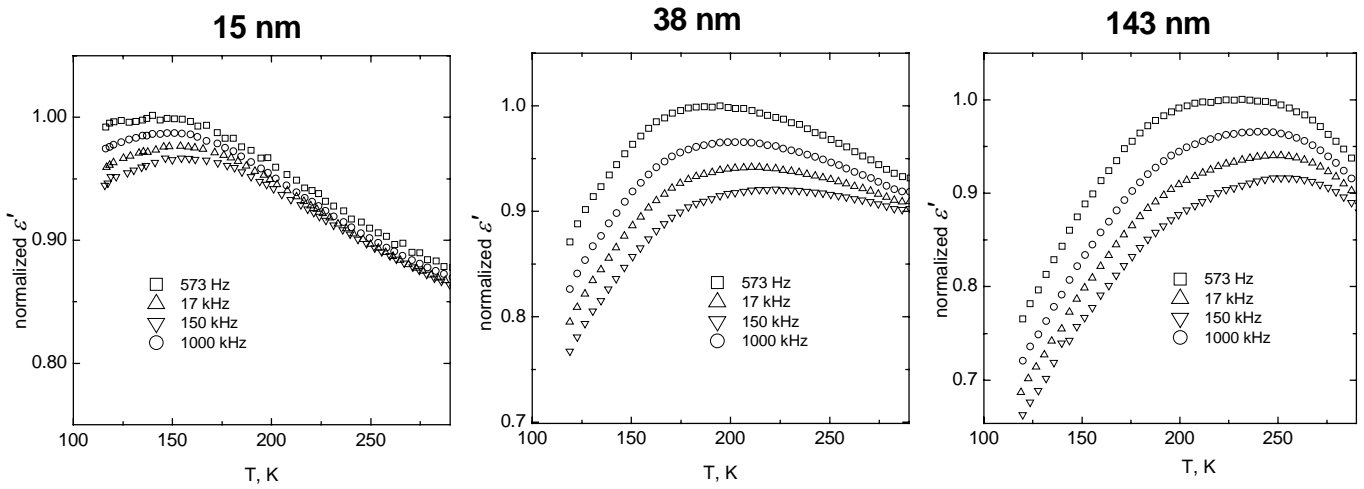


Fig. 1 Temperature dependence of dielectric permittivity (normalized to unity) at several different mean nanopowders sizes: 15nm (the left picture), 38nm (the center picture), 143nm (the right picture).

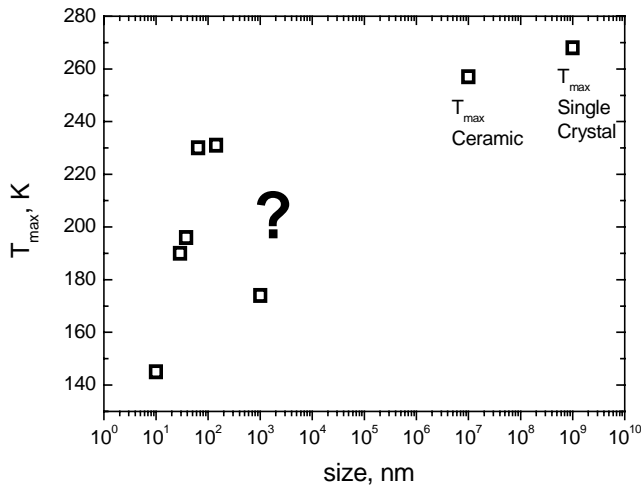


Fig. 2 The size dependence of maximum value of dielectric permittivity taken at 1.2 kHz frequency.

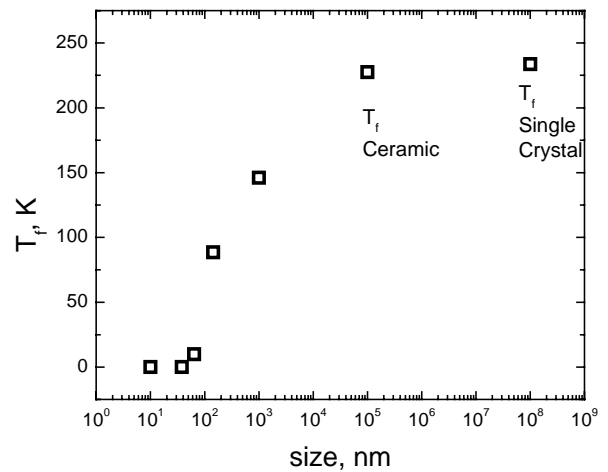


Fig. 3 The size dependence of the freezing temperature obtained from fitting the frequency dependences of PMN nanopowders with the Vogel-Fulcher relationship.

Novel depolarizing-field-induced phenomena in ferroelectric nanostructures

L. Bellaiche¹, I. Kornev¹, Bo-Kuai Lai¹, Sergey Lisenkov¹,
I. Ponomareva¹, Sergey Prosandeev¹, and R. Resta²

¹ *Physics Department, University of Arkansas,
Fayetteville, Arkansas 72701, USA*

² *Dipartimento di Fisica Teorica, Universit di Trieste,
strada Costiera 11, 34014 Trieste, Italy*

Ferroelectric nanostructures (FEN) are of increasing technological and fundamental interest because of the need in miniaturization of devices, as well as, the appearance of new phenomena (see, e.g., Ref. [1–6] and references therein). Unscreened polarization-induced charges at the surfaces/interfaces of FEN generate a depolarizing field that is now known to be responsible for some of these new phenomena. Examples are the existence of a critical thickness below which no ferroelectricity can appear [3] and the observation and prediction of laminar stripe nanodomains with exceptional small periodicity in ferroelectric thin films [2, 4]. Another example is the formation of a vortex structure for the electric dipoles in zero-dimensional ferroelectrics [5, 6]. Interestingly, the depolarizing field is very sensitive to many factors, including the shape and dimensionality of the FEN, as well as its surrounding. Furthermore, the depolarizing field dominates the polarization fluctuations, both thermal fluctuations (as considered here, see item 5 below) and quantum fluctuations (at $T=0K$ [7]). One may thus wonder if additional original phenomena remain to be discovered, as a result of depolarizing fields.

The purpose of this talk is to demonstrate (and understand via the development and use of first-principles-based approaches and analytical developments) that it is indeed the case. Examples of such phenomena, to be addressed here, are:

- 1) The formation of periodic stripe nanodomains in ferroelectric *superlattices*, and how the morphology of such nanodomains evolves under an external electrical field. A particular emphasis will be placed on how these nanodomains and their field-induced evolution differ from those of ferroelectric thin films.

- 2) The striking effect of *asymmetrical* screening at the surfaces/interfaces on the width and morphology of domains in ferroelectric thin films.
- 3) The existence of a new form of electromechanical coupling in ferroelectric nanodots.
- 4) The appearance of labyrinth structures in FEN.
- 5) Unusual features related to the static dielectric response of FEN, such as its possible *negative* sign and the modification of its analytical expression in terms of polarization's fluctuations when going from bulk to FEN.

This work is supported by ONR grants N00014-01-1-0365 and N00014-04-1-0413, by NSF grant DMR-0404335, and by DOE grant DE-FG02-05ER46188.

-
- [1] J. F. Scott and C. A. Paz de Araujo, *Science* **246**, 1400 (1989).
- [2] D.D. Fong, G.B. Stephenson, S.K. Streiffer, J.A. Eastman, O. Auciello, P.H. Fuoss and C. Thompson, *Science* **304**, 1650 (2004).
- [3] J. Junquera and P. Ghosez, *Nature* (London) **422**, 506 (2004).
- [4] I. Kornev, H. Fu and L. Bellaiche, *Phys.Rev. Lett.* **93**, 196104 (2004).
- [5] H. Fu and L. Bellaiche, *Phys. Rev. Lett* **91**, 257601 (2003).
- [6] I. Naumov and L. Bellaiche and Huaxiang Fu, *Nature* (London) **432**, 737 (2004).
- [7] R. Resta, *Phys. Rev. Lett.* **96**, 137601 (2006).

DFT models as a way to study Pd-doped BaCeO₃

Joseph W. Bennett^a, Jun Li^b, Udayshankar G. Singh^c, Susannah Scott^c and Ram Seshadri^b, Andrew M. Rappe^a.

(a) *The Makineni Theoretical Laboratories, Department of Chemistry,
University of Pennsylvania, Philadelphia, PA 19104-6323.*

(b) *Materials Department and Materials Research Laboratory,
University of California, Santa Barbara, CA 93106*

(c) *Department of Chemical Engineering and Department of Chemistry and Biochemistry,
University of California, Santa Barbara, CA 93106*

(Dated: January 14, 2007)

We use first-principles density functional theory (DFT) calculations to investigate the ground state structures of both BaCeO₃ and Pd-doped BaCeO₃ (BCP) perovskites for the first time. The DFT structure of these perovskites match closely with recent experimental studies. The possible oxidation state of Pd in each doped structure is investigated through a structural analysis, the results of which are supported by a projected density of states of their *d*-orbitals. The stoichiometric and oxygen-deficient structures are considered, and the structure with an O vacancy adjacent to each Pd is predicted to be favored.

I. INTRODUCTION

The many variations of structure and composition of solid oxide perovskites have been utilised to tailor their properties and applications for some time [1, 2]. It has been known that some ABO₃ perovskite oxides function well as proton conductors [3, 4], the most promising being doped BaCeO₃. The presence of large ions ($r_{\text{Ba}}=1.61$ Å, $r_{\text{Ce}}=0.87$ Å) on both A and B-sites makes the host perovskite cell unusually large.

Tolerance factor $t < 1$ usually leads to the rotation and expansion of the B-O₆ octahedra. Tolerance factor t is given by

$$t = \frac{R_{\text{A-O}}}{R_{\text{B-O}}\sqrt{2}} \quad (1)$$

where $R_{\text{A-O}}$ is the sum of A and O ionic radii and $R_{\text{B-O}}$ is the sum of B and O ionic radii. BaCeO₃ has $t=0.937$ and is predicted to be an anti-ferrodistortive dielectric material. In order to maintain t and study the effects of transition metal doping in BaCeO₃, Pd is chosen. The ionic radius of six-coordinate Pd⁺⁴ is 0.86 Å, very close to that of Ce⁺⁴. Though Ba²⁺ is known to stabilize higher oxidation states of transition metals, Pd⁺⁴ is not as common an oxidation state as Pd⁺². If Pd does reduce, then an O vacancy will be needed to maintain charge neutrality.

There are several theoretical studies of both the doped and undoped perovskite [5–8], however we have determined ground state structures of Pd-doped BaCeO₃ using DFT. In this work we explore structural and electronic properties of various Pd-doped BaCeO₃ perovskites, in order to elucidate why there is a range of stability in the various structures.

Undoped and Pd-doped BaCeO₃ calculations were performed on forty atom unit cells in a $2 \times 2 \times 2$ supercell arrangement allowing for the three-dimensional octahedral tilt that is seen in experiment. Structure 1 contained an

O vacancy adjacent to Pd, and Structure 2 contained the vacancy in the next unit over, between two Ce. Structure 3 contained no vacancy.

II. RESULTS

In the forty-atom BaCeO₃ $2 \times 2 \times 2$ unit cell, the O₆ tilt angles in this structure are all 12.2°. However, the tilts along (100) and (001) are anti-phase and indistinguishable from each other, while the tilts along (010) are in-phase. This structure belongs to the $a^-a^+a^-$ tilt system, and is indicative of the P_{nma} space group. We are able to reduce our forty-atom $2 \times 2 \times 2$ BaCeO₃ supercell to a twenty-atom $\sqrt{2} \times 2 \times \sqrt{2}$ irreducible unit cell that agrees well with experiment, as do the positions of ions from neutron refinements.

Structures 1, 2, and 3 have lattice constants $a = 8.799$, $b = 8.759$ and $c = 8.823$ Å, based on the relaxed BaCeO₃ structure. The higher energy vacancy structure was Structure 2, where the O vacancy was in between two Ce. This was 0.95 eV higher in energy than Structure 1. This is because Pd prefers to reside in a four-coordinate square planar geometry. A five-coordinate square pyramidal environment (PdO₅) would be more stable than PdO₆. As shown in Figure 1, the Pd in Structure 1 is roughly four-coordinate square-planar, and not the expected symmetric five-coordinate square-pyramidal. The first four shortest bond lengths are on average 2.04 Å, and the fifth is 2.66 Å. This longer bond length occurs as a result of the axial O in the CeO₅ square pyramid moving away from the Pd. This does not occur in Structure 2. All six Pd-O bond lengths in Structure 2 are around 2.02 Å, whereas the two Ce surrounding the vacancy seem to contract inward. These Pd-O bond lengths are similar to those seen in Structure 3, where there is no vacancy. This structure is not as stable as either of the vacancy structures, 1 and 2, which were more stable than Structure 3 by 2.4 and 3.3 eV respectively. This clearly

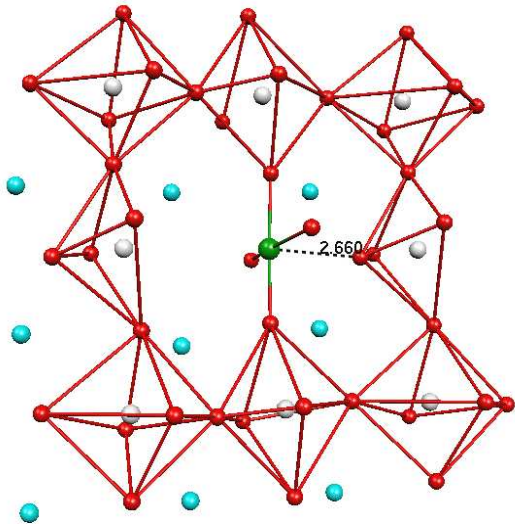


FIG. 1: Structure 1, where Pd dopant is accompanied by an O vacancy. This shows the lesser degree of octahedral distortion of the nearest neighbors when compared to Structure 2, as well as the increasingly symmetric tilt. O-O bonds surrounding Pd are omitted for clarity. Pd is green, Ba are light blue, Ce are gray and O red.

indicates that an O vacancy may be needed to alleviate some of the strain induced by Pd substitution.

Analysis of the density of states (DOS) shows that the band gap decreases upon Pd doping. It shows a further decrease when O vacancies are introduced into the doped structures between Pd and Ce atoms. The DFT calculated band-gap decreases going from Structure 3 to Structure 2 to Structure 1. The HOMO of these systems is mainly a hybridized Pd- d O- p type bond, and the LUMO are the Ce f states. The clearest example of this is in Structure 1, which contains an interesting feature absent from either Structures 2 or 3. Above the Fermi level, there is a d -orbital localized on Pd that is most likely $d_{x^2-y^2}$, which indicates the presence of Pd⁺². In

a square-planar environment, this is the non-degenerate d -orbital that is highest in energy, since d_{z^2} is filled. It is absent in Structures 2 or 3 because Pd assumes the Pd⁺⁴ oxidation state in those structures, surrounded by a complete O₆ octahedron. In comparing all three structures, the energy of the Ce f states is brought lower and the Pd- d O- p slightly higher as a vacancy is added between two Ce, as in Structure 2. Structure 1 however, has these levels even closer because more Pd d -states begin to be filled, as do some more O- p states. In doping BaCeO₃ with Pd, the band gap decreases. It decreases even further with the addition of an O vacancy in between a Pd-Ce pair as new d -states closer to the Fermi level begin to get populated, and previously unfilled bands decrease in intensity.

III. CONCLUSION

We have presented here a DFT study of the ground state structures of the undoped and Pd-doped rare-earth perovskite BaCeO₃. The substitution of Ce by Pd without an accompanying O vacancy distorts the doped perovskite moreso than with an accompanying vacancy, resulting in Structure 3 which is highest in energy by about 3.3 eV. When the vacancy is not adjacent to Pd, or in between two Ce, the structure is not as stable as when the O vacancy is next to Pd. Residing in between a Pd-Ce pair, the vacancy tilts the CeO₅ octahdra away from Pd, stabilizing a four-coordinate square-planar Pd geometry. The stabilization is about 0.95 eV. The coordination of Pd is also supported in the position of a newly filled Pd d -states just below the Fermi level of Structure 1 that are not filled in either Structures 2 or 3.

This work has been supported by the National science Foundation (CTS05-08455, DMR05-20415, DMR05-20020), the Department of Energy (DE-FG02-05ER15725, DE-AC52-06NA25396) Office of Basic Energy Sciences (BES) and the Air Force Office of Scientific Research (FA9550-04-0077). Computational support was provided by a Challenge Grant from the High Performance Computing Modernization Office (CHE-0131132).

-
- [1] I. Grinberg and A. M. Rappe, Appl. Phys. Lett. **85**, 1760 (2004).
 [2] M. R. Suchomel and P. K. Davies, Appl. Phys. Lett. **86**, 262905 (2005).
 [3] K.-D. Kreuer, S. J. Paddison, E. Spohr, and M. Schuster, Chem. Rev. **104**, 4637 (2004).
 [4] T. Shimura, H. Tanaka, H. Matsumoto, and T. Yogo, Solid State Ionics **176**, 2945 (2005).
 [5] R. Glockner, M. Islam, and T. Norby, Solid State Ionics **122**, 145 (1999).
 [6] K. Katahira, Y. Kohchi, T. Shimura, and H. Iwahara, Solid State Ionics **138**, 91 (2000).
 [7] R. A. Davies, M. S. Islam, and J. D. Gale, Solid State Ionics **126**, 323 (1999).
 [8] J. Wu, R. Davies, M. Islam, and S. Haile, Chem. Mater. **17**, 846 (2005).

Electric Field Induced Critical Points and Polarization Rotations in the PMN-PT System

R. Blinc and Z. Kutnjak

J. Stefan Institute, Ljubljana, Slovenia

Phone: +3861-447-3281; Fax: +3861-447-3191; e-mail: robert.blinc@ijs.si

High temperature resolution heat capacity, polarized light microscopy, dielectric, polarization, piezoelectric and Pb^{207} NMR investigations have been performed in $\text{PMN}_{1-x}\text{-PT}_x$ single crystals with $x=0, 0.10, 0.15, 0.25, 0.295$ and 0.31 . The electric bias field was applied along the $[111]$ and $[110]$ directions. For $\text{PMN}_{0.75}\text{-PT}_{0.25}$ and lower PT concentrations the critical behaviour is similar to that of pure PMN. The discontinuous jump in P at the ferroelectric-paraelectric transition for $E < E_{\text{cp}}$ disappears for $E \geq E_{\text{cp}}$. In the E-T phase diagram the line of first order ferroelectric transitions ends in an isolated critical point^[1] above which the difference between the different phases disappears and a continuous supercritical evolution is observed. For $\vec{E} \parallel [110]$ the common phase is pseudo-rhombohedral.

The situation is more complicated with increasing PT concentration close to the morphotropic boundary. The polarization data for $\vec{E} \parallel [110]$ show that at least three new phases (a monoclinic M_B , an orthorhombic O and another monoclinic M_C) exist between the rhombohedral (R) and tetragonal (T) ferroelectric phases. The phase sequence is $R \rightarrow M_B \rightarrow O - M_C - T$ and the polarization rotates^[2] under the applied $[111]$ field at fixed temperature from the T $[001]$ direction into the monoclinic $[101]$ (M_C) plane and then into the orthorhombic $[101]$ direction. From there it goes to the rhombohedral $[111]$ direction via the (101) monoclinic (M_B) plane. There are two critical points: one exists for the C-T and the other for the T- M_C transition. For the T to C transition at $x=0.295$ the critical point is at $E_{\text{cp}}=1.3\text{kV/cm}$ and for the T- M_C transition at $E_{\text{cp}}=1.25\text{kV/cm}$. The heat capacity, dielectric, and piezoelectric data demonstrate that the existence of the critical points in the E-dimension of the T-x-E phase diagram of the PMN-PT system results in a significant enhancement of the piezoelectric coefficient as well as a significant decrease of the energy costs and correspondingly the electric fields necessary to induce the R- M_B - O - M_C -T polarization rotations which produce the giant lattice strains. The system behaves as being effectively semi-soft as $E \rightarrow E_{\text{cp}}$. The electric fields induced critical points thus provide a new driving force for the giant electromechanical response.

[1] Z. Kutnjak, J. Petzelt, and R. Blinc, Nature **441**, 956 (2006)

[2] H. Fu and R. E. Cohen, Nature 403 , **281** (2000)

The effect of Pb-O divacancy Pairs on the Ferroelectric-Relaxor Transition in $\text{Pb}(\text{Sc}_{1/2}\text{Nb}_{1/2})\text{O}_3$

B. P. Burton,¹ Silvia Tinte,¹ Eric Cockayne,¹ and U. V. Waghmare²

¹*Ceramics Division, Materials Science and Engineering Laboratory, National Institute of Standards and Technology Gaithersburg, MD 20899-8520, USA*
²*J. Nehru Theoretical Sciences Unit, JNCASR, Jakkur, Bangalore, 560 064, INDIA*

Chemically disordered $\text{Pb}(\text{Sc}_{1/2}\text{Nb}_{1/2})\text{O}_3$ (PSN) exhibits a relaxor ferroelectric (RFE [1, 2]) to normal ferroelectric (FE) transition. Chu et al. [3] (also [4–6]) demonstrated that the addition of 1.7 atomic % [Pb-O] divacancy pairs depresses the FE transition temperature, T_{FE} , of chemically disordered PSN from ~ 373 K to ~ 338 K. This suggests that a sufficient concentration of divacancy pairs, $X_{[\text{Pb}-\text{O}]}$, will drive the system to a fully relaxor state, without a FE ground-state phase. Introducing Pb vacancies [8], or more likely, Pb-O divacancy pairs [7] increases the average strength of local “random fields” $\langle h_i \rangle$, and therefore it is expected [10, 11] that increasing $X_{[\text{Pb}-\text{O}]}$ will also drive the system toward a fully relaxor state. Thus, $\langle h_i \rangle$ is a *nonordering* field [12] that can be used to tune the proportions of relaxor vs. FE character in the system.

Increasing hydrostatic pressure (P) drives chemically disordered PSN into a fully relaxor state [9], and previous simulations by Tinte et al. [10] explain this result as follows: 1) increasing pressure has a negligible effect on the contribution to $\langle h_i \rangle$ from chemical disorder or vacancies; 2) pressure smoothly and monotonically reduces FE well depths [13–15], and thus destabilizes the FE phase relative to the RFE state of the paraelectric phase; 3) Keeping $\langle h_i \rangle$ constant while reducing the competition from normal FE-ordering corresponds to a *relative* increase in $\langle h_i \rangle$. Because P does not induce “random fields,” $\langle h_i \rangle$ must be nonzero, e.g. from chemical disorder, for increased P to induce a FE→RFE transition. Increasing $X_{[\text{Pb}-\text{O}]}$, however, directly increases $\langle h_i \rangle$, and will drive the system towards a FE→RFE transition, even if $\langle h_i \rangle = 0$ initially. Therefore, in a system with sufficient chemical disorder, one expects that the T vs. P phase diagram will be topologically equivalent to the T vs. $X_{[\text{Pb}-\text{O}]}$ phase diagram, as shown in Figures 1a and 1b.

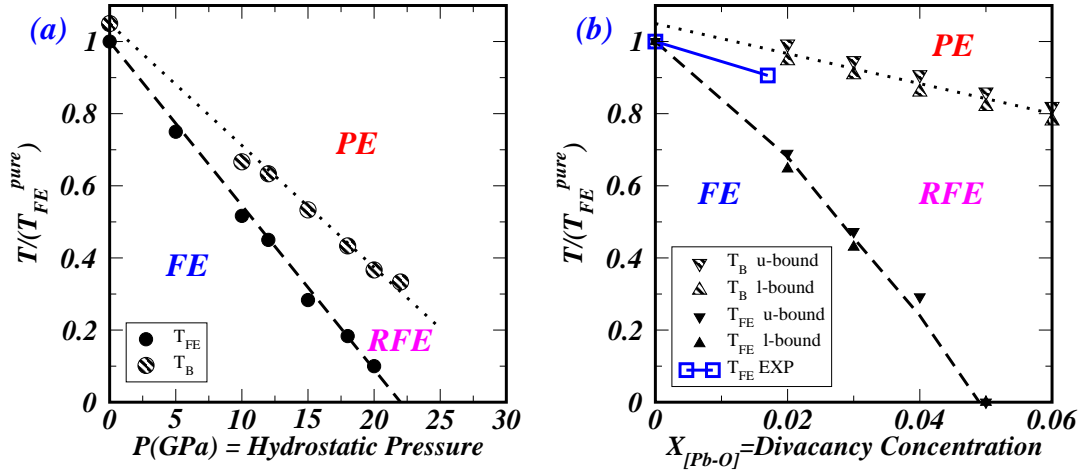


FIG. 1: Predicted PSN phase diagrams : (a) P vs. reduced temperature, T/T_{FE} ; (b) $X_{[\text{Pb}-\text{O}]}$ vs. T/T_{FE} . Dashed lines indicate the ferroelectric transition, T_{FE} , and dotted lines indicate the Burns temperature, T_B [16]. Triangles indicate upper- and lower-bounds, u- and l- respectively. The diagrams are topologically equivalent because both P and $X_{[\text{Pb}-\text{O}]}$ are related to the underlying *nonordering field* [12], $\langle h_i \rangle$, the spatial average strength of “random fields” that promote the relaxor state.

Details of the simulations used to calculate the diagrams in Figures 1 are given in: the review by Burton et al. [11]; the study of P-effects (Figure 1a) [10]; and the first-principles calculation of the dipole moment for a Pb-O nearest neighbor (NN) divacancy pair in PbTiO_3 [7]. As in Ref. [10], the simulation supercell contained $40 \times 40 \times 40$ Pb-site local mode variables, with the same “nano-ordered” chemical configuration: 20 ordered clusters of 800 sites each in

a percolating random matrix. Only NN divacancy pairs were considered, and they were assumed to have the same moments as in PbTiO_3 [7]. This treatment is distinct from that of Bellaiche et al. [8] which considered Pb-vacancies without charge-compensating O-vacancies. Presumably the real system has divacancy pairs as reported by Chu et al. [3], but our NN-divacancies approximation apparently overestimates $\langle h_i \rangle$ as a function of $X_{[\text{Pb-O}]}$. Thus, the simulations predict a steeper slope for T_{FE} vs. $X_{[\text{Pb-O}]}$ than is observed experimentally. A possible explanation is that the populations of second- and possibly farther- neighbor divacancy pairs are significant, and because the magnitudes of their dipole moments are inevitably smaller than those of NN pairs, a more realistic approximation of divacancies would yield a more gentle slope for $\langle h_i \rangle$ as a function of $X_{[\text{Pb-O}]}$.

Qualitatively, the only apparent, and small, difference between Figures 1a and 1b is that $T_{FE}(\text{P})$ appears to be approximately linear, while $T_{FE}(X_{[\text{Pb-O}]})$ exhibits slight negative curvature.

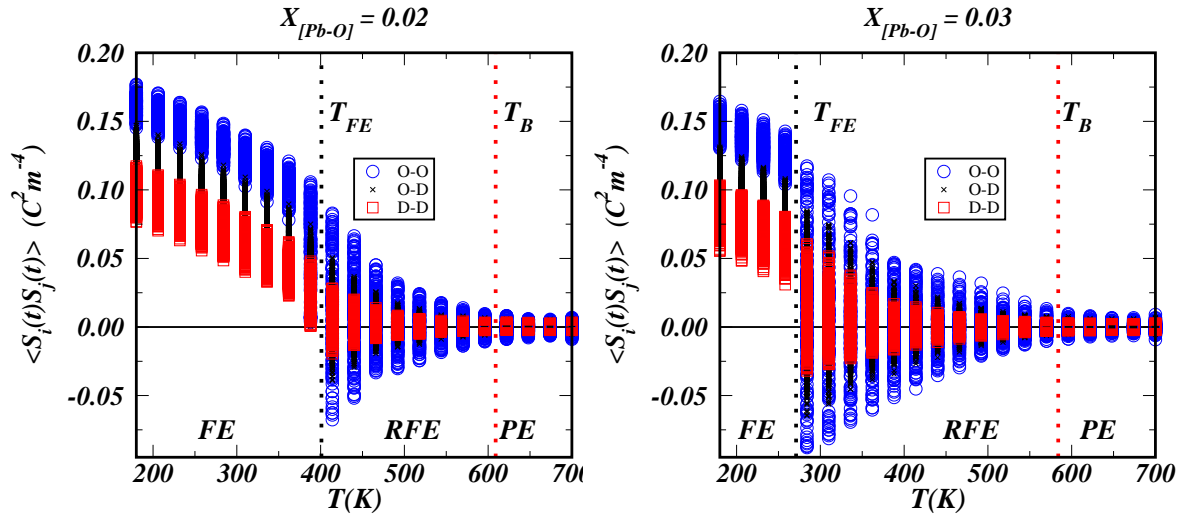


FIG. 2: Predicted cluster-cluster spin products for a nano-ordered system with $X_{[\text{Pb-O}]} = 0.03$.

As in the P-dependent simulations, we calculated cluster-cluster spin products for 800-site clusters (Fig. 2): O-O are the products between average spins on two chemically ordered clusters, O-D the products between one chemically ordered and one chemically disordered cluster, and D-D the products between two chemically disordered clusters. Figure 2 shows the spin products for the nano-ordered system with $X_{[\text{Pb-O}]} = 0.02$, and $X_{[\text{Pb-O}]} = 0.03$, and clearly shows how the RFE-state region increases as $X_{[\text{Pb-O}]}$ increases.

-
- [1] G. A. Smolensky and A. I. Agranovskaya, Sov. Phys. Sol. State **1**, 1429 (1959).
 - [2] L. E. Cross, Ferroelectrics **76**, 241 (1987).
 - [3] F. Chu, I.M. Reaney and N. Setter, J. Appl. Phys. **77**[4], 1671 (1995).
 - [4] F. Chu, N. Setter and A. K. Tagantsev, J. Appl. Phys. **74**[8], 5129 (1993).
 - [5] F. Chu, I.M. Reaney and N. Setter, J. Amer. Ceram. Soc. **78**[7], 1947 (1995)
 - [6] F. Chu, G. Fox and N. Setter, J. Amer. Ceram. Soc. **81**, (6) 1577 (1998)
 - [7] E. Cockayne and B. P. Burton, Phys. Rev. B **69**, 144116 (2004).
 - [8] L. Bellaiche, J. Ñiguez, E. Cockayne, and B. P. Burton Phys. Rev. B (to appear).
 - [9] E. L. Venturini, R. K. Grubbs G. A. Samara, Y. Bing and Z.-G. Ye, in review Phys. Rev. B (2006).
 - [10] S. Tinte, B. P. Burton, E. Cockayne and U. V. Waghmare, Phys. Rev. Lett. **97**, 137601 (2006).
 - [11] B. P. Burton, E. Cockayne, S. Tinte and U. V. Waghmare, Phase Trans. **79**, 91 (2006).
 - [12] J. M. Kosterlitz, D. R. Nelson and M. E. Fisher Phys. Rev. B, **13** 412- (1976).
 - [13] R. E. Cohen, Nature (London) **358**, 137 (1992), Also, R.E. Cohen and H. Krakauer, Ferroelectrics **136**, no.1-4, 65 (1992)
 - [14] G. Saghi-Szabo, R. E. Cohen and H. Krakauer, Phys. Rev. Lett. **80**, 4321 (1998).
 - [15] M. Fornari and D. Singh Phys. Rev. B **63**, 092101 (2001).
 - [16] G. Burns and F. H. Dacol, Solid State Commun. **48**, 853 (1983).

Coexistence of polar order and local domain dynamics in ferroelectric perovskites

Annette Bussmann-Holder¹, Helmut Büttner² and Alan R. Bishop³

¹Max-Planck-Institute for Solid State Research, Heisenbergstr.1, D-70569 Stuttgart, Germany

²Lehrstuhl für Theoretische Physik, Universität Bayreuth, D-95540 Bayreuth, Germany

³Los Alamos National Laboratory, Los Alamos, NM 87545, USA

Phone: +49 711 689 1679; Fax: +49 711 689 1091; e-mail: a.bussmann-holder@fkf.mpg.de

From the early history of research in ferroelectric perovskites, inelastic neutron scattering experiments have shown that not only a transverse optic mode softens substantially with decreasing temperature to freeze out at T_c , but that simultaneously finite momentum q anomalies appear in the related transverse acoustic mode. These anomalies are common to nearly all perovskite ferroelectrics but have never been addressed in detail. What does it mean to have a finite momentum incomplete acoustic mode softening simultaneously appearing with a long wave length optic mode instability? Clearly, the acoustic mode characterizes the elastic stability of the system. Its collapse would indicate a ferroelastic transition where strain/stress plays the role of an order parameter, whereas the polarisation is the order parameter in a purely ferroelectric system. The observation of finite momentum anomalies indicates an incipient ferroelastic instability on characteristic length scales, where only finite size domains transform into a new phase. Since softening is never complete in these systems and long wave length coherence is not observed, these anomalies are fingerprints of the formation of *dynamical* ferroelastic domains which are formed far above T_c , and their time and length scales change with temperature. Even though a mode-mode coupling approach has been invoked very early, neither a quantitative agreement between theory and experiment could be achieved nor a physical understanding of the microscopic origins. Here we show that mode-mode coupling is indeed the origin, however only so long as polarizability effects are its source. In addition, *we demonstrate that a dispersive long wave length soft mode can coexist with local symmetry breaking domains*. We address also the origin of ferroelectricity in isotope substituted $\text{SrTi}^{18}\text{O}_3$ and show that locally distorted dynamical patterns form far above T_c caused by an incipient tendency towards finite size elastic instabilities.

Influence of size effects on the relaxor behaviour and on the rotation of polarization in the PMN-PT system

J. Carreaud¹, J.M. Kiat^{1,2}, B. Dkhil¹

¹Laboratoire Structures, Propriétés et Modélisation des Solides, CNRS-UMR8580, Ecole Centrale Paris, 92290 Châtenay-Malabry, France

²Laboratoire Léon Brillouin, CE Saclay, 91191 Gif-sur-Yvette, France

Phone : +33(0)1 41 13 15 84; Fax : +33(0)1 41 13 14 37; e-mail : carreaud@spms.ecp.fr

Strongly connected with technological applications the question of ferroelectricity at nanometric scale on classical ferroelectrics has been recently revived due to new experimental results on nanograins of compounds such as BaTiO₃ and PbTiO₃, on thin films [1], as well as on nanocrystals reported by Scott et al. [2], who show existence of polar order in nanometric BaTiO₃ samples, thus contradicting previous experimental and theoretical works. However only very few results have been reported regarding size effect on morphotropic phase boundary (MPB) systems based on relaxor compounds especially on the prototype relaxor family PbMg_{1/3}Nb_{2/3}O₃-PbTiO₃ (PMN-PT) [3, 4] for which the smallest size studied was only about 150 nm. In this framework we present structural and dielectric results obtained on PMN-PT samples with grain sizes as low as 10nm for compositions PMN, PMN-20PT and PMN-35PT. This set of results shows the possibility to tailor the relaxor behaviour and the polarisation direction by changing the grain size.

Samples studied are powders and ceramics with different grain sizes (0.01 to 4 μm) obtained from nanocrystalline powders prepared by mechanochemical synthesis (10-20 nm) which were grown by calcination and sintering (conventional and hot-pressing) at different temperatures .

PMN is the textbook relaxor compound. Our dielectric measurements have shown a vanishing of the relaxation when the grain size becomes as low as the typical sizes of polar nanoregions PNRs (≈ 30 nm). PMN-35PT is a compound inside the MPB region with no dielectric relaxation for conventional grain sizes. However we have observed appearance of dielectric relaxation for grain size below ≈ 200 nm, (Figure 1). At lowest size (≈ 30 nm) the dielectric anomalies have completely disappeared, indicating a transformation to a conventional nonferroelectric phase.

Observation in PMN of strong X-ray diffraction diffuse scattering in addition to cubic Bragg peaks at 80K, as well as persistence of Raman signal reveal the persistence of PNRs down to the smallest grain sizes (≈ 15 nm). Moreover the correlation length of the polar order is the same as the size of the grain.

Concerning PMN-35PT, in agreement with the disappearance of dielectric and also of the Raman signal observed at the smallest sizes, a Rietveld analysis shows a structural transformation from a monoclinic Pm to a cubic phase as grain size is decreased. These results and the dielectric measurements show the destruction of the long range polar order below 200nm towards PNRs (relaxor state) and, below 15nm to a paraelectric system.

Considering that MPB compounds are very sensitive to internal and external fields, all these effects are discussed in connection with strain/electric field effects [5].

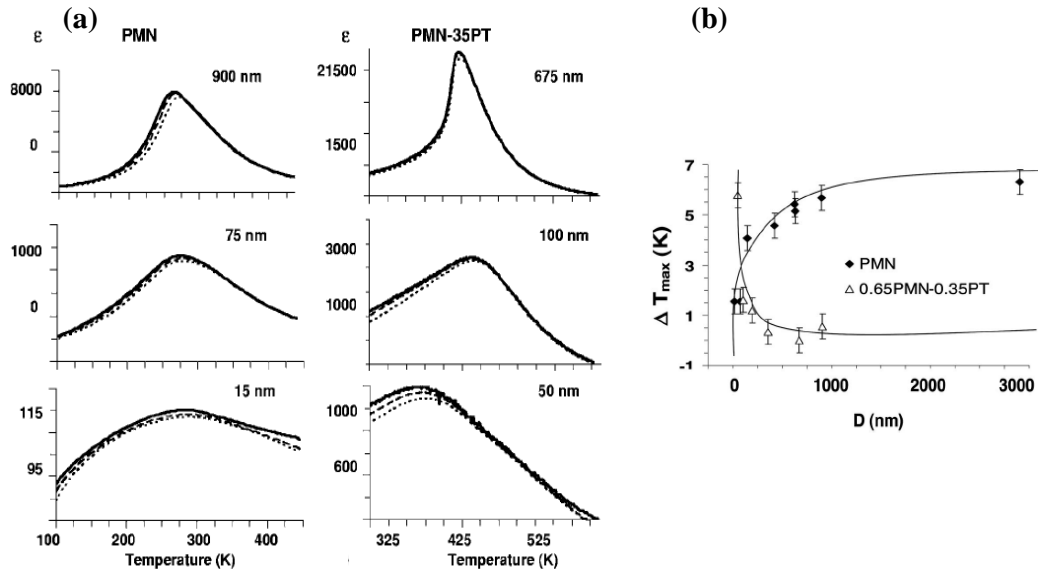


Figure 1 : Temperature and size dependence of a) dielectric constant and b) dielectric relaxation defined by $\Delta T_{\max}(f) = T_{\max}(100\text{KHz}) - T_{\max}(10\text{KHz})$ in PMN and PMN-35PT. Plain, dotted and dashed line correspond to frequency 1, 10 and 100 KHz.

A size driven rotation of the polarisation was also clearly evidenced by Rietveld analysis of dense ceramics of a compound at the border of the morphotropic phase boundary i.e. PMN-20PT. With size reduction the polarisation rotates in the monoclinic plane from M_B i.e. $P_x = P_y > P_z$ to M_A i.e. $P_x = P_y < P_z$ and finally reaches a rhombohedral phase, i.e. $P_x = P_y = P_z$, below ≈ 200 nm (Figure 3) with no diminishing in the amplitude of the polarisation. These results show the possibility of obtaining monoclinic or rhombohedral phases depending on the grain size and solve contradictions reported in the literature concerning this system and other MPB systems. Moreover it offers an easy way to tailor the direction of the polarisation of these materials [6].

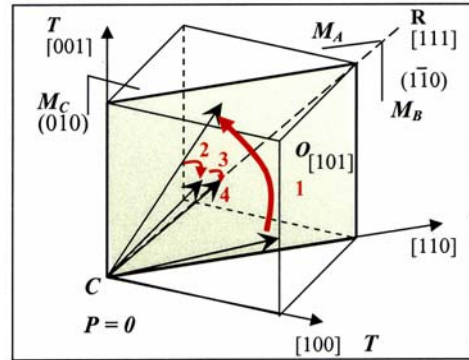


Figure 3 : Rotation of the polarisation in PMN-20PT at room temperature as grain size decreases from 1) $4\ \mu\text{m}$ to 400 nm, 2) 400 nm to 250 nm, 3) 250 to 150 nm and 4) 150 to 100 nm.

References

- [1] D. D. Fong, G. B. Stephenson, S. K. Streiffer, J. A. Eastman, O. Auciello, P. H. Fuoss, C. Thompson, "Ferroelectricity in ultrathin perovskite films", *Science* **304**, 1650 (2004).
- [2] J. F. Scott, F.D. Morrison, M. Miyake, P. Zubko, X Lou, V.M. Kugler, S. Rios and M Zhang, *J. Am. Ceram. Soc.* **88** (7) 1691 (2005).
- [3] P. Papet, J.P. Dougherty, T.R. Shrout, *J. Mater. Res.* **5** (12), 2902 (1990).
- [4] T. Mishima, H. Fujioka, S. Nagakari, K. Kamigami and S. Nambu, "Lattice image observations of nanoscale ordered regions in $\text{Pb}(\text{Mg}_{1/3}\text{Nb}_{2/3})\text{O}_3$ ", *Jpn. J. Appl. Phys.* **36**, 6141-6144 (1997).
- [5] J. Carreaud, P. Gemeiner, J. M. Kiat, B. Dkhil, C. Bogicevic, T. Rojac, and B. Malic *Phys. Rev. B* **72**, 174115 (2005).
- [6] J. Carreaud, J. M. Kiat, B. Dkhil, M. Alguero, J. Ricote and R. Jiménez, J. Holc and M. Kosec, *Appl. Phys. Lett.* **89**, 252906 (2006).

Towards Materials by Design: Exploring Properties of Piezoelectrics from First-Principles

R.E. Cohen

Carnegie Institution of Washington, Washington, D.C. 20015

Phone: 202-478-8937; e-mail: cohen@gl.ciw.edu

A range of recent work will be reviewed based on first-principles density functional computations. All first-principles computations were performed using the ABINIT package.¹ To obtain finite temperature properties or properties of disordered materials, the first principles results were used to parametrize a shell-model which was used for molecular dynamics simulations.²

Linear Response Computations

We used the ABINIT code to relax structures, compute total energies, and phonon dispersion curves, Born effective charges, and polarizations were computed for a range of perovskites, LiNbO₃, and perovskite oxynitrides. These results were used to better understand experimental data, and to explore and search for new stable polar compounds.

First-principles based shell-model

Unlike effective Hamiltonian models all of the atomic degrees of freedom including hard modes are included, allowing accurate thermal expansivity and anharmonic dressing of soft modes. Unlike previous potential models, the effective charges are intrinsic to the model, including variations in effective charges with structure or dynamical motions of the ions. We fit first-principles total energies, forces, stresses, Born transverse effective charges, dielectric tensors, and phonon frequencies.

Pyroelectricity in LiNbO₃

The resulting shell model parameters are transferable among perovskites, but we found refitting was required to obtain a reasonable potential for the LiNbO₃ structure, because the Nb-charges appropriate for PMN were not appropriate for LiNbO₃. The model is essentially that reported previously,² but the parameters were refit. All molecular dynamics results presented here are preliminary. Molecular dynamics (MD) simulations for LiNbO₃ were performed as functions of temperature for 2160 atom supercells (6x6x6 10 atom unit cells), and shell coordinates were also treated as dynamical variables. We found a T_c of about 950 K, compared with the experimental value of 1480 K. This may be due to the local density approximation data, to which the potential was fit, or may be due to lack of convergence of the MD system size.

The pyroelectric coefficient can be found from the change in polarization with temperature, $\Pi=dP/dT$. This is a stringent test of the model since pyroelectricity is a high order property. We obtain a pyroelectric coefficient of $-98 \mu\text{C}/\text{m}^2$ at 300 K, in reasonable agreement with experiment. We have also analyzed the relative contributions from the clamped lattice contribution (the so-called primary piezoelectric coefficient) and the secondary contribution, which arises from thermal dilation.

We also performed linear response lattice dynamics with ABINIT, and computed the quasiharmonic free energies from the frequencies as functions of volume. Using this we obtain the thermal expansivity, which is in good agreement with experiment. Using the thermal expansion and the polarization versus volume we were able to directly determine the secondary pyroelectric effect.

Polarization switching in PbTiO₃

We studied polarization switching in PbTiO₃ using molecular dynamics with the shell model. Depending on the field and temperature, and the presence or absence of domain walls, we find a range of interesting behaviors. Homogeneous periodic systems switch via polarization rotation. Systems with domains switch through domain motion for low to moderate fields, but the domain motion involves polarization rotation at the interface. For high fields switching occurs in the bulk even in the presence of domains.

Polarization rotation and electromechanical response in PMN-PT and PZN-PT

We have simulated polarization rotation in PMN-PT by studying its behavior under applied fields using molecular dynamics. Good agreement is also found for the PMN-PT phase diagram. In conjunction with the Carnegie Institution experimental group we are exploring the relative importance of intrinsic bulk and extrinsic domain driven response.

High temperature piezoelectricity in BS-PT

We have parameterized our shell model to simulate BS-PT solid solutions, which have very high T_c 's and thus are candidates for high temperature piezoelectrics. This work is in progress, but so far is in good agreement with available experiments.

New oxynitrides

We have predicted new ordered oxynitrides which have very large polarizations, and large predicted non-linear optic coefficients. A large number of compounds were studied computationally, and two excellent candidates were found, YSiO₂N and YGeO₂N. Polarizations are predicted of 170 $\mu\text{C}/\text{cm}^2$ and 184 $\mu\text{C}/\text{cm}^2$, respectively. For comparison, the polarization of LiNbO₃, one of the highest known polarizations, is 71 $\mu\text{C}/\text{cm}^2$. Under normal applications the polarization itself is not as important as its change with respect to field or strain. We also compute non-linear optic coefficients, and find values of $d_{15}=-2.0$ pm/V and 2.6 pm/V in YSiO₂N and YGeO₂N, respectively, with d_{33} 's of -5.5, and -4.5, compared with 0.4 pm/V in KDP, a commonly used non-linear optic material.

This work is in collaboration with R. Caracas, Yajie Lei, Q. Peng, M. Sepliarsky, Q. Peng, and Xiaowei Zeng. This work is supported by Office of Naval Research grant N00014-02-1-0506.

1. X. Gonze, J. M. Beuken, R. Caracas et al., Computational Materials Science 25 (3), 478 (2002).
2. M. Sepliarsky, Z. Wu, A. Asthagiri et al., Ferroelec. 301 (2004).

Stability of Glassy and Ferroelectric State in the Relaxors.

Eugene V. Colla, M.B. Weissman

Department of Physics, University of Illinois at Urbana-Champaign.

Phone: 217-333-5772; Fax: 217-244-7187; e-mail koll@uiuc.edu

The relaxor ferroelectrics display a long list of diverse electric properties but do not spontaneously undergo a phase transition to a state with long range ferroelectric order (LRFO) at zero field[1]. It is well known[2, 3] that an applied electric field can induce LRFO in the familiar relaxor $\text{PbMg}_{1/3}\text{Nb}_{2/3}\text{O}_3$ (PMN). It was found that this new induced state could be stable even without DC bias at low enough temperature. Doping of

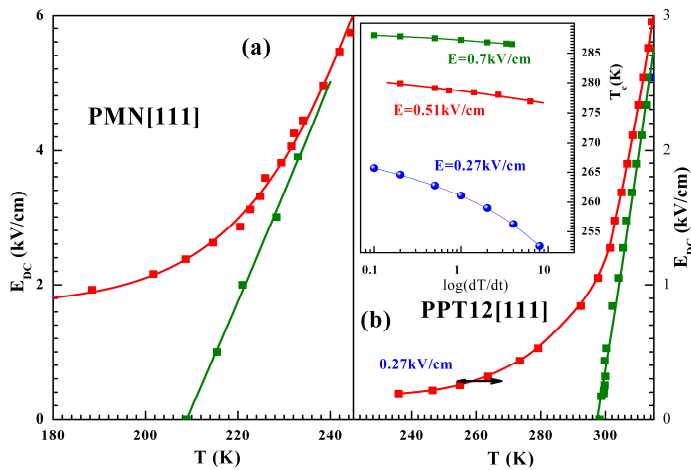


Fig.1 Phase diagrams for PMN and PPT12

PMN by lead titanate (PT) makes this induced transition easier and at doping level higher than 33-35% the system shows regular ferroelectric properties. The empirical phase diagrams (PD) for PMN [111] and PMN-PT12% [111] (PPT12) are depicted in Fig.1. Both materials show a hysteretic behavior. The left hand lines represent the transition into the ordered state (freezing) observed under field cooling.

The right lines show the melting. For the PMN PD there was claimed[3] to be a threshold field E_{th} for the induced transition. For PPT12 the existence of such a threshold has not been shown, i.e. the stability of the glassy phase at any E has not been demonstrated. We performed some experiments on the kinetics and aging to explore which phase is stable. Field cooling (FC) at rates from 0.1 to 10 K/min gave a broad range of freezing temperatures (T_f), e.g over 13K spread at 0.27kV/cm. Since slowing the cooling results in significant increase of T_f , T_f does not represent a true thermodynamic transition temperature. The dependence of T_f on cooling rate for three different E_{DC} 's is depicted in the insert to Fig.1b. For higher fields the variation of T_f becomes smaller. Warming experiments show no dependence of the melting temperature on rate in this range, as seen in Figure 2 where the records of pyroelectric current are presented. The current spikes move dependent on cooling rate and appear at the same position while heating. The practical range of rates is not enough to determine if the freezing and melting lines would converge at slow enough rates.

Aging experiments confirmed that the ordered phase rather than the glassy phase is stable in the hysteretic region of the PD. Field cooling, but not quite to T_f , and then aging *in zero field* at constant temperature leads to polarization of the sample in time. For

T=260K and a cooling field of E=0.177kV/cm it took ~ 30 hours at E=0 to reach the saturation polarization of ~30 μ C/cm² typical for perovkite ferroelectrics.

Similar experiments were performed on a PMN[111] sample. Unfortunately the available crystal did not show a sharp field induced transition to LRFO phase and the

results on this material are mostly preliminary. The measurements of the pyroelectric current in FC – ZF aging – ZF heating experiment show decreasing of the polarization while aging, opposite to the trend for PPT12. This is an indication that unlike for PPT12 the PMN disordered glassy phase may be stable at E=0. Since on heating the sample showed abrupt current spikes from melting of ordered regions, nuclei with LRFO appeared to be present during the spontaneous depolarization, suggesting that the glassy phase is indeed thermodynamically favored. For PMN where the true phase boundary or boundaries are remains to be determined for crystals displaying sharp transitions similar to one found

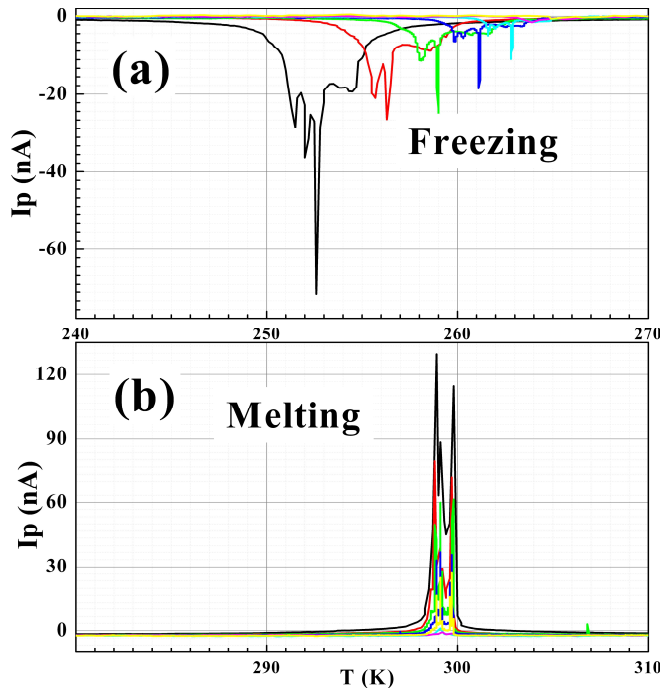


Fig.2 Freezing - melting pyroelectric current spikes in PPT12

in[4].

We thank our collaborators, Dwight Viehland and Brahim Dkhil both for samples and for thoughtful advice. This work was funded by NSF DMR 02-40644 and used facilities of the Center for Microanalysis of Materials, University of Illinois, which is partially supported by the U.S. Department of Energy under grant DEFG02-91-ER4543.

1. Cross, L.E., *Relaxor Ferroelectrics: An Over View*. Ferroelectrics, 1994. **151**: p. 305-320.
2. Schmidt, G., et al., *Induced Phase Transitions in Ferroelectrics with Difuse Phase Transition*. phys. stat. sol. (a), 1981. **63**(501-510).
3. Colla, E.V., et al., *Field Induced Kinetic Ferroelectric Phase Transition in Lead Magnoniobate*. Ferroelectrics, 1996. **184**: p. 209-215.
4. Colla, E.V., et al., *The Lead Magnoniobate Behavior in Applied Electric Field* Ferroelectrics, 1994. **151**: p. 337-342.

Polarization Enhancement in Short Period Superlattices via Interfacial Intermixing

Valentino R. Cooper, Karen Johnston, and Karin Rabe
 Department of Physics and Astronomy, Rutgers University
 136 Frelinghuysen Rd, Piscataway, New Jersey 08854-8019, USA
 Phone 732-445-4601; e-mail: vcooper@physics.rutgers.edu

Ferroelectric superlattices present a unique paradigm for creating novel materials for modern devices. In ideal superlattices with perfectly flat, compositionally abrupt interfaces, first-principles calculations and experimental studies have shown how factors such as strain due to lattice mismatches [1–14], charge compensation [15–18] and bonding at the interface [19] can be controlled to enhance the ferroelectric properties of the superlattice. Recent high resolution COBRA studies on SrTiO₃ (ST) supported PbTiO₃ (PT) thin films suggest that an additional factor, cation intermixing at the interface, may occur [20]. Our results for short period PT/ST superlattices demonstrate that interfacial intermixing significantly enhances the polarization and may be useful in tuning other macroscopic properties of these materials.

Here, we use density functional theory (DFT) to examine the effects of interlayer cation mixing on the polarization within PT/ST superlattices. We compare superlattices with sharp interfaces with three different compositionally equivalent intermixed systems of $n=1-3$ ST layers and $m=1-3$ PT layers. All calculations were performed with the Vienna Ab initio Simulation Package (VASP) [21], with the local density approximation for the exchange correlation functional and using projector augmented wave (PAW) potentials [22, 23]. ST was found to be cubic with a lattice constant of 3.86 Å (experiment: 3.925 Å). The tetragonal PT lattice constants were computed as $a=3.87$ Å and $c=4.03$ Å (experiment: $a=3.935$ Å and $c=4.02$ Å). This agreement is typical of LDA calculations of ferroelectric perovskites. In all calculations the in-plane lattice constant was constrained to that of the theoretical ST lattice constant. Ionic coordinates were fully relaxed while the lattice vectors were optimized only along the c axis. For all intermixed supercells two layers

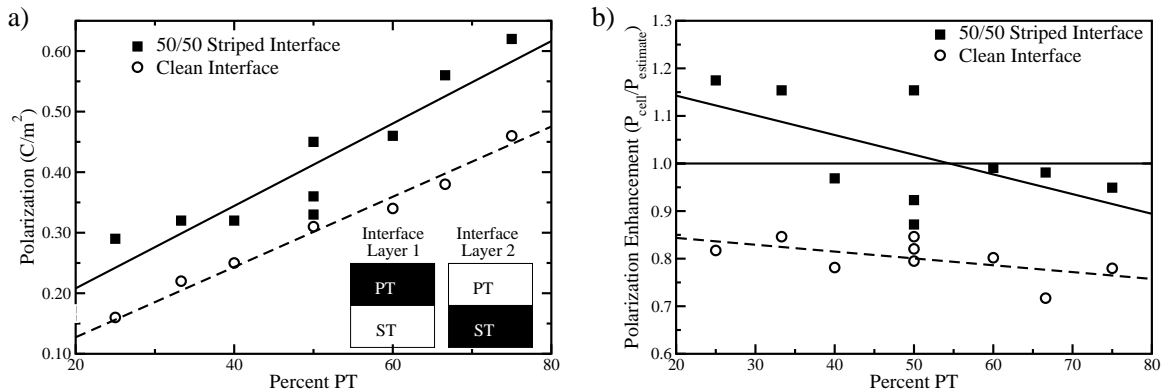


FIG. 1: a) Polarization and b) polarization enhancement as a function of PT concentration for m_{PT}/n_{ST} short period superlattices. The solid squares (■) represents 50/50 striped interfaces (see inset) and the open circles (○) are for the sharp interfaces. The solid lines (—) and dashed lines(- -) are fits through the 50/50 striped interface and sharp interface data respectively.

of mixed PT/ST were placed at each interface. Polarizations were computed using the Berry phase method [24]. Polarization enhancements (P_{enhance}) were computed using:

$$P_{\text{enhance}} = \frac{P_{\text{actual}}}{P_{\text{estimate}}} \quad (1)$$

where P_{estimate} is an average of bulk PT and ST polarizations.

Figure 1a depicts the polarization as a function of PT concentration for the sharp interface and the 50/50 striped m_{PT}/n_{ST} short period superlattices studied. For both interfaces we see a marked increase in the total polarization as a function of percent PT. In all cases, the mixed PT/ST interface superlattices exhibited larger polarizations than the sharp interfaces. Furthermore, figure 1b shows that the polarization enhancement for the PT/ST 50/50 striped superlattice is either greater than or equal to that which would be expected by averaging the polarizations of an equivalent number of bulk PT and bulk ST cells. While, the sharp interfaces result in smaller polarizations than estimated from bulk PT and ST superlattices.

In conclusion our results indicate that the presence of intermixed PT/ST layers enhances the polarization of the superlattice over that of the ideal sharp interfaces. This enhancement is greater than would be expected from a combination of bulk PT and ST supercells and suggests a new mechanism for tailoring the properties of short period superlattices.

-
- [1] H. Tabata, H. Tanaka, and T. Kawai, *App. Phys. Lett.* **65**, 1970 (1994).
 - [2] H. M. Christen *et al.*, *App. Phys. Lett.* **68**, 1488 (1996).
 - [3] J. C. Jiang *et al.*, *App. Phys. Lett.* **74**, 2851 (1999).
 - [4] F. Le Marrec *et al.*, *Phys. Rev. B* **61**, R6447 (2000).
 - [5] O. Nakagawara *et al.*, *App. Phys. Lett.* **77**, 3257 (2000).
 - [6] M. Sepliarsky *et al.*, *J. Appl. Phys.* **90**, 4509 (2001).
 - [7] A. Q. Jiang *et al.*, *J. App. Phys.* **93**, 1180 (2003).
 - [8] J. B. Neaton and K. M. Rabe, *App. Phys. Lett.* **82**, 1586 (2003).
 - [9] S. Rios *et al.*, *J. Phys.:Cond. Matt.* **15**, L305 (2003).
 - [10] C. Bungaro and K. M. Rabe, *Phys. Rev. B* **69**, 184101 (2004).
 - [11] M. Dawber *et al.*, *Phys. Rev. Lett.* **95**, 177601 (2005).
 - [12] K. Johnston *et al.*, *Phys. Rev. B* **71**, 100103 (2005).
 - [13] H. N. Lee *et al.*, *Nature* **433**, 395 (2005).
 - [14] S. M. Nakhmanson, K. M. Rabe, and D. Vanderbilt, *App. Phys. Lett.* **87**, 102906 (2005).
 - [15] M. Dawber *et al.*, *J. Phys.: Cond. Matt.* **15**, L393 (2003).
 - [16] J. Junquera and P. Ghosez, *Nature* **422**, 506 (2003).
 - [17] C. H. Ahn, K. M. Rabe, and J.-M. Triscone, K. M. Rabe, *Science* **303**, 488 (2004).
 - [18] A. M. Kolpak, N. Sai, and A. M. Rappe, *Phys. Rev. B* **74**, 054112 (2006).
 - [19] D. D. Fong *et al.*, *Phys. Rev. Lett.* **96**, 127601 (2006).
 - [20] D. D. Fong *et al.*, *Phys. Rev. B* **71**, 144112 (2005).
 - [21] G. Kresse and J. Furthmüller, *Phys. Rev. B* **54**, 11169 (1996).
 - [22] P. E. Blöchl, *Phys. Rev. B Rapid Comm.* **41**, 5414 (1990).
 - [23] G. Kresse and D. Joubert, *Phys. Rev. B* **59**, 1758 (1999).
 - [24] R. D. King-Smith and D. Vanderbilt, *Phys. Rev. B* **47**, 1651 (1993).

NEW PIEZOELECTRIC COMPOSITES DRIVEN BY FLEXOELECTRIC CHARGE SEPARATION

L. Eric Cross, John Y. Fu, Wenyi Zhu, Nan Li
187 Materials Research Laboratory, Penn State University, PA USA
Phone: 814-865-1181, E-mail: lec3@psu.edu

Flexoelectricity is a property of all solid dielectrics. The direct flexoelectric effect is described by the relation

$$P_m = \mu_{ijkm} \nabla_k S_{ij}$$

where P_m is the electric polarization induced by the elastic strain gradient $\nabla_k S_{ij}$. The flexoelectric coefficients μ_{ijmk} form a fourth rank polar tensor with symmetry constraints similar to the electrostrictive Q_{ijmk} . The thermodynamic converse effect is described by

$$T_{ij} = \mu_{ijkm} \nabla_k E_m$$

where T_{ij} are the components of elastic stress and $\nabla_k E_m$ the gradient in electric field. Here-to-fore the phenomenon has been regarded as of only academic interest as the μ_{ijmk} in simple dielectrics are exceedingly small of order 10^{-10} C/m. Recent measurements at Penn State have however shown values of flexoelectric μ_{ijkm} in cubic incipient ferroelectrics of order 100 $\mu\text{C}/\text{m}$ more than 6 orders larger, so now the phenomenon becomes of practical interest. Exploiting the elastic strain gradient realized in a barium strontium titanate: air macro-composite with Curie group symmetry 4mm we fabricate a piezoelectric composite containing no piezoelectric phase for which we measure $d_{33} = 6$ pC/N and calculate from the measured μ_{11} a similar value, demonstrating that charge separation in the composite is flexoelectric.

Unlike conventional piezoelectric composites the gradient driven flexoelectric system increases in sensitivity with decreasing scale and we predict that for achievable scales it should be possible to achieve d_{33} values in the range 300 ~600 pC/N. It is also interesting to note that in the gradient driven piezoelectric direct and converse effects are no longer equivalent so that sensing and actuation functions are separable. This feature highlights an interesting aspect of shape generated texture symmetry in composites which may have important consequence in other systems. Another very interesting feature is that the lead cation appears to be a killer for high flexoelectric coefficients so that successful flexoelectric piezoelectric composites will necessarily be lead free.

Ferroelectric nanowires : a combined experimental and theoretical investigation

L. Louis¹, W. Ma^{2, a}, P. Gemeiner³, B. Dkhil³, G. Geneste³, I. Ponomareva¹, L. Bellaiche¹,
N. Setter²

¹*Department of Physics, University of Arkansas, Fayetteville, Arkansas 72701, USA*

²*Ceramics Laboratory, Swiss Federal Institute of Technology (EPFL), CH-1015 Lausanne, Switzerland*

^a*Department of Physics, Shantou University, Shantou, Guangdong, 515063, P.R. China*

³*Laboratoire Structures, Propriétés et Modélisation des Solides, Ecole Centrale Paris, CNRS-UMR8580, Grande Voie des Vignes 92295, Châtenay-Malabry Cedex, France*

Phone : +33 1 41 13 15 86; Fax : +33 1 41 13 14 37; e-mail : brahim.dkhil@ecp.fr

Among the different possible ferroelectric nanostructures, the thin films (2-Dimensions) are, by far, the ones that have been the most investigated. As a result, the role of the substrate, growth orientation, surface termination, buffer layer or thickness on the ferroelectric properties of thin films begins to be rather well determined and understood despite some controversial issues. This situation, even if some unanswered questions remain, was achieved thanks to both theoretical calculations and experimental studies. On the other hand, studies on 0-Dimension ferroelectric nanostructures, namely nanoparticles, nanograins or nanodots are essentially investigated by experimental tools and for particles size up to 5nm. The only theoretical work (to our knowledge) is done by the groups of L. Bellaiche and H. Fu of the University of Arkansas. They predict that nanodots (less than 5nm-size) exhibit a vortex structure for their electrical dipoles, leading to a nonzero toroid moment of polarization rather than a net polarization, this latter being null. Such vortexes have never been observed, and even if they really exist, one has then to find a way to change the direction of rotation inside the vortex to make such nanodot suitable for applications.

In between the 2-D and 0-D ferroelectric nanostructures, the 1-D nanowires are rather scarcely studied, despite their potential in resulting to interesting phenomena and applications like for instance non-volatile memory devices with an integration density of 1 Terabit/cm². To the best of our knowledge, only few studies address the problems of ferroelectricity in such confined system.

In this presentation we will show new results obtained on KNbO₃ nanowires synthesized by hydrothermal method. The nanowires with a mean diameter of about 50nm and a mean length of about 5 μ m, exhibit the perovskite-like structure. X-ray diffraction and Raman techniques as a function of temperature were used to determine the phase transition sequence. Interestingly the temperatures of the transition from the cubic-tetragonal and tetragonal-orthorhombic phases are very close to the bulk ones. But surprisingly, the low-temperature ground state of the nanowire never reaches the bulk-like rhombohedral phase. Calculations based on first-principles confirm the absence of the rhombohedral phase for the low temperature state for the nanowires. A discussion between experiment and calculation will be provided.

Ferroelectric thin films investigated by x-ray diffraction

P.-E. Janolin¹, L. Bellaïche², B. Dkhil¹, M. El Marssi³, Yu.I. Golovko⁴, Bo-Kuai Lai², F. Le Marrec², V.M. Mukhortov^{4,5}, Yu. I. Yuzyuk⁵

¹Laboratoire Structures, Propriétés et Modélisation des Solides, CNRS-UMR8580, Ecole Centrale Paris, 92295 Châtenay-Malabry, France

²Physics Department, University of Arkansas, Fayetteville, Arkansas 72701, USA

³Laboratoire de Physique de la Matière Condensée, Université de Picardie Jules Verne, 80039 Amiens, France

⁴South Scientific Center RAS, Rostov-on-Don, 344006 Russia

⁵Faculty of Physics, South Federal University, Zorge 5, Rostov-on-Don, 344090 Russia
Phone : +33 1 41 13 15 86; Fax : +33 1 41 13 14 37; e-mail : brahim.dkhil@ecp.fr

A material can exhibit drastically different properties if deposited as a thin film or considered as a mechanically free bulk material. The differences in thermal expansion coefficients and crystal lattice parameters between the substrate and the film are considered as the main causes of the in-plane stress (up to several GPa) that arises in the film. This stress can be partially (or fully) relaxed through domains or dislocations formation. As a consequence the ferroelectric thin film properties and the associated phase transitions are strongly affected: shift of the transition temperature, change of the order parameter, increase of the diffuseness, change in the sequence of the phase transitions; it may even lead to new phases in the material.

This presentation is divided into three parts. In each part, our investigation was performed by using mainly X-Ray Diffraction as a function of temperature and the data are compared with recent theoretical calculations.

The first part is devoted to the structural analysis of epitaxially mono-oriented 100nm-thick film of $\text{Pb}(\text{Zr}_{0.2}\text{Ti}_{0.8})\text{O}_3$ (PZT) deposited by pulsed laser deposition (PLD) on [001]-oriented SrTiO_3 substrate. This study demonstrates that the substrate controls the temperature evolution of the in-plane film parameter which induces a non-cubic (tetragonal) and paraelectric high temperature phase up to the deposition temperature. From the lattice parameters it is possible to extract a value of the polarization after removing the pure elastic distortion imposed by the substrate at the deposition temperature.

The second part mainly concerns the temperature evolution of the polydomain structure of 100nm-thick PZT film deposited by PLD on [001]-oriented MgO substrate. Our analysis demonstrates that even in relatively strongly relaxed systems thanks to domains, the phase transitions and domain states remain strongly affected. Still the substrate plays a key role and the structure never reaches the expected high-temperature cubic phase.

Finally in a third part, a serie of $(\text{Ba}_{0.8}\text{Sr}_{0.2})\text{TiO}_3$ (BST) thin films were deposited on [001]-oriented MgO substrate by rf sputtering. Now, the thickness of the films varied from 6 up to 980 nm. The in-plane and out-of-plane lattice parameters were determined by means of x-ray diffraction as a function of temperature. Polarized Raman spectra were also studied on the same set of samples. Our analysis shows that the degree of stress (or equivalent misfit-strain) in the epitaxially grown thin films is a function of film thickness. This allows us to plot a thickness-temperature phase diagram comparable to the classical misfit-strain-temperature diagram. Possible symmetry changes as a function of temperature and as a function of film thickness are therefore discussed.

Ab initio calculations of the SrTiO₃, BaTiO₃, and PbTiO₃ (001), as well as BaTiO₃ and PbTiO₃ (011) surfaces

R.I. Eglitis, and J. Lee

School of Materials Science and Engineering, Sung Kyun Kwan University, Suwon 440-746, South Korea; e-mail: reglitis@uos.de; phone: +82-31-2994742

Numerous high technology applications, including catalysis, microelectronics, substrates for growth of high T_c superconductors etc., are based on thin films of ABO₃ perovskite ferroelectrics [1]. Several *ab initio* quantum mechanical [2,3] studies have dealt with the (001) surface of BaTiO₃, and SrTiO₃ crystals. Due to intensive development and progressive miniaturization of electronic devices, the electronic properties and atomic structure of the ABO₃ perovskite thin films have been extensively studied experimentally during the last years. However, according to our knowledge, there are no *ab initio* calculations performed for the BaTiO₃ and PbTiO₃ (011) surfaces.

To perform the first-principles density functional theory (DFT) calculations using Becke's three parameter method, combined with the non-local correlation functionals by Perdew and Wang (B3PW), we used the CRYSTAL computer code [4].

Our calculated atomic displacements for TiO₂ and BaO terminated BaTiO₃ (001) as well

as for TiO₂ and PbO terminated PbTiO₃ (001) surfaces are presented in Table 1. A comparison with the surface atomic displacements for the BaTiO₃ (001) surfaces obtained by other theoretical calculations performed by Padilla and Vanderbilt [2] by means of the local density approximation (LDA) and by Heifets *et al.* [5] using the classical shell model (SM) is also made in Table 1. For the PbTiO₃ (001) surface relaxation we compare our results with the *ab initio* calculations by Meyer *et al.* [3]. (see Table 1). The relaxation of surface metal atoms is much larger than that of oxygen ion, which leads to a considerable rumpling of the outermost plane.

The calculated surface energies of the relaxed BaTiO₃ (001) and (011) surfaces are presented in Table 2. In BaTiO₃, the surface energy of two differently terminated (001) surfaces is comparable each other. The surface energies of BaO and TiO₂ – terminated (001) surfaces are 1.19 eV and 1.07 eV per surface cell, respectively. Unlike the BaTiO₃ (001) surface, different terminations of the (011) surface lead to great differences in the surface energies. The lowest energy has the A-type O-terminated surface (1.72 eV). This is close to the energy of BaTiO₃ (001) surfaces. This result suggests that A – type O – terminated (011) surface and (001) surfaces can co-exist in BaTiO₃. The Ba – terminated BaTiO₃ (011) surface has a much higher surface energy of 3.24 eV, while the BaTiO₃ TiO – terminated (011) surface energy is 2.04 eV.

Our calculated surface energies for PbTiO₃ (001) surfaces show, that also in PbTiO₃ both TiO₂ (0.74 eV) and PbO (0.83 eV) terminated (001) surfaces are stable and has a comparable surface energies. Nevertheless, the TiO₂ terminated (001) surface is slightly more stable for both materials, as BaO or PbO terminated (001) surface.

According to the results of our calculations, the energetically most unfavorable, and thereby most unstable is metal (Ba or Pb) terminated BaTiO₃ (3.24 V) or PbTiO₃ (2.03 eV) (011) surface. It is interesting to notice, that the surface energies for the O terminated, A type BaTiO₃ and PbTiO₃ (011) surfaces coincide (1.72 eV).

Table 1. Atomic displacements with respect to atomic positions on unrelaxed BaTiO₃, and PbTiO₃ (001) surfaces (in percent of bulk lattice constant).

BaTiO ₃ (001) surface relaxation						PbTiO ₃ (001) surface relaxation				
Termination	Layer	Ion	This study	SM [5]	LDA [2]	Termination	Layer	Ion	This study	LDA PW [3]
BaO	1	Ba2+	-1.99	-3.72	-2.79	PbO	1	Pb2+	-3.82	-4.36
		O2-	-0.63	1.00	-1.40			O2-	-0.31	-0.46
	2	Ti4+	1.74	1.25	0.92		2	Ti4+	3.07	2.39
		O2-	1.40	0.76	0.48			O2-	2.30	1.21
	3	Ba2+		-0.51	0.53		3	Pb2+		-1.37
		O2-		0.16	0.26			O2-		-0.20
TiO ₂	1	Ti4+	-3.08	-2.72	-3.89	TiO ₂	1	Ti4+	-2.81	-3.40
		O2-	-0.35	-0.94	-1.63			O2-	0.31	-0.34
	2	Ba2+	2.51	2.19	1.31		2	Pb2+	5.32	4.53
		O2-	0.38	-0.17	-0.62			O2-	1.28	0.43
	3	Ti4+		-0.33	-0.75		3	Ti4+		-0.92
		O2-		-0.01	-0.35			O2-		-0.27

Table 2. Calculated surface energies for BaTiO₃ and PbTiO₃ (in electronvolt per unit cell area) using the hybrid B3PW method.

BaTiO ₃ (001) and (011) surface energies			
Surface	Type	B3PW	SM [5]
(001)	TiO ₂ terminated	1.07	1.40
	BaO terminated	1.19	1.45
(011)	TiO terminated	2.04	2.35
	Ba terminated	3.24	4.14
	O terminated, A type	1.72	1.81
PbTiO ₃ (001) and (011) surface energies			
Surface	Type	B3PW	
(001)	TiO ₂ terminated	0.74	
	PbO terminated	0.83	
(011)	TiO terminated	1.36	
	Pb terminated	2.03	
	O terminated, A type	1.72	

References:

1. M. Dawber, K.M. Rabe, and J.F. Scott, *Reviews of Modern Physics* **77**, 1083 (2005).
2. J. Padilla, and D. Vanderbilt, *Phys. Rev. B* **56**, 1625 (1997).
3. B. Meyer, J. Padilla, and D. Vanderbilt, *Faraday Discussions* **114**, 395 (1999).
4. V.R. Saunders, R. Dovesi, C. Roetti, M. Causa, N.M. Harrison, R. Orlando, C.M. Zicovich-Wilson, *CRYSTAL2003 Users Manual* (University of Torino, Torino, 2003).
5. E. Heifets, E. Kotomin, and J. Maier, *Surf. Sci.* **462**, 19 (2000).

Electronic structure of perfect and defective $\text{PbZrO}_3(001)$: *Ab initio* simulations

R.I. Eglitis¹, A. Gopejenko², S. Piskunov², Yu.F. Zhukovskii², and J. Lee¹

¹ School of Materials Science and Engineering, Sung Kyun Kwan University, Suwon, South Korea; e-mail: reglitis@uos.de; phone: +82-31-2994742

² Institute of Solid State Physics, University of Latvia, Riga, Latvia

Lead zirconate PbZrO_3 due to its antiferroelectric behavior, is technologically important for applications involving actuators and high energy storage devices [1]. PbZrO_3 is also a parent compound of $\text{PbZr}_{1-x}\text{Ti}_x\text{O}_3$ solid solutions, which are of high scientific and technological interest for their ferroelectricity and piezoelectricity observed over a wide range of compositions. Recently, antiferroelectric PbZrO_3 thin film heterostructures have been found to be radiation resistant and suggested as a promising candidate for application in radiation environments [2], including diagnostic materials and bolometers for thermonuclear reactors.

We present and discuss the results of calculations of the electronic structure of $\text{PbZrO}_3(001)$ surfaces. First-principles DFT calculations have been performed using the exchange-correlation B3PW functional involving a “*hybrid*” of non-local Fock exact exchange and exchange potentials as implemented in *CRYSTAL-03* code [3] The band gap obtained for PbZrO_3 (PZ) bulk (cubic phase) is in satisfactory agreement with the experimental data (3.8 vs. 3.7 eV in experiment). Atomic displacements of ZrO_2 and PbO terminated PbZrO_3 (001) surfaces are given in Tables I (a) and I (b). Our calculations predict Pb displacement on the PbO terminated surface to be approximately two times larger than that for Zr atom on the ZrO_2 terminated PbZrO_3 (001) surface. All upper layer atoms for both terminations relax inwards (Tables Ia,b).

Table I. Atomic relaxation of uppermost five layers (in percent of the lattice constant) for (a) ZrO_2 terminated and (b) PbO terminated PbZrO_3 (001) surface by means of DFT hybrid B3PW method. Positive (negative) values refer to the displacements in the direction outwards (inwards) the surface.

(a)	Layer	Ion	B3PW (Δz % of a_0)	(b)	Layer	Ion	B3PW (Δz % of a_0)
1.	1.	Zr^{4+}	-2.97	1.	1.	Pb^{2+}	-6.95
		O^{2-}	-1.36			O^{2-}	-0.04
2.	2.	Pb^{2+}	5.54	2.	2.	Zr^{4+}	2.57
		O^{2-}	0.84			O^{2-}	1.08
3.	3.	Zr^{4+}	-1.12	3.	3.	Pb^{2+}	-2.63
		O^{2-}	-0.53			O^{2-}	-0.26
4.	4.	Pb^{2+}	1.39	4.	4.	Zr^{4+}	0.58
		O^{2-}	0.14			O^{2-}	0.15
5.	5.	Zr^{4+}	-0.27	5.	5.	Pb^{2+}	-0.62
		O^{2-}	-0.12			O^{2-}	-0.08

According to the results of our calculations, the surface rumpling for PbO terminated PbZrO_3 (001) surface is much larger than for the ZrO_2 terminated PbZrO_3 (001) surface. Our calculations predict

(see Table II) compression of the distance between the first and second planes, and its expansion for the second and third planes.

Table II. The calculated surface rumpling s and relative displacements (Δd_{ij}) for the three near-surface planes of PbO and TiO₂ terminated (001) surfaces (in percent of bulk lattice constant).

Method	PbO – terminated			ZrO ₂ - terminated		
	s	Δd_{12}	Δd_{23}	s	Δd_{12}	Δd_{23}
B3PW	6.91	-9.52	+5.20	1.61	-8.51	+6.66

Table III. The calculated (001) surface energies for both PbO and ZrO₂ terminations.

Method	PbO-terminated	ZrO ₂ -terminated
B3PW	0.93*	0.95*

* energy values are presented in eV *per* surface cell

According to results of our calculations, both ZrO₂- and PbO-terminated (001) PZ surfaces are stable, and since the surfaces energies for PbO and ZrO₂ (001) terminations are close, (0.93 and 0.95 eV, respectively) (see Table III) they could be produced simultaneously after cleavage of PZ bulk crystal. We have found a strong increase of the Zr-O bond covalency near the ZrO₂-terminated (001) surface as compared to the PZ bulk. Defective PbZrO₃(001) surface have been modeled by creating of the *F*-center (*i.e.* neutral oxygen vacancy trapping up to two electrons) on the ZrO₂-terminated surface of cubic PZ phase. *F*-center induces an additional defect level in the band gap of PbZrO₃(001) and affects the electron density distribution in its vicinity, substantially influencing the electronic properties of the material. We compare our calculated data with experimental results whenever it is possible.

References:

- [1] B. Xu, Y. Ye, L.E. Cross, J. Appl. Phys. **87**, 2507 (2000).
- [2] R. Bittner, K. Hummer, H.W. Weber, K. Kundzins, A. Sternberg, D.A. Lesnyh, D.V. Kulikov, Yu.V. Trushin, J. Appl. Phys. **96**, 3239 (2004).
- [3] V.R. Saunders, R. Dovesi, C. Roetti, R. Orlando, C.M. Zicovich-Wilson, N.M. Harrison, K. Doll, B. Civalleri, I.J. Bush, Ph. D'Arco, and M. Llunell M. (2003) *CRYSTAL-2003 User's Manual*. (University of Turino, Torino, Italy).

Ab initio calculations of BaZrO₃ (001) and (011) surfaces

R.I. Eglitis, and J. Lee

School of Materials Science and Engineering, Sung Kyun Kwan University, Suwon, South Korea;
e-mail: reglitis@uos.de; phone: +82-31-2994742

We present and discuss the results of calculations of BaZrO₃ (001) surface relaxation and rumpling with two different terminations (BaO and ZrO₂), and BaZrO₃ (011) polar surface relaxation with two terminations (Ba and ZrO). These are based on a hybrid Hartree-Fock and density-functional theory exchange functionals, using Beckes three-parameter method, combined with the nonlocal correlation functionals by Perdew and Wang [1]. According to the results of our calculations, all upper layer atoms for ZrO₂ and BaO terminated BaZrO₃ (001) surfaces relax inwards (see Tables I a,b). In (001) surface, the displacement of Ba on the BaO terminated surface is larger than that of Zr atom on the ZrO₂ terminated surface (see Tables I a,b).

Table I. Atomic relaxation of uppermost three layers (in percent of the lattice constant) for (a) ZrO₂ terminated and (b) BaO terminated BaZrO₃ (001) surface by means of hybrid B3PW method. Positive (negative) values refer to the displacements in the direction outwards (inwards) the surface.

(a)	Layer	Ion	B3PW (Δz % of a_0)	(b)	Layer	Ion	B3PW (Δz % of a_0)
1.		Zr ⁴⁺	-1.79	1.		Ba ²⁺	-4.30
		O ²⁻	-1.70			O ²⁻	-1.23
2.		Ba ²⁺	1.94	2.		Zr ⁴⁺	0.47
		O ²⁻	0.85			O ²⁻	0.18
3.		Zr ⁴⁺	-0.03	3.		Ba ²⁺	-0.01
		O ²⁻	0.00			O ²⁻	-0.14

According to the results of our calculations, the surface rumpling for BaO terminated BaZrO₃ (001) surface is much larger than for the ZrO₂ terminated BaZrO₃ (001) surface. Our calculations predict (see Table II) compression of the distance between the first and second planes, and its expansion for the second and third planes.

Table II. The calculated surface rumpling s and relative displacements (Δd_{ij}) for the three near-surface planes of BaO and ZrO₂ terminated (001) surfaces (in percent of bulk lattice constant).

Method	BaO – terminated			ZrO ₂ - terminated		
	s	Δd_{12}	Δd_{23}	s	Δd_{12}	Δd_{23}
B3PW	3.07	-4.77	+0.48	0.09	-3.73	+1.97

Table III. Atomic relaxation of BaZrO₃ (001) surface (in percent of the lattice constant) for two terminations, calculated by means of the *ab initio* B3PW method. Positive sign corresponds to outward atomic displacements (toward the vacuum).

Layer	Ion	B3PW, (Δz % of a_0)
ZrO terminated		
1	Zr ⁴⁺	-6.61
1	O ²⁻	+3.35
2	O ²⁻	-0.29
3	Ba ²⁺	-1.51
3	O ²⁻	-3.54
3	Zr ⁴⁺	+0.90
Ba terminated		
1	Ba ²⁺	-11.81
2	O ²⁻	+0.66
3	Zr ⁴⁺	+0.09
3	O ²⁻	-0.07
3	Ba ²⁺	+0.71

Table IV. Calculated surface energies for BaZrO₃ (001) and (011) surfaces (in electronvolt per unit cell area) using the hybrid B3PW method.

BaZrO ₃ (001) and (011) surface energies		
Surface	Type	B3PW
(001)	ZrO ₂ terminated	1.31
	BaO terminated	1.30
(011)	Ba terminated	2.90
	ZrO terminated	3.09

We found that relaxation magnitudes of Ba and ZrO terminated BaZrO₃ (011) surface upper layer metal atoms are stronger as it was for the BaZrO₃ (001) surface upper layer atoms. While, the metal atoms for the Ba and ZrO terminated BaZrO₃ (011) surfaces strongly relax inwards, the oxygen atoms on ZrO terminated BaZrO₃ (011) surface upper layer relax outwards by 3.35 % of the lattice constant a_0 (see Table III). The results of calculations for the surface energy of BaZrO₃ (001) and (011) surfaces are presented in Table IV. Both BaO (1.30 eV) and ZrO₂ (1.31 eV) terminated surfaces are stable and energetically equally favorable. Our calculated surface energies of Ba (2.90 eV) and ZrO (3.09 eV) terminated BaZrO₃ (011) surfaces is larger than those of BaO and ZrO₂ terminated BaZrO₃ (001) surfaces.

References:

- [1] V.R. Saunders, R. Dovesi, C. Roetti, R. Orlando, C.M. Zicovich-Wilson, N.M. Harrison, K. Doll, B. Civalleri, I.J. Bush, Ph. D'Arco, and M. Llunell M. (2003) *CRYSTAL-2003 User's Manual*. (University of Turino, Torino, Italy).

Designing a hugh magnetoelectric response in epitaxially strained thin films from first principles

Craig J. Fennie*¹ and Karin M. Rabe²

¹*Center for Nanoscale Materials and Materials Science
Division, Argonne National Laboratory, Argonne IL 60439*

²*Department of Physics and Astronomy, Rutgers University, Piscataway, New Jersey 08854, USA*

There is great interest in multiferroic materials in which ferroelectric (FE) and ferromagnetic (FM) ordering not only coexist, but in which the electrical polarization \mathbf{P} and the magnetization \mathbf{M} are large and strongly coupled [1, 2]. One challenge in identifying strongly coupled FM-FE's that has received considerable attention in the past [3] is the scarcity of such materials in nature, as most insulators (a requirement for ferroelectricity) are paraelectric (PE) and antiferromagnetic (AFM). With the recent advances in first-principles density-functional methods for predicting [4] and in novel synthetic techniques for growing new FM-FE multiferroics, the focus has now turned to how to produce a strong coupling between the two distinct order parameters [5]. Recently, attention has focused on a mechanism in which magnetic order itself breaks inversion symmetry [6–9]. Based on this, remarkable control of the FE state by an applied magnetic field has been demonstrated in some rare-earth manganites [10, 11], however, the natural scale of the spontaneous polarization thus induced is very small, of the order of nC/cm². Furthermore, the magnetic state appears to be rather insensitive to an applied electric field for this class of materials.

As a result, it is clearly advantageous to explore other possible mechanisms for strongly coupled multiferroism. A fruitful starting point for identifying such mechanisms is the observation, recently discussed by Tokura [5], that the basic physics of a strong \mathbf{M} - \mathbf{P} coupling involves a competition between different ordered states, e.g. between a FM-FE state and an AFM-PE state. In this Talk, we present a new approach for designing a strongly coupled multiferroic in which the interplay of spins, optical phonons, and strain leads to such a competition [12].

The criteria that a bulk system must satisfy for this proposed mechanism to be realized are as follows: (1) It must be an AFM-PE insulator in which at least one infrared-active (ir) phonon is coupled to the magnetic order, (2) the spins in the AFM ground state should align with the application of a magnetic field of modest strength, (3) this alignment should decrease the frequency of the spin-coupled ir-active phonon, and, (4) the key to our approach, the ir-active mode of interest must be strongly coupled to strain.

In the remainder of the Talk we present a first-principles calculation of the ground-state epitaxial phase diagram for the magnetic perovskite EuTiO₃ [13] demonstrating that this system is indeed a realization of our proposed mechanism for strongly coupled multiferroicity. Epitaxial strain can have profound effects on the properties of thin films [14]. In our design strategy we use epitaxial strain to dial into the region of the phase diagram where a spin-phonon-driven destabilization of the lattice actually occurs. The FM-FE phase thus produced is a low-lying state competing with the AFM-PE ground state. As a direct result of this competition, magnetic and electric phase control can be achieved by an applied electric and magnetic field respectively. As the polarization of the low-lying FM-FE phase

* fennie@anl.gov

results from the freezing-in of a soft polar phonon triggered by the spin-phonon coupling, it is of the same order of magnitude as prototypical soft-mode FEs ($\mu\text{C}/\text{cm}^2$) as seen in Fig. 1(a). In addition, as the phase-control region is approached from the low strain side, the magnetocapacitance diverges, Fig. 1(b), while on the high strain side there may be, in some cases, a phase boundary between the AFM-PE phase control region and a true equilibrium FM-FE phase. The use of epitaxial strain to exploit the relatively modest spin-phonon effects displayed by many bulk materials provides an exciting new design strategy in the pursuit of strong **M-P** coupled multiferroics.

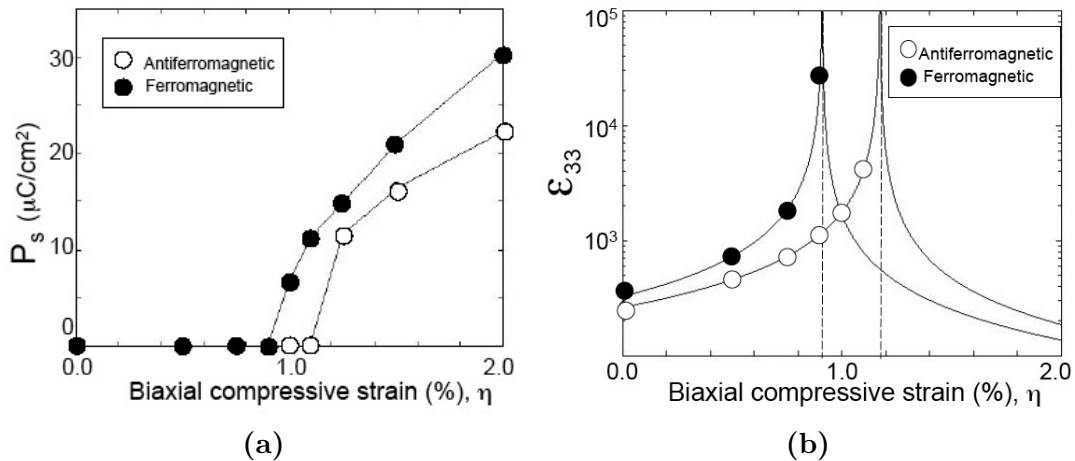


FIG. 1: (a) Spontaneous polarization P_s and (b) static dielectric constant ϵ_{33} as a function of epitaxial compressive strain η .

-
- [1] M. Fiebig, J. Phys. D: Appl. Phys. **38**, R123 (2005).
 - [2] N. A. Spaldin and M. Fiebig, Science **309**, 391 (2005).
 - [3] N.A. Hill, J. Phys. Chem. B., **104**, 6694 (2000).
 - [4] C. Ederer and N. A. Spaldin, Current opinion in solid state and materials science **9**, 128 (2006).
 - [5] Y. Tokura, Science **312**, 1481 (2006).
 - [6] L. C. Chapon, P. G. Radaelli, G. R. Blake, S. Park, and S. -W. Cheong, Phys. Rev. Lett. **96**, 097601 (2006).
 - [7] A. B. Harris, J. Appl. Phys. **99**, 08E303 (2006).
 - [8] M. Mostovoy, Phys. Rev. Lett. **96**, 067601 (2006).
 - [9] I. A. Sergienko and E. Dagotto, Phys. Rev. B **73**, 094434 (2006).
 - [10] N. Hur, S. Park, P. A. Sharma, J. S. Ahn, S. Guha, and S. -W. Cheong, Nature **429**, 392 (2004).
 - [11] T. Kimura, T. Goto, H. Shintani, K. Ishizaka, T. Arima, and Y. Tokura. Nature **426**, 55 (2003).
 - [12] C. J. Fennie and K. M. Rabe, Phys. Rev. Lett. **97**, 267602 (2006).
 - [13] T. Katsufuji and H. Takagi, Phys. Rev. B **64**, 054415 (2001).
 - [14] K. M. Rabe, Current opinion in solid state and materials science **9**, 122 (2006).

Comparative study of vacancy formation energies in PbTiO₃ and BaTiO₃

Zeyad Alahmed and Huaxiang Fu

Department of Physics, University of Arkansas, Fayetteville, Arkansas 72701, USA

BaTiO₃ and PbTiO₃ are two paradigm examples of ferroelectrics due to their distinct ferroelectric properties. With respect to BaTiO₃, PbTiO₃ displays a far larger c/a strain, stronger spontaneous polarization, and a deeper potential well of FE instability. While there have been numerous studies devoted to these structural differences, far fewer studies are conducted to understand difference and/or similarity of these two materials in terms of tendency for forming vacancy (in fact, theoretical studies of defects in ferroelectrics are rather limited in general[1–4]). For example, TiO₆ octahedra exist in both substances and have similar structure. Does it indicate that the formation energy for oxygen vacancy, under oxygen-poor condition, be close in two materials? (Under oxygen-rich condition, this question is of less interest since oxygen vacancies will not take place.) On a separate issue, the strong tetragonality (that exists in PbTiO₃ but to a considerably less extent in BaTiO₃) results in two non-equivalent oxygen sites. What difference will this tetragonality lead to the formation energy of oxygen vacancy? Another question concerns the A-site vacancy. It is well known that in PbTiO₃ there is a strong covalent hybridization between Pb atom and O atom. Because of this hybridization shall we expect a larger formation energy for V_{Pb} in PbTiO₃ than for V_{Ba} in BaTiO₃? Furthermore, how does the consideration of chemical potentials alter the conclusion?

Formation energy of vacating atom j is, as described above, the energy required to move this atom from the ABO₃ solid into the gas-phase reservoir. This energy, denoted as $\Delta E_f^v(j)$ can be written as a function of the atomic chemical potential as follows:

$$\Delta E_f^v(j) = E_{\text{tot}}(\text{ABO}_3, [j]) + E_{\text{tot}}(j) + \mu_j - E_{\text{tot}}(\text{ABO}_3) \quad (1)$$

where $E_{\text{tot}}(\text{ABO}_3)$ and $E_{\text{tot}}(\text{ABO}_3, [j])$ are the total energy of the perfect perovskite solid and the solid containing one j -specie vacancy. $E_{\text{tot}}(j)$ is the total energy per atom in elemental solid, and μ_j the chemical potential of this specie. The first three terms in the right side of Eq.(1) is the total energy of the system after the vacancy is created. For convenience, Eq.1 can be also written as $\Delta E_f^v(j) = \Delta G(j) + \mu_j$, where $\Delta G(j) = E_{\text{tot}}(\text{ABO}_3, [j]) - E_{\text{tot}}(\text{ABO}_3) + E_{\text{tot}}(j)$ is the vacancy formation energy when chemical potential μ_j is zero.

Using density functional total-energy calculations and structural minimization we determined the formation enthalpy of various compounds, and critical quantity ΔG which is associated with the energy of creating a vacancy in the host solid and the vacated atom is placed in the lattice site of the relevant elemental solid. We further ob-

tained analytically, according to thermodynamical laws, the formulae that specify the valid chemical-potential range of gas-phase reservoirs in equilibrium with the ferroelectric solids. Both the formation enthalpy of compounds and the valid chemical potentials, as determined here in this study, will be fairly helpful for investigating other types of defects and related properties. By combining the studies of ΔG and chemical potentials, formation energies of neutral vacancies under different environment conditions are calculated for all species. Comparing vacancies in PbTiO₃ and BaTiO₃ further reveals interesting differences of defect energetics in these two paradigm ferroelectrics. Our specific conclusions are summarized as follows.

(i) The oxygen gas reservoir in equilibrium with BaTiO₃ can vary its chemical potential over a much wider range than the oxygen reservoir in equilibrium with PbTiO₃ can, and more quantitatively, $-5.87 \leq \mu_{\text{O}} \leq 0$ eV in the BT system, while $-2.98 \leq \mu_{\text{O}} \leq 0$ eV in the PT case. (ii) For a fixed μ_{O} , μ_{Pb} and μ_{Ti} of gas reservoirs in PbTiO₃ system must be carefully adjusted in order to avoid the occurrence of secondary phases, since the valid region of μ_{Pb} or μ_{Ti} has a narrow width of only 0.39 eV. This is different in BaTiO₃, where μ_{Ba} or μ_{Ti} can be adjusted over a significant range of 1.62 eV. (iii) ΔG is predicted to be on the order of about 4.5, 6.0, 9.5, and 15.0 eV for Pb, O, Ba, and Ti vacancies, respectively. Thus, $\Delta G(\text{Pb}) < \Delta G(\text{O}) < \Delta G(\text{Ba}) < \Delta G(\text{Ti})$. (iv) While Pb and Ba are both predominantly ionic in ferroelectric solids (Pb-O bonds have some covalent character), their vacancy formation energies ΔG are dramatically different, however, and $\Delta G(\text{Pb})$ is about 5 eV smaller than $\Delta G(\text{Ba})$. Furthermore, although O atoms form strong covalent bonds with Ti, its $\Delta G(\text{O})$ is surprisingly smaller than the ΔG of Ba. (v) The strong tetragonality in PbTiO₃ does not introduce significant effect to the vacancy formation energy of two non-equivalent oxygen atoms. (vi) Oxygen chemical potential can be effectively used to modify the vacancy formation energy (and thus the vacancy concentration) of oxygen specie and *other* species. For instance, our calculations show that by varying μ_{O} , $\Delta E_f^v(\text{Ti})$ of a Ti vacancy can be drastically reduced from 15.65 eV to 3.67 eV, while $\Delta E_f^v(\text{Ba})$ changes from 9.69eV to merely 2.43 eV. (vii) Under oxygen-rich condition, formation of a Pb vacancy in PbTiO₃ needs an energy within the range of [1.47, 1.86] eV, while formation of a Ba-site vacancy takes [2.43, 4.05] eV. The comparable and small formation energies of A-site vacancies thus indicate that, when oxygen is rich, both Pb and Ba vacancies are very likely to appear in corresponding ferroelectrics. (viii) For the limiting case when oxygen is poor, our calculations predict that in BaTiO₃ formation of an

O vacancy needs only 0.43 eV, and the concentration of V_O is thus to be exceedingly high.

- [1] S. Poykko and D.J. Chadi, Phys. Rev. Lett. **83**, 1231 (1999).
- [2] L. He and D. Vanderbilt, Phys. Rev. B **68**, 134103 (2003).
- [3] E. Cockayne and B. P. Burton, Phys. Rev. B **69**, 144116 (2004).
- [4] H. Moriwake, Int. J. Quantum Chem. **99**, 824 (2004).

Embryonic Domain Structure Investigated by means of Simultaneous Measurements of Brillouin Scattering and Light Deflection

Y. Fujii^{1*}, S. Yoshioka², and S. Kinoshita²

¹*Department of Applied Physics and Chemistry, The University of Electro-Communications, Chofu, Tokyo 182-8585, Japan*

²*Graduate School of Frontier Biosciences, Osaka University, Suita, Osaka 565-0821, Japan*

*Phone: +81-42-443-5454; E-mail: y.fujii@osa.org

When a crystal undergoes a ferroelastic phase transition, nonzero strain comes to appear spontaneously. However, the direction of the spontaneous strain is not usually uniform overall the crystal, but it differs in one domain to another. The causes of this domain formation has been investigated experimentally and theoretically for a long time.^[1] Here we experimentally investigate the initial process of a ferroelastic domain formation by simultaneously applying two completely different methods—light deflection method and Brillouin scattering spectroscopy. The former method utilizes light reflection/refraction phenomenon at domain boundaries caused by the difference in the direction of optical principal axes between adjacent ferroelastic domains. This method is a powerful tool to probe the initial stage of the ferroelastic domain formation near T_c , because the formation process can be observed as a gradual increase of the deflected light intensity which can be detected by a highly sensitive photon detection system even when the spontaneous strain is very small. The latter spectroscopic method gives us the information on the dynamical instability of an acoustic phonon mode, which is essential for the phase transition mechanism.

We studied a ferroelastic crystal, deuterated potassium trihydrogen selenite (DKTS, $\text{KD}_3(\text{SeO}_3)_2$), which is known to undergo a second-order ferroelastic phase transition changing the crystal symmetry from the orthorhombic to monoclinic phase at $T_c \approx 27^\circ\text{C}$. In the lower temperature phase, s_4 component of the spontaneous strain appears.^[2] This crystal have one of two kinds of a stripe-like domain pattern called b- and c-domain, where the domain boundaries were parallel to (001) and (010) plane, respectively. The deflected light was observed using liquid N_2 cooled CCD camera system (Photometrics, Spectra 9000), and Brillouin scattering spectroscopy was simul-

taneously performed by using a Sandercock-type tandem Fabry-Perot interferometer using an optical system described previously.^[3] The sample temperature was controlled within the accuracy of 0.008°C using a temperature controller (Technol Seven, C531-8). The formation of b-domain structure was investigated in the present study.

Figure 1(a) shows the temperature dependence of the deflected light intensity integrated in angle from $8 \sim 26^\circ$ from the direction of an incident He-Ne laser. It is found that the de-

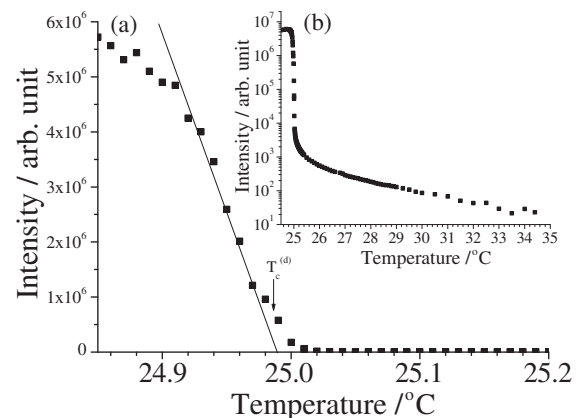


Figure 1: Temperature dependence of the deflected light intensity integrated over the angular range from $8 \sim 26^\circ$ in linear(a) and logarithmic(b) scale.

flected light intensity drastically increases below 25°C indicating that the crystal undergoes the phase transition and the domain structure appears around that temperature (fig. 1(a)). Since the deflected light is theoretically expected to be proportional to $(T - T_c)^{[4]}$, we have determined the temperature at which the extrapolated line for the data in the region from 24.92 to 24.98°C crosses the horizontal axis to be $24.990 \pm 0.006^\circ\text{C}$, called $T_c^{(d)}$. When the same data is plotted in a logarithmic scale, we can notice that the deflected light still exists in higher temperature region, where no domain structure is expected to exist as shown in fig. 1(b). The deflected light intensity de-

creases continuously and can be observed at least up to 35 °C. Figure 2 represents the combined results obtained by the two methods applied simultaneously. We have repeated three times these experiments. We notice that $T_c^{(d)}$ is slightly lower than $T_c^{(B)}$ that is the phase transition temperature determined as the temperature when the frequency of Brillouin peak shift becomes lowest. A fitting analysis gives $(T_c^{(B)} - T_c^{(d)})$ to be 44 ± 11 mK, 50 ± 11 mK and 41 ± 9 mK, for three measurements. The good agreement among three sets of results confirms that $T_c^{(d)}$ is certainly lower than $T_c^{(B)}$ by about 40 mK. This fact is thought to deeply relate with the nature of the growing domain structure.

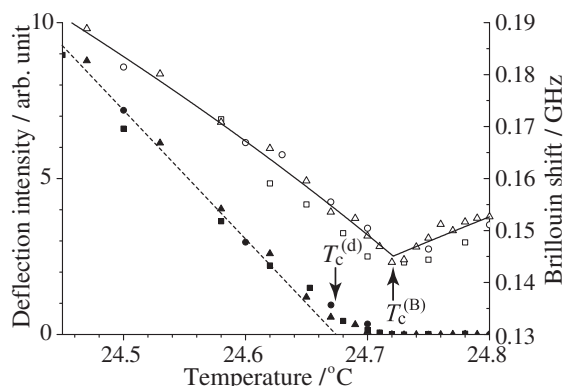


Figure 2: Temperature dependence of the intensity of the deflected light (filled symbols) and Brillouin peak shift (open symbols) obtained by simultaneous measurements. Three types of symbol shapes indicate three sets of results obtained on different days.

The light deflection caused above T_c and the observed difference between $T_c^{(B)}$ and $T_c^{(d)}$ can be explained by an idea of existence of embryo of the domain structure that exists above T_c . The embryonic domain is considered to be a continuous modulation of the small strain induced by the intrinsic stress field caused by impurities or defects.^[3] The embryonic domain finally grows up to the full-grown one as the temperature decreases much below the phase transition temperature. A model assuming an embryonic domain structure reasonably reproduces the difference between $T_c^{(d)}$ and $T_c^{(B)}$ as follows. We consider Ginzburg-Landau (GL) free energy, $\int \left(g_0 + \frac{\alpha(T-T_c)}{2} \eta(x)^2 + \frac{B}{4} \eta(x)^4 + \frac{D}{2} (\nabla \eta(x))^2 \right) dV$, where g_0 is the part of the potential density which does not depend on order parameter η . A calculation of minimizing GL free energy reveals that the thickness of domain

boundary is expected to be thicker near T_c , and the thick domain wall implies that the principal axis of the refractive indicatrix is gradually rotates inside the wall. This gradual change works to reduce the deflected light intensity owing to destructive interference. A similar destructive interference is known as “anti-reflection effect”, which is observed at an interface of two isotropic media with the refractive index varying gradually.^[5] We have simulated the temperature dependence of the deflected light intensity assuming existence of the embryonic domain structure as shown in fig. 3. The calculated result (dashed line) reproduces the temperature shift of $T_c^{(d)}$ from $T_c^{(B)}$, while a solid line indicates that in which no gradual region is assumed. The apparent shift was found to be roughly proportional to D/α . Further, the result also represents the behavior that the intensity of light deviates from the linear relation around $T_c^{(d)}$. Studies of the origins of the embryonic domain structure are now in progress.

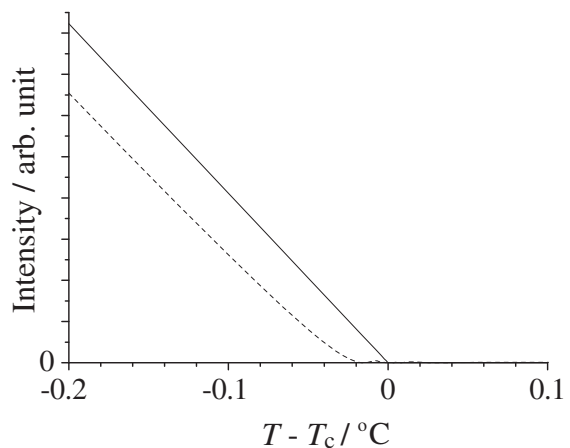


Figure 3: Simulation of the temperature dependence of the deflected light intensity. The dashed line is expected from the model assuming the embryonic domain structure, while the solid one indicates $I \propto T - T_c$ ($T < T_c$), which is expected by the model of discontinuous domain boundaries.

Acknowledgement - This work was supported by 21st century COE Program “Innovation in Coherent Optical Science”

- [1] E. Salje, *Phase transitions in ferroelastic and co-elastic crystals* (Cambridge University Press, U. K., 1990)
- [2] R. Blinc *et. al*, Phys. Rev. B **22**, 3486(1980)
- [3] Y. Fujii *et. al*, Ferroelectrics **334**, 287(2006)
- [4] S. Kinoshita *et. al*, Phys. Rev. B **50**, 5834(1994)
- [5] J. Rayleigh, Proc. Lond. Math. Soc. **11**, 51(1880)

Neutron Scattering Study of Zone Boundary Tilt Modes in PMN

Ian Swainson,¹ Christopher Stock,² Peter M. Gehring,³ Guangyong Xu,⁴ and H. Luo⁵

¹National Research Council, Canadian Neutron Beam Centre, Chalk River Labs, Chalk River, Ontario K0J 1J0, Canada

²Dept. of Physics and Astronomy, Johns Hopkins University, Baltimore, MD 21218

³NIST Center for Neutron Research, National Institute of Standards and Technology, Gaithersburg, MD 20899-8562

⁴Condensed Matter Physics and Materials Science Dept., Brookhaven National Laboratory, Upton, NY 11973-5000

⁵Shanghai Institute of Ceramics, Chinese Academy of Sciences, Shanghai, China 201800

We have made extensive measurements on a large (2 cm³) single crystal specimen of PbMg_{1/3}Nb_{2/3}O₃ (PMN) at 300 K and 600 K using the neutron time-of-flight scattering technique. The crystal was oriented in the [HHL] zone and mounted inside a closed-cycle ³He refrigerator with access to temperatures from 30 to 650 K. The neutron scattering measurements were performed at the NIST Center for Neutron Research on the Disk Chopper Spectrometer (DCS) in an effort to characterize the low-frequency lattice dynamics of this prototypical relaxor system along the major symmetry directions $\Gamma \rightarrow R$, $\Gamma \rightarrow M$, and $\Gamma \rightarrow X$.

Figure 1 displays an intensity map of the inelastic scattering measured at room temperature in pure PMN along the reciprocal lattice direction [0,0,L] for fixed H = [1.5,1.5,0]. These data demonstrate continuity along the line M-T-R thus implying that the scattering intensities visible at the M and R-point zone boundaries have a common origin. By virtue of the fact that the modes at M and R are the zone boundary acoustics, as shown in Fig. 2, we may conclude unambiguously that these are the tilt modes [1-3].

The data in Fig. 1 also show the presence of an anomalous continuum of scattering that extends from each of the M and R-points down to the elastic channel. As this scattering weakens at 600 K, it suggests the presence of soft zone boundary modes that are likely the origin of the temperature dependent superlattice peaks that have been observed in both x-ray and neutron measurements [4]. It is interesting to note that temperature dependence nearly tracks the zone centre soft optic mode which is associated with the development of short-range polar correlations at low temperatures.

The excitations at both the R and M-points are well defined in momentum, but also extremely broad in energy. This suggests a form of very periodic disorder associated with the tilting of octahedra. Such continuums of scattering have not been observed in either PbTiO₃ or PMN doped with 60% PbTiO₃, both of which undergo transitions to long-range ferroelectric ground states, but have been seen in calcite [5]. These results may suggest that it is the random fields associated with the structural disorder in PMN that prevents the formation of long-ranged ferroelectric correlations, and also that allow the existence of large piezoelectric coefficients.

References

- [1] MT Dove AP Giddy V Heine, "Rigid unit mode model of displacive phase transitions in framework silicates," *Trans Am Cryst Assoc* **27**, 65-74 (1991).
- [2] C Howard and HT Stokes, "Group-Theoretical Analysis of Octahedral Tilting in Perovskites," *Acta Cryst* **B54**, 782-789 (1998).
- [3] IP Swainson, "Tilt and acoustic instabilities in ABX_4 , A_2BX_4 and ABX_3 perovskite structure types: their role in the incommensurate phases of the organic-inorganic perovskites," *Acta Cryst* **B61**, 616-626 (2005). [1] [4] A Tkachuk and H Chen, *Proceedings of the Fundamental Physics of Ferroelectrics*, AIP Conference Proceedings vol. 677, Edited by Peter K. Davies and David J. Singh, p. 55 (2003).
- [5] MT Dove, ME Hagen, MJ Harris, BM Powell, U Steigenberger, and B Winkler, "Anomalous inelastic neutron scattering from calcite," *J. Phys.: Condens. Matter* **4**, 2761 (1992).

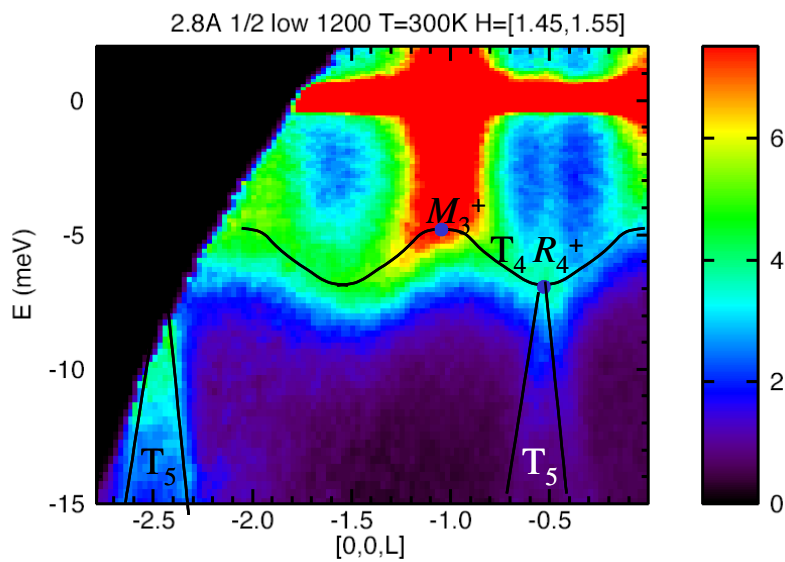


Fig. 1: Data measured at 300 K on single crystal PMN at a neutron wavelength of 2.8 Angstroms. The figure is a slice at fixed $H = [1.5, 1.5, 0]$ and shows a continuous dispersion between the M and R-points along T. Note also the anomalous continuum of inelastic scattering underneath the M and R-points that extend to the elastic region.

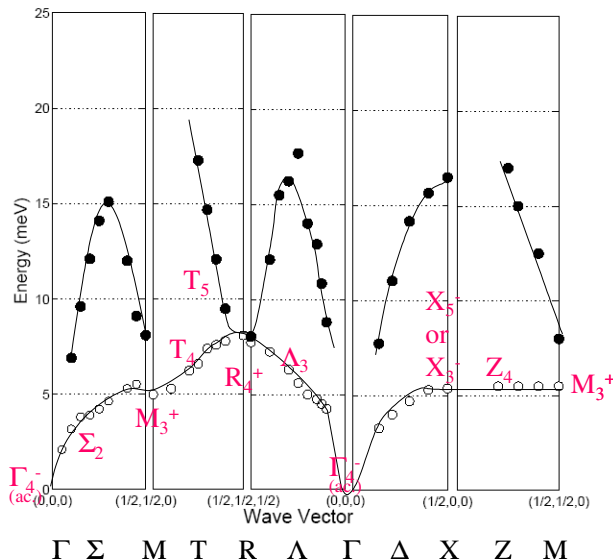


Fig. 2: Dispersions of PMN derived from both triple-axis and time-of-flight neutron data. Mode assignments were made using the Isotropy code.

Probing Domain Configurations in Nanoscale Ferroelectrics

A. Schilling¹, D. Byrne¹, T. B. Adams¹, P. R. Evans¹, R. J. Pollard¹, R. M. Bowman¹ and J. M. Gregg¹, G. Catalan², J. F. Scott² and F. D. Morrison³

¹Centre for Nanostructured Media, Queen's University Belfast, Belfast, U. K.
Phone:44-(0)2890973309; Fax:44-(0)2890973997; e-mail: m.gregg@qub.ac.uk

²Department of Earth Sciences, University of Cambridge, Cambridge, U. K.

³School of Chemistry, University of St. Andrews, St. Andrews, U. K.

A focused ion beam microscope (FIB) has been used to cut thin film lamellae, nanoscale columns and more complex nanoscale shapes (such as rings and 'picture frames') from single crystals of ferroelectric material (mostly BaTiO₃). Scanning Transmission Electron Microscopy (STEM) has then been used as the dominant technique for examining the domain configurations that occur, in such single crystal nanomorphologies, on cooling through the Curie temperature. The almost free-standing single crystal nature of the systems examined has allowed for observations of domains to be made with little of the complications that normally arise from microstructure, defects and uncontrolled surface boundary conditions in conventionally made thin films and nanostructures.

In all of the single crystal systems examined to date, conventional 90° stripe domains persist irrespective of geometry and size (figures 1 and 2) even in nanocolumns with cross-sections less than 100nm x 100nm. The periodicity of the stripe domains varies relatively systematically and can be rationalized by considering the tension between an increase in energy associated with increased domain size, and an increase in energy associated with an increased density of domain walls (and hence decreased domain size). Arguments for this balance in energy terms follow the continuum models developed by Kittel [1] and by Mitsui and Furuichi [2] to determine equilibrium behaviour in ferroic systems which have been shape limited in one direction (slabs of material). We have tested such models for describing BaTiO₃ lamellae [3] and extended them to consider shape limitation in two directions, *x* and *y* (column geometry) [4]:

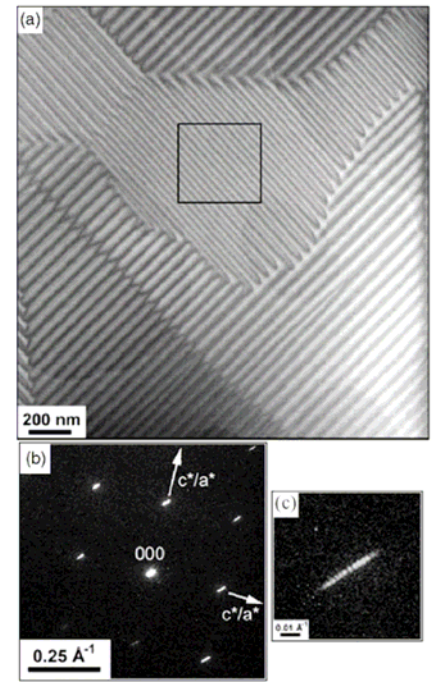


Figure 1. STEM image of stripe domains on BaTiO₃ lamella (a), with diffraction patterns (b) & (c) confirming the {110} domain wall orientations and domain period.

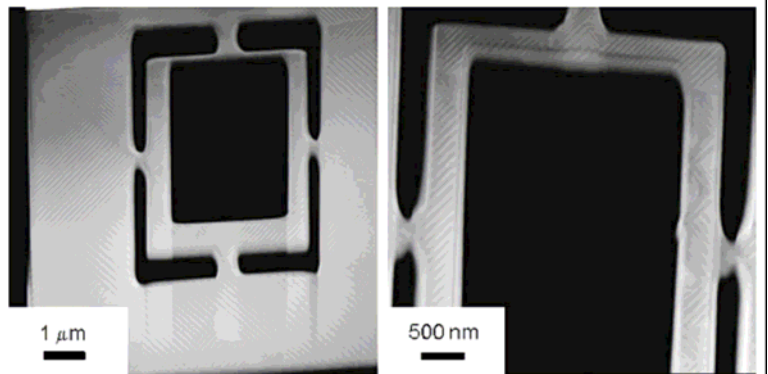


Figure 2. STEM images showing both the morphology of 'picture frames' cut using FIB, and the stripe domains present on each of the limbs of the frames.

$$\omega^2 = \frac{\sqrt{2}}{2} \frac{\sigma}{\frac{U_x}{x} + \frac{U_y}{y}} \quad (1)$$

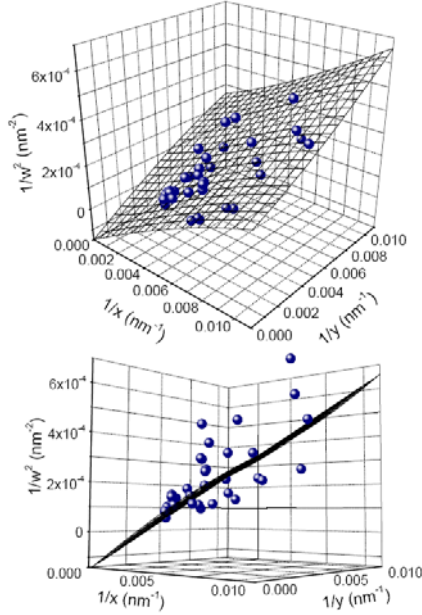


Figure 3. Plots of domain width as a function of the cross-sectional dimensions in nanocolumns of BaTiO₃

where ω is the domain width, σ the domain wall energy per unit area, U_x and U_y are constants proportional to the components of the energy density of the domain contributed by the presence of the external surfaces perpendicular to nominally defined x and y axes respectively; x is the column dimension in the x direction, and y the dimension in the y direction (z is taken to be large).

Rearranging equation (1) as:

$$\omega^{-2} = \frac{2}{\sqrt{2}\sigma} (U_x x^{-1} + U_y y^{-1})$$
 allows comparison with

experimental data in which plotting ω^{-2} against x^{-1} and y^{-1} in a three dimensional graph should yield a plane of best fit. Figure 3 shows that such a description looks reasonable. This is somewhat surprising, as the original treatments by Kittel and by Mitsui and Furuichi sought to describe an equilibrium behaviour, but in the absence of external shape constraint, the lowest energy states for our nanocolumns should be monodomain, with polar axis parallel to z . It seems that kinetics through the Curie temperature frustrate the attainment of true equilibrium, and instead the trade-off between the domain energy and domain wall energy determine the configurations observed.

In further work we have sought to examine domain behaviour in much smaller nanoshapes, motivated by atomistic simulations that suggest the possibility of polarization vortices in ferroelectrics [5] analogous to those already seen in soft ferromagnets. While no vortex domain states have yet been observed, some progress in the self-assembly of nanorings has been made [6] and will be expanded further in the talk.

- [1] C. Kittel, Phys. Rev. **70**, 965 (1946)
- [2] T. Mitsui and J. Furuichi, Phys. Rev. **90**, 193 (1953)
- [3] A. Schilling, T. B. Adams, R. M. Bowman, J. M. Gregg, G. Catalan and J. F. Scott, Phys. Rev. B, **74**, 024115 (2006)
- [4] A. Schilling, R. M. Bowman and J. M. Gregg, G. Catalan and J. F. Scott, Appl. Phys. Lett. **89**, 212902 (2006); G. Catalan, J. F. Scott, A. Schilling and J. M. Gregg *submitted to JPCM* 2007
- [5] H. Fu, L. Bellaiche, Phys. Rev. Lett., **91**, 257601 (2003); I. Kornev, H. Fu, L. Bellaiche, Phys. Rev. Lett., **93**, 196104 (2004); I. I. Naumov, L. Bellaiche, H. Fu, Nature, **432**, 737 (2004)
- [6] X. H. Zhu, P. R. Evans, D. Byrne, A. Schilling, C. Douglas, R. J. Pollard, R. M. Bowman, J. M. Gregg, F. D. Morrison and J. F. Scott, Appl. Phys. Lett. **89**, 122913 (2006)

Relationship between local structure and relaxor behavior in perovskite oxides

Ilya Grinberg¹, Pavol Juhas², Peter K. Davies³ and Andrew M. Rappe¹

¹*The Makineni Theoretical Laboratories, Dept. of Chemistry,
University of Pennsylvania, Philadelphia, PA 19104-6323,*

³*Dept. of Physics and Astronomy, Michigan State University East Lansing,
MI 48824-2320, ²Dept. of Materials Science and Engineering,
University of Pennsylvania, Philadelphia, PA 19104-6323*

(Dated: January 14, 2007)

Despite intensive investigations over the past five decades, the microscopic origins of the fascinating dielectric properties of ABO₃ relaxor ferroelectrics are currently poorly understood. Here, we show that the frequency dispersion that is the hallmark of relaxor behavior is quantitatively related to the crystal chemical characteristics of the solid solution. Density functional theory is used in conjunction with experimental determination of cation arrangement to identify the 0 K structural motifs. These are then used to parameterize a simple phenomenological Landau theory that predicts the universal dependence of frequency dispersion on the solid solution cation arrangement and off-center cation displacements.

Since the first synthesis of the classic PbMg_{1/3}Nb_{2/3}O₃ (PMN) material in the 1961 [1], relaxor ferroelectrics have been the subject of ongoing experimental and theoretical investigation [2–7] due to their fundamental scientific interest and their importance in technological applications such as capacitors and piezoelectric devices. One of the most intriguing properties of relaxors is the frequency dispersion of the temperature maximum of the dielectric constant. Despite intense research, the relationship between perovskite composition and relaxor properties is poorly understood. While it is known that heterovalency and a degree of disorder on the B-site are necessary for appearance of relaxor behavior in Pb-based systems, quantitative relationships between local structure and relaxor dispersion are lacking.

To understand the origins of the dispersion observed in Pb-based relaxors, we search for correlations between the experimentally observed differences between the temperature maximum of the dielectric constant at 100 Hz and 1 MHz (ΔT_{disp}) and crystal chemical parameters such as ionic valence (bonding) and ionic displacement. Relaxor behavior is usually observed in perovskites with overbonded and underbonded O-atoms, since this leads to fluctuation in the local potential energy surface felt by the Pb cations. As a measure of the degree of these fluctuations, we use the second moment of the valence of the two B-cation nearest neighbors of each oxygen atom ($\langle V^2 \rangle$), defined as

$$\langle V^2 \rangle = \frac{1}{N_{\text{O}}} \sum_i (V_{i,1}^B + V_{i,2}^B - \overline{V^B})^2 \quad (1)$$

where the i index runs over all of the O atoms and $V_{i,1}$ and $V_{i,2}$ are the valences of the two nearest B-cation neighbors of the i th O atom. The first moment of the oxygen atom B-cation neighbor valence $\overline{V^B}$ is equal to four in all Pb-based perovskites.

The other relevant crystal chemical parameter is the average B-cation displacement away from the high-symmetry cubic structure. Larger B-cation off-center

displacements allow the overbonding (underbonding) of oxygen atoms to be alleviated by motion of the B-cations away from (toward) the O atom, tending to stabilize normal ferroelectric phases relative to relaxor or other disordered phases.

The B-cation arrangement in many perovskites is unknown, preventing accurate computation of $\langle V^2 \rangle$. We therefore examine relaxors that exhibit B-cation ordering within the framework of the random-site model [8]. For such systems, $\langle V^2 \rangle$ can be computed exactly. Experimental dispersion data is available for 22 such systems [8–12]. To obtain average values of B-cation displacements for these systems, we perform density functional theory (DFT) calculations using the local density approximation (LDA).

Combining the two crystal chemical parameters, we propose a simple linear relationship between $D_{\text{B,avg}}$, $\langle V^2 \rangle$ and ΔT_{disp} , such that

$$\Delta T_{\text{disp}} = a_V \langle V^2 \rangle - a_D D_{\text{B,avg}} + C, \quad (2)$$

where a_V , a_D and C are constants and fit the experimental ΔT_{disp} to the theoretical $D_{\text{B,avg}}$ and $\langle V^2 \rangle$ data. The ΔT_{disp} predicted by the fit a_V , a_D and C (13 K, 438 K/Å and 56.5 K respectively) are in good agreement with the observed ΔT_{disp} values as shown in Figure 1.

The rather simplistic assumption of linear dependence of ΔT_{disp} on $\langle V^2 \rangle$ and $D_{\text{B,avg}}$ in Eq. 2 is sufficient to demonstrate that a close and quantitative relationship exists between frequency dispersion and crystal chemical parameters (Figure 1). However, careful examination of the data yields a more physically insightful picture. Following the usual treatment of phase transitions, we model the compositional relaxor to ferroelectric phase transition with Landau theory using ΔT_{disp} as the order parameter.

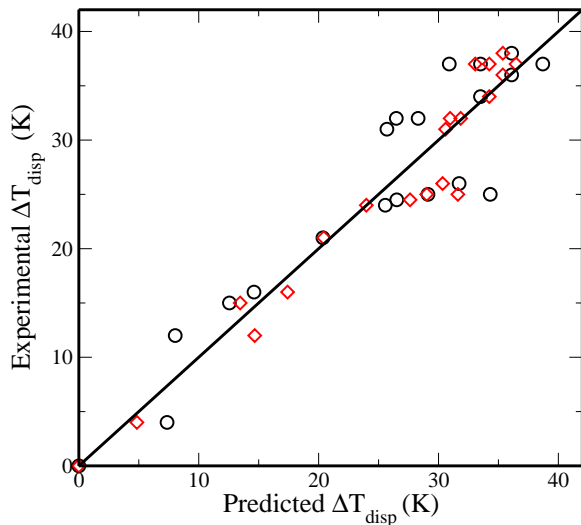


FIG. 1: Correlation between experimental ΔT_{disp} values and those predicted from fit ($a_v=13$ K, $a_D=438$ K/Å, $C=56.5$ K) of Eq. 2 (circles) and Eq. 5 ($a_0=-727$ K², $a_v=394$ K², $a_d=2.02 \times 10^4$ K² and $k=28.6$ Å⁻¹) (diamonds) to crystal chemical data for 22 ordered Pb-based relaxor compositions. Good agreement with experiment is found. The average errors for ΔT_{disp} predictions using Eqns. 2 and 5 are 3.0 K and 1.9 K respectively.

$$G = G_0 - \frac{1}{2}A(\langle V^2 \rangle, D_{B,\text{avg}})\Delta T_{\text{disp}}^2 + \frac{1}{4}\Delta T_{\text{disp}}^4, \quad (3)$$

$$\Delta T_{\text{disp,equil}}^2 = A(\langle V^2 \rangle, D_{B,\text{avg}}) \quad (4)$$

$$A(\langle V^2 \rangle, D_{B,\text{avg}}) = a_0 + a_v \langle V^2 \rangle + a_d e^{-kD_{B,\text{avg}}} \quad (5)$$

where G is the free energy of the relaxor phase, G_0 is

the energy of the parent ferroelectric phase and the A Landau coefficient is a function of $\langle V^2 \rangle$ and $D_{B,\text{avg}}$ (a_0 , a_v , a_d and k are constants).

The exponential dependence on $D_{B,\text{avg}}$ is due to exponential variation of bonding overlap with interatomic distances changed by the cation displacement. The correlation between the experimentally observed ΔT_{disp} values and ΔT_{disp} values calculated using a_0 , a_v , a_d and k fit to the experimental $D_{B,\text{avg}}$ disp data is shown in Figure 1. The more physical nature of the modeling gives rise to smaller deviations from experimental results than for the corresponding predictions using the simple linear form in Eq. 2. This indicates that the Landau theory of the relaxor-ferroelectric transition encapsulated by Eq. 5 provides good model of experimental data. Since the crystal chemical parameters in the model involve individual interatomic interactions, our work strongly suggests that some local, Å-scale interatomic interactions cause relaxor behavior. This supports previously suggested models of relaxors as ferroelectrics with local frustration of the ferroelectric coupling by antiferroelectric-like interactions [13, 14].

This work was supported by the Office of Naval Research, under grant numbers N-000014-00-1-0372 and N00014-01-1-0860 and through the Center for Piezoelectrics by Design. We also acknowledge the support of the National Science Foundation, through the MRSEC program, grant No. DMR05-20020. Computational support was provided by the Center for Piezoelectrics by Design, the DoD HPCMO, DURIP and by the NSF CRIF program, Grant CHE-0131132. We would also like to thank I-W. Chen and A. A. Bokov for stimulating discussions.

-
- [1] G. A. Smolenskii, V. A. Isupov, A. I. Agranovskaya, and S. N. Popov, *Sov. Phys. Solid State* **2**, 2584 (1961).
 [2] I. K. Jeong, T. W. Darling, J. K. Lee, T. Proffen, R. H. Heffner, J. S. Park, K. S. Hong, W. Dmowski, and T. Egami, *Phys. Rev. Lett.* **94**, 147602 1 (2005).
 [3] R. Blinc, J. Dolinsek, A. Gregorovic, B. Zalar, C. Filipic, Z. Kutnjak, A. Levstik, and R. Pirc, *Phys. Rev. Lett.* **83**, 424 (1999).
 [4] R. Blinc, V. Laguta, and B. Zalar, *Phys. Rev. Lett.* **91**, 247601 (2003).
 [5] V. Westphal, W. Kleeman, and M. D. Glinchuk, *Phys. Rev. Lett.* **68**, 847 (1992).
 [6] P. M. Gehring, S. E. Park, and G. Shirane, *Phys. Rev. Lett.* **84**, 5216 (2000).
 [7] J. Hemberger, P. Lunkenheimer, R. Fichtl, H. von Nidda, V. Tsurkan, and A. Loidl, *Nature* **434**, 364 (2005).
 [8] M. A. Akbas and P. K. Davies, *J. Am. Ceram. Soc.* **80**, 2933 (1997).
 [9] L. Farber and P. K. Davies, *J. Am. Ceram. Soc.* **86**, 1861 (2003).
 [10] M. A. Akbas and P. K. Davies, *International Journal of Inorganic Materials* **3**, 123 (2001).
 [11] A. Kumar, K. Prasad, S. N. Choudhary, and R. N. P. Choudhary, *Material Lett.* **58**, 3395 (2004).
 [12] Y.-H. Bing, A. A. Bokov, Z.-G. Ye, B. Noheda, and G. Shirane, *J. Phys.-Cond. Matt.* **17**, 2493 (2005).
 [13] R. Fisch, *Phys. Rev. B* **67**, 094110 (2003).
 [14] I.-W. Chen, *J. Phys. Chem. Solids* **61**, 197 (2000).

Towards a phase-field model for BaTiO₃ with realistic domain wall properties

J. Hlinka and P. Márton

Institute of Physics, Academy of Sciences of the Czech Republic, Na Slovance 2, 18221 Praha 8, Czech Republic

Phase-field type computer simulation is starting to be a standard tool for studying properties of multiaxial ferroelectrics, especially in the case of thin films[1–10]. In general, along with similar effective-hamiltonian techniques, such approaches allow to extend substantially the accessible space- and time perimeter of the realistic computer modeling. The advantage of the phase-field models is that they normally go around the problem of anharmonic temperature effects by using the phenomenological Landau free energy functional as the effective potential. However, surprisingly little attention was paid to the quantitative appreciation of the interaction terms, associated with spatial inhomogeneity of the order parameter field. Thus, so far the actual values of time and spatial units in the phase-field simulations were only very approximately known, unlike in the case of the effective hamiltonian methods, where the values of all model parameters are usually systematically derived from a microscopic theory.

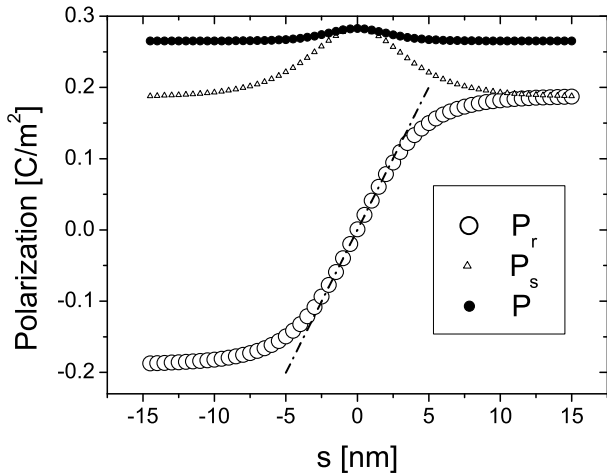


FIG. 1: Polarization profiles across a fully compensated 90° head-to-tail domain wall in room temperature BaTiO₃ (calculated *without* long-range dipole-dipole interactions from the GGLD model discussed here). Larger point symbols stay for tangential component P_r , smaller ones for the normal component P_s (perpendicular to the domain wall) and for the modulus $P = |\mathbf{P}| = \sqrt{P_s^2 + P_r^2}$ of the polarization, respectively. Solution fulfills Saint-Venant compatibility relations and the usual boundary conditions as considered for example in Refs. 16, 17.

Recently, we have proposed a complete list of model parameters for a generalized Ginzburg-Landau-Devonshire (GGLD) model of BaTiO₃. In this list, adopted parameter values are derived solely from vari-

ous bulk measurements: parametrization of the Landau-Devonshire potential[11] is that of Refs. 12, 13 (6-th order expansion) or that of Ref. 14 (8-th order expansion), while the magnitudes of anisotropic gradient energy and the long-range dipolar energy terms were derived from available experimental data in Ref. 15.

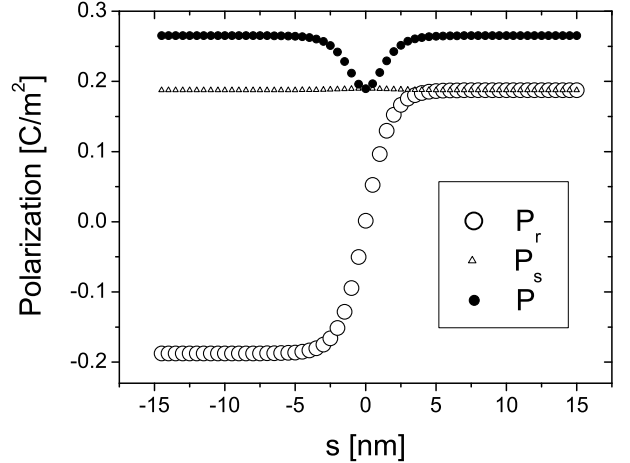


FIG. 2: Polarization profiles across 90° head-to-tail domain wall in room temperature BaTiO₃ calculated for the present model *including* the dipole-dipole term. Larger point symbols stay for P_r , smaller ones for P_s and $|\mathbf{P}|$, respectively.

method	90° wall thickness [nm]	source (year)
TEM	20	Ref. 25 (1964)
TEM	4-6	Ref. 18 (1972)
TEM	7-12	Ref. 23 (1974)
electron holography	1-2.5	Ref. 19 (1992)
electron holography	2- 5	Ref. 20 (1993)
X-ray diffraction	4-6	Ref. 21 (1997)
X-ray diffraction	14	Ref. 22 (1999)
AFM/SNOM	25	Ref. 24 (2000)
GGLD	3.6	Ref. 15 (2006)

TABLE I: Experimental estimates of 90° wall thickness in BaTiO₃ in comparison with the prediction of the GGLD model. TEM, AFM and SNOM stands for transmission electron microscopy, atomic force microscopy, scanning near-field optical microscopy.

We believe that such a qualitative GGLD model can be extremely useful for predictions of phenomena associated with the lengthscales of few or few tens of nanometers. Among others, it turns out that present model yields the

thickness of the 180-degree domain wall which is almost identical to the ab-initio predicted value[27] and it also gives a very reasonable prediction for 90-degree domain walls, which makes a challenge for both experimental and ab-initio investigations (see TABLE I). Moreover, phase-field simulations with this model has produced domain patterns[30] with a very similar morphology to that observed in experiments.

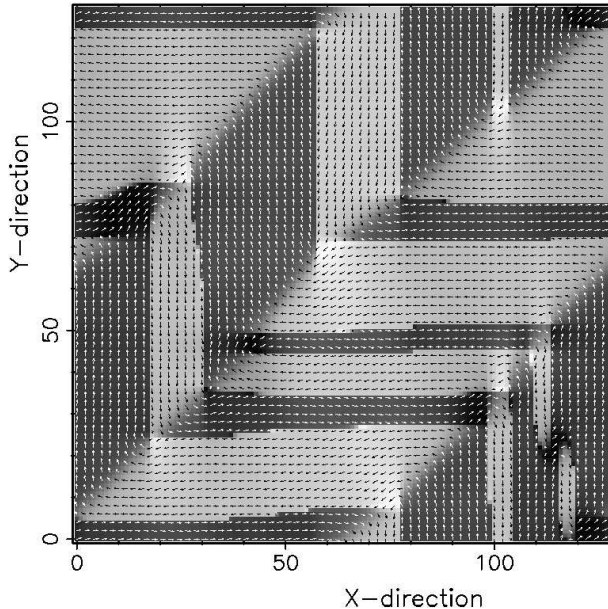


FIG. 3: (LEFT SIDE) Typical fish-bone type domain structure pattern showing interpenetrating systems of 90-degree and 180-degree domain walls, produced by phase-field computer simulations with the proposed BaTiO₃ GGLD model. Proper balance of elastic and dipole-dipole interactions as well and anisotropic gradient terms are responsible for the observed pattern. Displayed results corresponds to a fully clamped 2D geometry with room-temperature parameters and no macroscopic depolarization field (short-cut electric boundary conditions).

In this contribution we shall review the present approach, discussing its possible applications, advantages and disadvantages. We shall give examples of predicted domain wall properties, such as domain wall thickness, energy density, chirality[26] and mobility. Finally, the meaning and the importance of the pronounced anisotropy of the gradient term will be illustrated in phase-field simulated patterns of tetragonal and orthorhombic domain structures.

Acknowledgments

This work has been supported by the Grant Agency of the Czech Republic (projects 202/05/H003 and 202/06/0411).

-
- [1] S. Nambu and D.A. Sagala, Phys. Rev. B **50**, 5838 (1994).
 - [2] S. Semenovskaya and A. G. Khachatryan, J. Appl. Phys. **83**, 5125 (1998).
 - [3] H.L. Hu and L.Q. Chen, Mater. Sci. Eng., A **238**, 182 (1997).
 - [4] H.L. Hu and L.Q. Chen, J. Am. Ceram. Soc. **81**, 492 (1998).
 - [5] J. Slutsker, A. Artemev, and A. L. Roytburd, J. Appl. Phys. **91**, 9049 (2002).
 - [6] R. Ahluwalia, T. Lookman, A. Saxena and W. Cao, condmat 0308232, (2003).
 - [7] R. Ahluwalia, T. Lookman, A. Saxena and W. Cao, Appl. Phys. Lett. **84**, 3450 (2004).
 - [8] D.A. Tenne et al, Science **313**, 1614 (2006).
 - [9] Y. L. Li and L. Q. Chen, Appl. Phys. Lett. **88**, 072905 (2006).
 - [10] Y. L. Li, S. Y. Hu, Z. K. Liu, and L. Q. Chen, Appl. Phys. Lett. **78**, 3878 (2006).
 - [11] A.F. Devonshire, Phil. Mag. **40**, 1040 (1940).
 - [12] A.J. Bell, J. Appl. Phys. **89**, 3907 (2001).
 - [13] A.J. Bell and L.E. Cross, Ferroelectrics **59**, 197 (1984).
 - [14] Y.L. Li, L.E. Cross, and L.Q. Chen, J. Appl. Phys. **98**, 064101 (2005).
 - [15] J. Hlinka and P. Marton, Phys. Rev. B **74**, 104104 (2006).
 - [16] V. A. Zhirnov, Zh. Eksp. Teor. Fiz. **35**, 1175 (1958). [Sov. Phys. JETP **35**, 822 (1959)].
 - [17] W. Cao and L.E. Cross, Phys. Rev. **44**, 5 (1991).
 - [18] S.I. Yakunin, V.V. Shakmanov, G.V. Spivak, and N.V. Vasil'eva, Fiz. Tverd. Tela (Leningrad) **14**, 373 (1972); Soviet Physics - Solid State **14**, 310 (1972).
 - [19] X. Zhang, T. Hashimoto, and D. C. Joy, Appl. Phys. Lett. **60**, 784 (1992).
 - [20] X. Zhang, D. C. Joy, Y. Zhang, T. Hashimoto, L. Allard and T. A. Nolan, Ultramicroscopy **51**, 21 (1993).
 - [21] N. Floquet, C.M. Valot, M.T. Mesnier, J.C. Niepce, L. Normand, A. Thorel, R. Kilaas, J. Phys. (France) III **7**, 1105 (1997).
 - [22] N. Floquet, C. Valot, Ferroelectrics **234**, 107 (1999).
 - [23] M.D. Dennis and R.C. Bradt, J. Appl. Phys. **45**, 1931 (1974).
 - [24] L.M. Eng and H.J. Guntherodt, Ferroelectrics **236**, 35, (2000).
 - [25] M. Tanaka and G. Honjo, J. Phys. Soc. Jpn. **19**, 954 (1964).
 - [26] B. Houchmandzadeh, J. Lajzerowicz and E. Salje, J. Phys. Cond. Matter. **3**, 5163 (1991).
 - [27] J. Padilla, W. Zhong, and D. Vanderbilt, Phys. Rev. B **53**, R5969 (1996).
 - [28] B. Meyer and D. Vanderbilt, Phys. Rev. B **65**, 104111 (2002).
 - [29] R. C. Bradt and G. S. Ansell, J. Appl. Phys. **38**, 5407 (1967).
 - [30] P. Marton and J. Hlinka, Phase Transitions **79**, 351 (2006).

Neutron Scattering Study of the Phase Transition(s) in the Mixed Ferroelectric Single Crystal $\text{KTa}_{0.83}\text{Nb}_{0.17}\text{O}_3$

¹E.Iolin, ¹J.Toulouse, ²R.Erwin

Physics Department of Lehigh University, Bethlehem, PA 18015

NIST, Gaithersburg, MD 20899

Phone: 215-673-3252; e-mail eiolin@netzero.net, eui206@lehigh.edu, jt02@lehigh.edu

Relaxor ferroelectrics $\text{A}(\text{B}'\text{B}'')\text{O}_3$ are characterized by the mixed occupancy of the B site. In $\text{Pb}(\text{Zn}_{1/3}\text{Nb}_{2/3})\text{O}_3$ (PZN), the B site can be occupied by either niobium (valence +5) or zinc(+2) and in $\text{Pb}(\text{Mg}_{1/3}\text{Nb}_{2/3})\text{O}_3$ (PMN) by either niobium (+5) or magnesium (+2). Therefore chemically ordered regions exist in PZN and PMN. In $\text{K}(\text{Ta}_{1-x}\text{Nb}_x)\text{O}_3$ (KTN), the B site can be occupied by either niobium or tantalum, both with the same valence of +5. Therefore chemically ordered regions are absent in KTN. KNbO_3 exhibits a series of ferroelectric phase transitions. In contrast KTaO_3 is described as an incipient ferroelectric down to low temperature. It was shown by D.Singh (Phys Rev B, 53, 176, 1964-1) that the curves of energy vs displacement of the transition ion with respect to the oxygen octahedral are qualitatively different for the case of KNbO_3 and KTaO_3 . KTN could be considered a highly polarized system with random forces created by the Nb ions interacting with the soft mode displacements in the host matrix.

Here we report the inelastic neutron scattering results obtained on a single crystal, $\text{KTa}_{0.83}\text{Nb}_{0.17}\text{O}_3$. Measurements were done at the triple axis spectrometer BT-9 at NCNR (NIST), in the regime of fixed incident energy 14.7 meV. Constant Q and constant E scans were performed in the experiment. We studied scattering by the transverse acoustic (TA) and optic (TO) modes along $(Q_x, 2, 0)$. Phonon data were taken as a function of temperature in the range 100K to 310K, which covers the dynamical processes of interest. An example of data is shown at the Fig.1. The TO dynamics are illustrated in Figs. 2, 3, and 4.

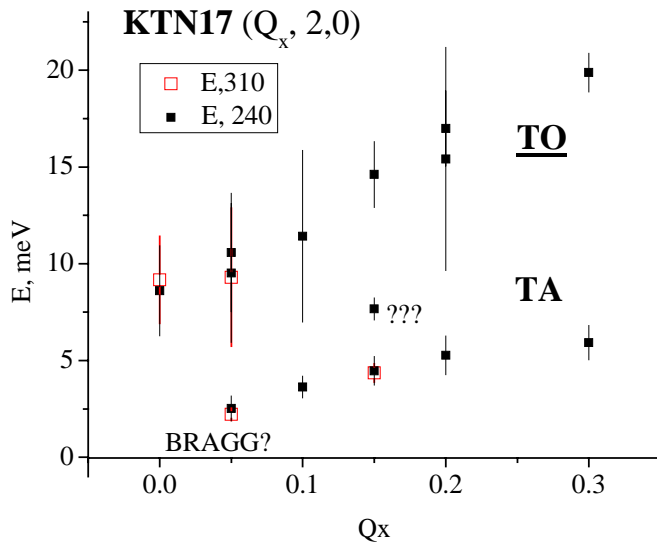


Fig.1 Dispersion curves at $T=310\text{K}$ and $T=240\text{K}$. The width of the neutron peak is shown as vertical bars. The width is relatively large in the range $Q_x=0$ to $Q_x=0.1$ and $E>6\text{meV}$, indicating damped excitations in this region.

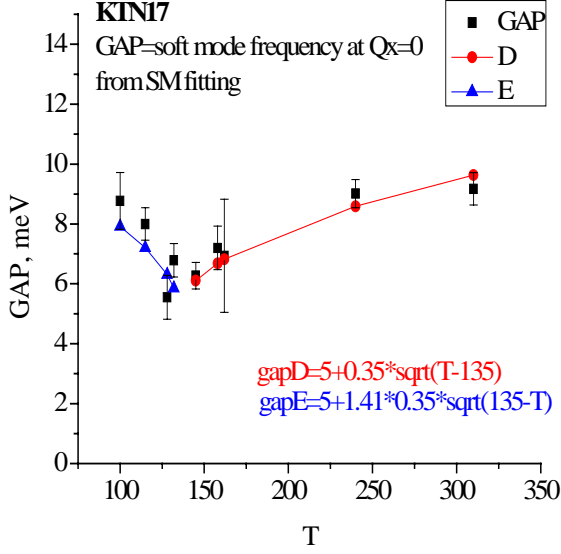


Fig.2. Value of TOW frequency at $Q_x=0$ vs temperature. Soft mode frequency was fitted in a frame of mean-field theory. Curve GAP(T) is similar to the ordinary soft mode behavior at the second order phase transition, $T_c=135$ K. However, the value of gap is not equal to zero at $T=T_c$.

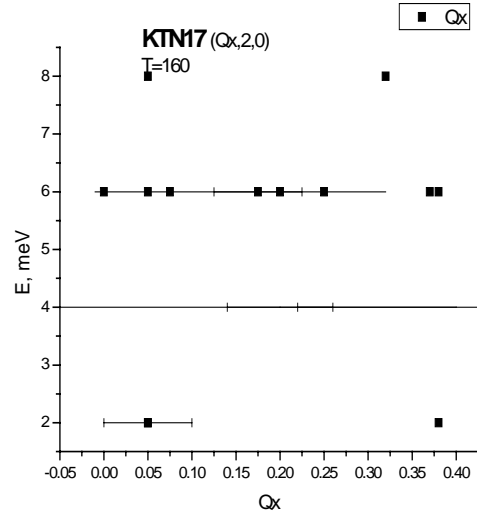
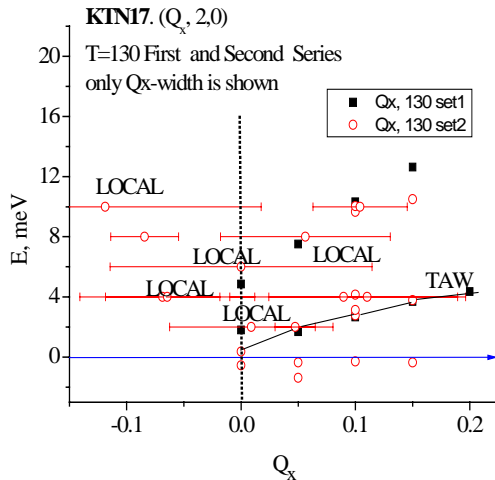


Fig.3. $T=160$ K, constant E method. It is practically impossible to find peak position at Q_x axis when $E=6$ meV. This circumstance can be considered as evidence of the phonon localization inside of crystal.

As part of their extensive investigation of the KTN system, J.Toulouse and R.K.Pattnaik studied the dielectric properties of a 15.7%Nb-KTN crystal (J.Phys.Chem. Solids, v. 57, p.1473, 1996) and found ‘reduced softening’ of the bulk susceptibility beginning at the temperature T^* which is appr. 25 K above the transition ($T_c=138$ K, $T^*=164$ K) and explained it as marking the condensation of polar clusters (Polar Nano Regions first appearance). Here, we observe the appearance of localized modes in the vicinity of the similar temperature, $T^* \sim 160$ K, in a single crystal (nominally) of $KTa_{0.83}Nb_{0.17}O_3$.



These local modes exist also in the condensed phase ($T=130$ K).

Fig.4. $T=130$ K, constant E method. Peaks which we conditionally classify as “local” are pointed at the graphic.

We suppose that the existence of the local soft-mode could be explained (in general) in the frame of Anderson theory of localized states in a random potential.

Domain Dynamics and Coercive Field in BaTiO₃ Ultrathin Capacitors

J. Y. Jo¹, D. J. Kim¹, Y. S. Kim¹, T. K. Song², J.-G. Yoon³, T. W. Noh¹

¹*FPRD&ReCOE, Department of Physics, Seoul Nat'l Univ., Korea*

²*School of Nano & Advanced Materials Engineering, Changwon Nat'l Univ., Korea*

³*Department of Physics, Univ. of Suwon, Korea*

Phone:+82-2-883-1385; Fax:+82-2-875-1222; e-mail: jyjo@phy.snu.ac.kr

Under an electric field, a polarization of a ferroelectric material can be switched. Coercive field (E_C), which is an electric field enough to switch a polarization, has attracted technological interests as well as scientific issue. Especially, thickness-dependence of E_C has believed to provide physical understandings on polarization switching. At the same time, thickness-dependence of E_C can give a guideline for determining the device size to obtain information on operating voltage of high density ferroelectric memory device. In this talk, we will show that, in ultrathin BaTiO₃ (BTO) capacitors, the initial domain nucleation stage governs the polarization switching process and thickness dependence of E_C .

We fabricated fully-strained and passive-layer-free SrRuO₃/BTO/SrRuO₃ capacitors, whose BTO thicknesses (d) are between 5 and 30 nm, on SrTiO₃ (001) substrates using laser molecular beam epitaxy [1]. From hysteresis loops of the BTO capacitors, E_C values could be measured. As d decreases, E_C seems to increase initially but becomes almost independent of d . In order to explain this behavior, we used the theory on domain nucleation. Under the condition that half-prolate spheroid nuclei are formed, we found that calculated E_C should be proportional to $d^{-2/3}$. With the literature values of the domain wall energy, 17 mJ/m², and $a(c)$ -axis dielectric constant, 220(80), we found that the domain nucleation theory can explain the experimental values quantitatively. Below 15 nm, the film thickness becomes so thin that cylindrical nuclei should be formed instead of the half-prolate nuclei. Under this condition, we could also explain the d -independent E_C values quantitatively using the same domain nucleation theory [2].

This ferroelectric domain nucleation process should govern the polarization switching process of the ultrathin BTO films, whose domain wall velocity becomes extremely slow. In addition, this could provide an explanation for the strong polarization relaxation of the BTO capacitors, which was reported very recently [3].

[1] Y. S. Kim *et al.*, Appl. Phys. Lett. **86**, 102907 (2005).

[2] J. Y. Jo *et al.*, Appl. Phys. Lett. **89**, 232909 (2006).

[3] J. Y. Jo *et al.*, Phys. Rev. Lett. **97**, 247602 (2006).

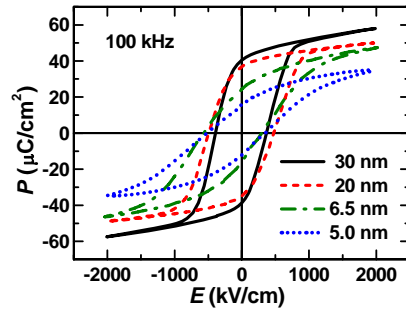


FIG. 1. (Color online) Polarization-electric field (P - E) hysteresis loops of $\text{SrRuO}_3/\text{BaTiO}_3/\text{SrRuO}_3$ capacitors with BaTiO_3 thickness from 30 to 5.0 nm.

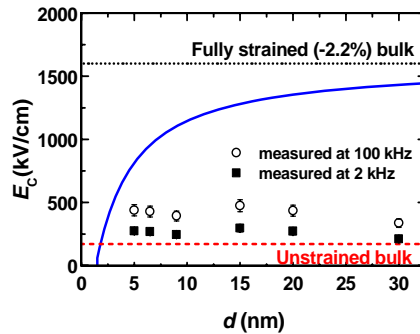


FIG. 2. (Color online) Thickness (d) dependence of coercive fields (E_C) based on homogeneous polarization switching models. Calculated intrinsic E_C of BaTiO_3 capacitors with the Landau-Devonshire theory and measured E_C values (open circles) at 100 kHz and (solid squares) at 2 kHz. The red dashed line and black dotted line are the calculated E_C for unstrained and -2.2% fully strained BaTiO_3 bulk, respectively. The blue solid line is the calculated E_C under -2.2% fully strain and a depolarization field.

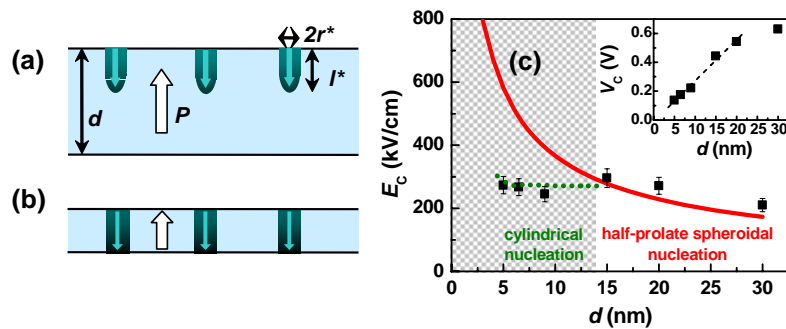


FIG. 3. (Color online) Schematic diagrams of (a) half-prolate spheroidal nucleation and (b) cylindrical nucleation. (c) The d -dependent (solid squares) experimental and calculated E_C based on the half-prolate spheroidal nucleation model (red solid line) and the cylindrical nucleation model (green dotted line). In the shaded region, the d -dependent E_C is thought to be governed by cylindrical nucleation, rather than half-prolate spheroidal nucleation. The inset shows the coercive voltages (V_C) as a function of d . The black dashed line is an eye-guide.

The hunt for a Snark: Direct imaging of Spatial and Energy Distribution of Nucleation Centers in Ferroelectric Materials

Sergei V. Kalinin,^{1,2} Stephen Jesse, Brian J. Rodriguez, and Arthur P. Baddorf
Materials Science and Technology Division and The Center for Nanophase Materials
Sciences, Oak Ridge National Laboratory, Oak Ridge, TN 37831

I. Vrejoiu, D. Hesse, and M. Alexe
Max Plank Institute of Microstructure Physics, 06120 Halle, Germany

Eugene A. Eliseev and Anna N. Morozovska
National Academy of Science of Ukraine, Kiev, Ukraine

The presence of two or more stable polarization states has propelled ferroelectric materials into a spotlight as promising materials for non-volatile random access memories,^{1,2} high-density data storage, and functional oxide heterostructures.³ These applications are ultimately based on writing by electric-field induced polarization switching and subsequent reading of the stable polarization state. Seminal work by Landauer has demonstrated that the experimentally observed switching fields correspond to impossibly large ($\sim 10^3 - 10^5$ kT) values for the nucleation activation energy.⁴ To resolve this discrepancy, referred to as the Landauer paradox, the presence of discrete switching centers initiating low-field nucleation and controlling macroscopic polarization switching is required.⁵ However, despite 50 years of research,^{6,7,8} very little is known about the microscopic origins of the Landauer paradox.

We have used a spectroscopic approach based on atomic force microscopy (AFM) to visualize and probe individual nucleation centers. The probe concentrates an electric field to a nanoscale volume of material (~ 10 nm), as shown in Fig. 1(a), and induces local domain formation. Simultaneously, the probe detects the onset of nucleation and the size of a forming domain via detection of the electromechanical response of the material to a small AC bias after the application of controlled DC bias pulses.⁹ The onset of nucleation corresponds to the point in the electromechanical hysteresis loop where the signal deviates from the remanent value [Fig. 1 (c)]. As in the macroscopic case, the presence of defects is expected to lower the nucleation energy or, equivalently, the bias required for switching. Hence, a map of local nucleation voltages represents the spatial and energy distribution of local switching centers.

Shown in Fig. 1(d) is the nucleation voltage map of an epitaxial lead zirconate-titanate thin film. The dark spots on the image correspond to local nucleation centers, and corresponding bias provides the information on local activation barrier on switching. From the estimate of activation energy of ~ 1 eV, the nucleating domain radius is $\sim 1-2$ nm, well below spatial resolution of contact mode AFM. From Fig. 1 (d), the spatial distribution of the switching centers can be obtained. The analysis of both positive and negative nucleation bias maps allows extracting the components of thermal (variation in depolarization energy of domain wall energy) and field (built-in polarization) disorder independently.

To summarize, we have demonstrated an approach for real-space imaging of microscopic switching behavior in ferroelectrics including spatial and energy distribution of

¹ Corresponding author, sergei2@ornl.gov

² Also affiliated with Department of Materials Science and Engineering, North Carolina State University, and Department of Materials Science and Engineering, University of Tennessee, Knoxville

nucleation centers. The fact that area density of dislocations in these films is close to the density of observed defects provides strong evidence that dislocations can be preferred nucleation sites. Further work will reveal the role of dislocation type and establish atomistic mechanisms for domain nucleation.

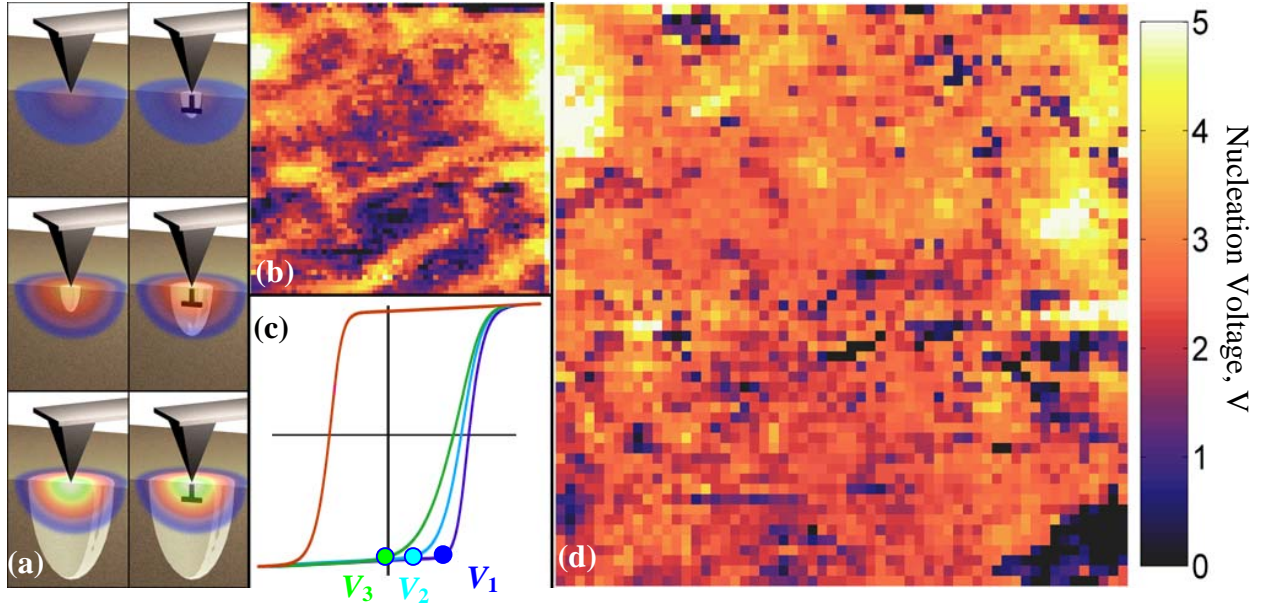


Fig. 1. (a) Domain formation (white parabolic) in the field (blue) of a PFM tip on an ideal surface (left) and in the presence of a nucleation center (right) for three different voltages ($V_{\text{top}} < V_{\text{middle}} < V_{\text{bottom}}$). The presence of the defect lowers the critical bias required for domain nucleation. Without the defect, the new domain nucleates at V_{middle} , whereas with the defect, it nucleates at V_{top} . (b) point-by-point PFM image of the PZT film. (c) Schematics of hysteresis loops which demonstrate the variability in nucleation voltages. (d) 2D map of nucleation biases from the same region as (b). Dark regions (indicated with white ovals) correspond to nucleation centers. (b) and (d) are 60 x 60 pixel (16 nm spacing) images corresponding to a 960 x 960 nm² area.

Research supported by the U.S. Department of Energy Office of Basic Energy Sciences Division of Materials Sciences and Engineering at Oak Ridge National Laboratory operated by UT-Battelle, LLC.

References

- ¹ J. Scott, *Ferroelectric Memories* (Springer Verlag, Berlin, 2000).
- ² Rainer Waser (Ed.), *Nanoelectronics and Information Technology*, Wiley-VCH (2003)
- ³ T. Tybell, P. Paruch, T. Giamarchi, and J.-M. Triscone, *Phys. Rev. Lett.* **89**, 097601 (2002).
- ⁴ R. Landauer, *J. Appl. Phys.* **28**, 227 (1957).
- ⁵ J.F. Scott, *J. Phys. Condens. Matter* **18**, R361 (2006).
- ⁶ A.M. Bratkovsky and A.P. Levanyuk, *Phys. Rev. Lett.* **85**, 4614 (2000).
- ⁷ M. Molotskii, R. Kris, and G. Rosenman, *J. Appl. Phys.* **88**, 5318 (2002).
- ⁸ G. Gerra, A.K. Tagantsev, and N. Setter, *Phys. Rev. Lett.* **94**, 107602 (2005).
- ⁹ S. Jesse, H.N. Lee, and S.V. Kalinin, *Rev. Sci. Instr.* **77**, 073702 (2006).

Locally Probed Ferroelectricity of Nanomesas Formed from Polymer Langmuir-Blodgett Thin films

Jihee Kim¹, Stephen Ducharme¹, Brian Rodriguez², Stephen Jesse², Sergei V. Kalinin²

¹Department of Physics and Astronomy, Nebraska Center for Materials and
Nanosturctures, Univerty of Nebraska, Lincoln, NE 68588-0111, USA

²Materials Science and Technology Division, Oak Ridge National Laboratory, Oak Ridge,
TN 37831, USA

Phone: 402-472-2694; Fax: 402-472-2879; e-mail: jhkim@unlserve.unl.edu,
sducharme1@unl.edu

Nanomesas are self assembled ferroelectric crystals formed from Langmuir-Blodgett (LB) films of copolymers of polyvinylidene fluoride with trifluoroethylene (P(VDF-TrFE)) through annealing.^{1,2} Nanomesas are disk-shaped with approximately 9 nm in thickness and 100 nm in diameter.^{1,2} The crystallinity of nanomesas has been probed by x-ray diffraction and their ferroelectricity also has been shown by various measurements. The ferroelectric to paraelectric phase transition has been measured by temperature-dependent X-ray diffraction¹ and macroscopic dielectric ‘butterfly’ hysteresis curves and pyroelectric hystersis loops also have been observed from nanomesas.²

Following the previous studies, one of our goals in nanomesa studies has been to probe the ferroelectric properties of individual nanomesas. Piezoresponse force microscopy (PFM) and switching spectroscopy PFM (SSPFM) are excellent tools for the purpose. Our recent study on P(VDF-TrFE) LB thin films with PFM revealed that the imaging resolution is below 5 nm, and well-behaved local polarization switching was also observed by obtaining piezoelectric hysteresis loops from regions of the film averaging 25-50 nm in size with SSPFM.³

Here we report the preliminary results of local electromechanical characterization of nanomesas using PFM and SSPFM. Poling nanomesas over an area 600 nm square was successfully executed by applying a DC bias of ± 3.5 V to the PFM tip during scanning [Figure 1]. Polarization switching loops were obtained by SSPFM over a region of 30 nm square [Figure 2]. Some amount of modification of mesas morphology during scanning is, however, inevitable since the morphology of nanomesas itself introduces a rough, compliant surface to the probing tip. Despite the fact that we need to improve scanning condition to reduce the modification of the nanomesas, this study showed promising results that the probing one individual nanomesa is possible.

References

1. Mengjun Bai, Matt poulsen, Stephen Ducharme “Effects of annealing conditions on ferroelectric nanomesa self-assembly” *JPCM* **18** 7383-7392 (2006)

2. Mengjun Bai, Stephen Ducharme, “Ferroelectric nanomesa formation from polymer Langmuir-Blodgett films” *APL* **85**, 3528-3530 (2004)

3. Brian J. Rodriguez, Stephen Jesse, Sergei V. Kalinin, Jihee Kim, Stephen Ducharme, “Nanoscale polarization manipulation and imaging in ferroelectric Langmuir-Blodgett polymer films”, submitted to *Appl. Phys. Lett.*

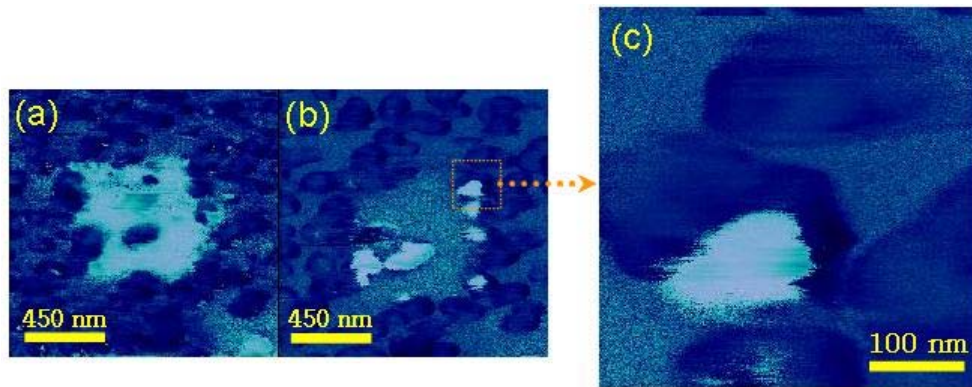


Figure 1. PFM phase images of nanomesas. (a): An area of 600 nm square was firstly poled with +3.5 DC voltage, then an image of a larger area of 1.5 μm square was taken. (b): The same procedure shown in the image (a) was repeated with -3.5 DC voltage on the same spot. (c): After (a) and (b) the tip was relocated as indicated with a box in the image (b), then the image of an area of 392 nm square was taken.

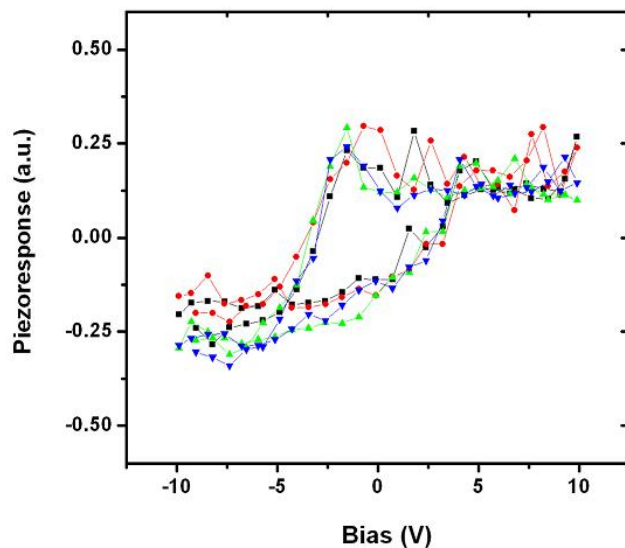


Figure 2. Well-behaved Piezoelectric hysteresis loops obtained from four different spots within an area of 30 nm square of a nanomesa sample with SSPFM. The time for each loop was 2.5 seconds.

Observation of room temperature ferroelectricity in strained SrTiO₃ thin films on SrTiO₃ substrate

Y. S. Kim¹, D. J. Kim¹, J. S. Choi², T. H. Kim¹, J. Y. Jo¹, B. H. Bark², J.-G. Yoon³, T. W. Noh¹

¹*ReCOE & FPRD, Department of Physics and Astronomy, Seoul National University, Seoul 151-747, Korea*

²*Department of Physics, Konkuk University, Seoul 143-701, Korea*

³*Department of Physics, University of Suwon, Gyung-gi do 445-743, Korea*

Phone: 82-2-883-1385; Fax: 82-2-875-1222; E-mail: ysukim@phya.snu.ac.kr

SrTiO₃ (STO) is known well as incipient ferroelectric (FE) material: competing interactions, such as FE in stability, quantum fluctuation, and/or the antiferrodistortive, interrupt the FE transition down to 0K. Such competing interactions could be overcome by applying additional degrees of freedom. For examples, enhancement of the Curie temperature can be achieved by doping with other atoms, isotopic substitution in the oxygen octahedra, and applying external electric fields or strain. There have been numerous works which reported appearance of ferroelectricity in STO. However, in most previous works, the direct evidences of the spontaneous polarization have been rare. Instead, anomalies of dielectric constant, the second harmonic generation, or changes in the lattice constants were presented as evidences of ferroelectricity. In addition, the reported values of the Curie temperature enhancement were not so large. As far as we know, there has been one report which showed the FE *P-V* loops at temperature higher than 70K on single crystal-like STO on DyScO₃ (101) substrate.^[1, 2]

In this presentation, we will report the room temperature FE properties of epitaxial STO films, which were deposited between SrRuO₃ top and bottom electrodes on STO (001) substrate. From reciprocal space mapping, we could observe enhancement of unit cell volume of our STO films, probably due to oxygen vacancies. Therefore, the STO films have tetragonal structure even on STO substrates. As shown in Fig. 1, the c-axis lattice constant shows strong dependence on deposition oxygen partial pressure. Figure 2 displays temperature dependent *P-V* loops, which show that remnant polarization increases with decrease of temperature and has a non-zero value even at room temperature. Up to our best knowledge, this is the first room temperature observation of *P-V* loops in compressive strained STO films. Stability of ferroelectric domains was also investigated by piezoresponse force microscopy as a function of domain retention time, as shown in Fig. 3. When the film was poled downward, the down polarization disappears rather fast with time. On the other hand, up polarization shows very slow decay in time. According to a thermodynamic calculation,^[3] the misfit strain of our STO films is not large enough to raise their Curie temperature up to room temperature. Therefore, we cannot explain the observed FE behavior at room temperature simply in terms of biaxial strain. We will discuss possible origins and other intriguing aspects of these phenomena.

- [1] J.H. Haeni *et al. Nature*. **430**, 758 (2004).
 [2] M.D. Biegalski *et al. Appl. Phys. Lett* **88**, 192907 (2006)
 [3] Pertsev *et al. Phys. Rev. B* **61**, R825–R829 (2000).

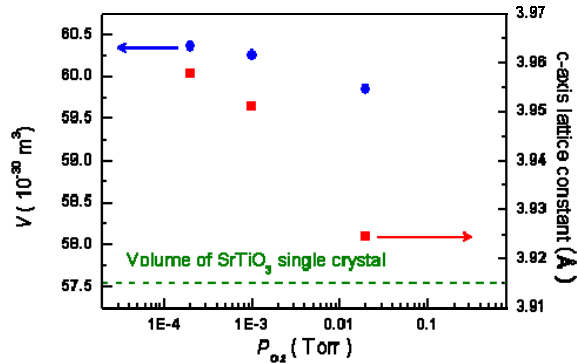


Figure 1 Unit cell volume and the c-axis lattice constant of SrTiO₃ films as a function of deposition oxygen partial pressure. (P_{O_2}) The films were grown with the capacitor configuration of SrRuO₃/SrTiO₃/SrRuO₃ on SrTiO₃ (001) substrates

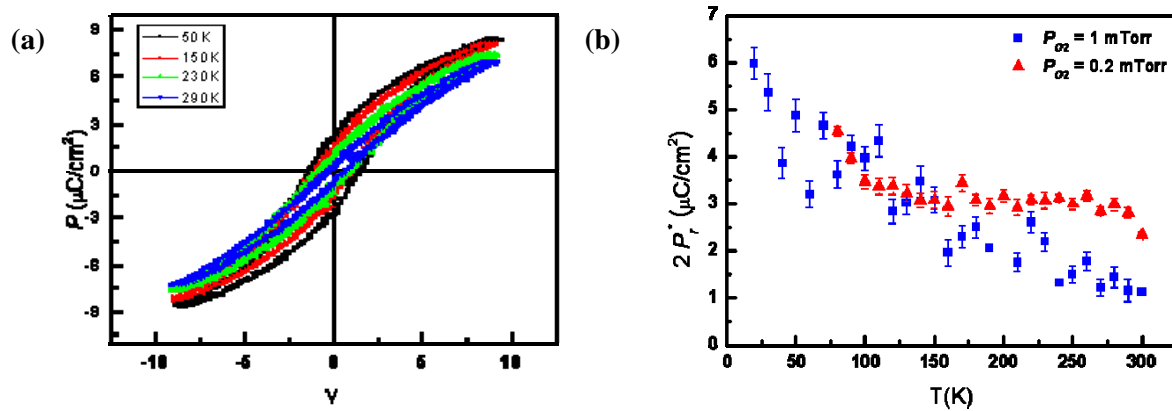


Figure 2 (a) Temperature dependent P - V hysteresis loops of the SrTiO₃ films. Deposition oxygen partial pressure (P_{O_2}) was 1×10^{-3} Torr. (b) Temperature dependence of remnant polarization for the SrTiO₃ films deposited at 1×10^{-3} Torr (blue squares) and 2×10^{-4} Torr (red triangles).

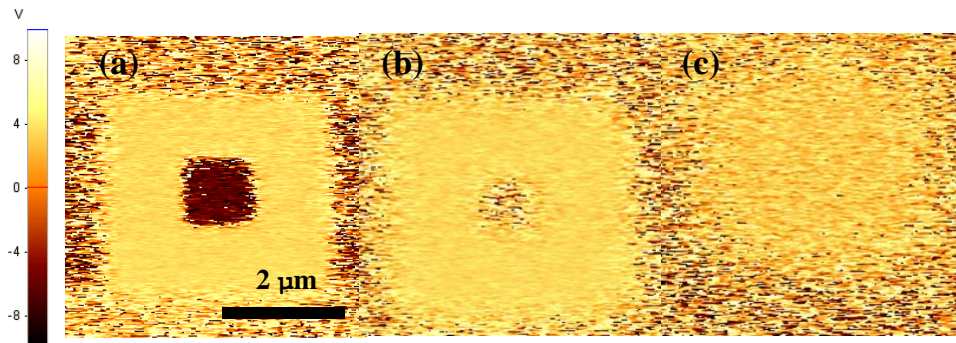


Figure 3 Piezoresponse force microscopy (PFM) images for the SrTiO₃ film. Initially, the inner 3 and 1 μm^2 regions were applied with +10.5 and -10.5 V bias, respectively. PFM images were taken after around (a) 7 minutes, (b) 2 hours, and (c) 17 hours.

On the Lattice Representation of Joint Hamiltonian and Stochastic Dynamics for Field Induced Polarization Switching

Eriks Klotins

Institute of Solid State Physics, University of Latvia

Phone: +371 7187866; Fax: +371 7132778; e-mail: klotins@cfi.lu.lv

This study is focused on nonequilibrium Landau-type polarization and strain response [1], inextricably mixed with the stochastic behavior as emerged from the system - bath coupling [2]. The subject of special interest is the dynamics of polarization response formally introduced by Fokker-Planck equation for model Hamiltonian and (in this study) reformulated in the lattice representation, namely, each site of a cubic lattice is assigned to an anharmonic oscillator obeying Ginzburg-Landau dynamics and affected by thermal noise and mean-field interaction with its first neighbors. In spite of simplicity and the canonical axiomatic level, the lattice representation displays essential features of polarization response as well as the impact of electric and elastic boundary conditions associated with model Hamiltonians of arbitrary complexity. The technicalities comprise Wentzel-Kramer-Brillouin (WKB) mapping to imaginary time Schrödinger equation and its subsequent symplectic integration [3]. This approach (valid for microscopically large and macroscopically small lattice spacing) starts with Hamiltonian \mathbf{H} structured in local polarization f_p , elastic f_{el} , electroelastic f_c , and gradient f_g terms, and polarization \mathbf{P} , strain u_{ij} and electric field \mathbf{E} as key entities

$$H(\mathbf{P}, u_{ij}) = \int d\mathbf{r} (f_p(\mathbf{P}) + f_{el}(u_{ij}) + f_c(\mathbf{P}, u_{ij}) + f_g(P_{i,j}P_{k,l}) - \mathbf{P} \cdot \mathbf{E}) \quad (1)$$

The lattice representation emerges at replacing the integral by a sum over i, j, k lattice sites and WKB mapping for the relevant Fokker-Planck relation. The time evolution of polarization obeys the mean-field imaginary time Schrödinger equation for auxiliary function $G(\mathbf{P}_{ijk})$

$$\frac{\partial G(\mathbf{P}_{ijk})}{\partial t} = \left[\Xi \left(\frac{\partial^2}{\partial P_1^2} + \frac{\partial^2}{\partial P_2^2} + \frac{\partial^2}{\partial P_3^2} \right) + V \right] G(\mathbf{P}_{ijk}) \quad (2)$$

In Eq.(2) the diffusion term accounts for thermal fluctuations whereas the second one V comprises local polarization $\mathbf{P}_{i,j,k}$, the first moments of probability distribution in adjacent sites $\bar{\mathbf{P}}_{i\pm 1,j,k}, \bar{\mathbf{P}}_{i,j\pm 1,k}, \bar{\mathbf{P}}_{i,j,k\pm 1}$, the lattice spacing, kinetic coefficient emerged by system - bath coupling, and the impact of electroelastic interactions as generated by elastostatic Greens functions [4]. Selfconsistent solution of this (nonlocal and boundary) problem is found by symplectic integration of Eqs.(2) for all lattice sites [3]. New results concern (i) field induced polarization switching and (ii) nucleation and sideway growth of domains in uniaxial lattice models.

Figure 1 shows a finite 1D lattice of 120 lattice sites which initially polarization pattern found as a result of self consistent stationary solution of a set of Fokker-Planck equations with zero boundary conditions (plot 1). Time development of these 180° domains under monotonously growing external field (plot 2) demonstrates side growth

(motion of domain walls) and the birth of opposite domains at boundaries. Monodomain state (plot 3) arrives at external field being substantially lower than the thermodynamic switching field, as expected.

Figure 2 shows snapshots of temperature controlled nucleation and sideway growth of a domain actually located at lattice site # 110 of 240 with 10^{-8} m spatial increment. Material constants are taken for PbTiO_3 (with 479°C transition temperature) [5]. Nucleation is triggered by ergodicity breaking defect (specified by $0.5 \cdot 10^6$ V/m electric field). The left shifted snapshot shows polarization at 493.1°C as restricted within a single lattice site. At reducing the temperature down to 471.3°C coarsening over about ten lattice sites (middle plot) appears. Further decreasing of the temperature down to 470.9°C reproduces the sideway growth reaching 50 lattice sites (right snapshot) in accord with the concept [6]. Estimate of the lattice spacing is 10^{-8} m.

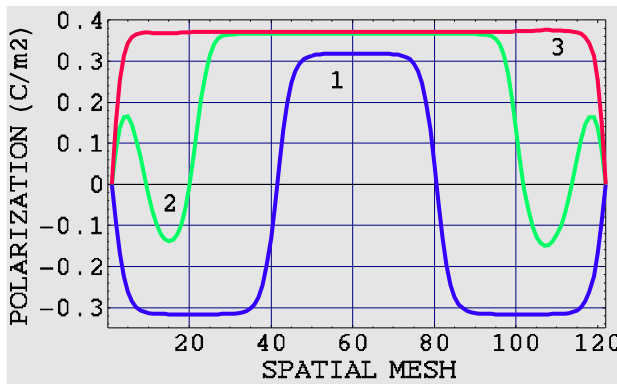


Fig.1 Subsequent snapshots of three 180° domains (1) switched under external field. Plot (2) exposes sideway growth of the positive domain and the birth of opposite domains at boundaries. Monodomain state (3) arrives at field substantially lower than the thermodynamic one. Material constants are from [5] for PbTiO_3 thin film at temperature 100°C .

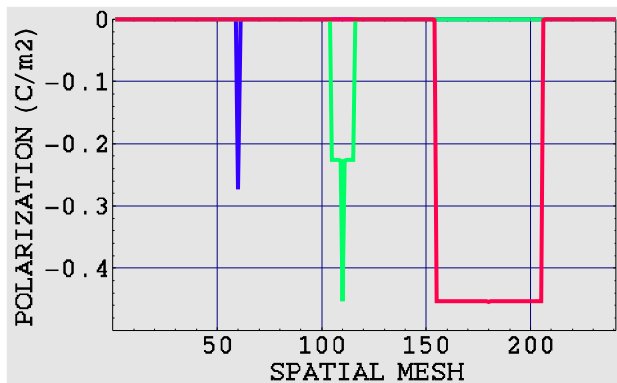


Fig.2 Temperature controlled nucleation and sideway growth of a single domain. The left snapshot resembles to local polarization triggered by ergodicity breaking defect located at lattice site # 110 of 240. As the temperature decreases the coarsening (middle snapshot) and sideway growth (right snapshot) appear in accord with [6].

Insight in the survey of lattice representation and symplectic integration including electro-elastic interactions is given in [7].

References

- [1] S. Nambu, A. Sagala, Phys. Rev. B, 50, 5838 (1994).
- [2] M. Shiino, Phys. Rev. A 36, 2393 (1987).
- [3] E. Klotins, Eur. Phys. J. B 50, 315-320 (2006).
- [4] J. Hlinka, E. Klotins, J. Phys.: Condens. Matter 15, 5755-5764 (2003).
- [5] Y.L. Li, S.Y. Hu, Z.K. Liu, L.Q. Chen, Acta Materialia 50 (2002) 395-411.
- [6] M. Dawber, K. M. Rabe, J. F. Scott, Rev. Mod. Phys, Vol 77, (2005).
- [7] <http://home.lanet.lv/~klotins/>

Clarified Ferroelectric Transition of BaTiO₃ Single Crystal

Akira Kojima¹, Yukio Yoshimura², Ken-ichi Tozaki³

¹ The University of Shiga Prefecture, Hikone, Shiga 522-8533, Japan

² Ritsumeikan University, Kusatsu, Shiga 525-8577, Japan

³ Chiba University, Inage, Chiba 263-8522

Phone: +81-749-28-8367; Fax: +81-749-28-8589; e-mail:kojima@mat.usp.ac.jp

It is the best method for the deep understanding of structure and mechanism of ferroelectrics to observe directly the precise transient process from paraelectric to ferroelectric phases but it has never succeeded until today due to the technical difficulty of slow cooling. We have recently established a technique of simultaneous measurements of physical properties during the phase transition even on cooling with nearly quasi-static change, using the “MKS cell” [1]. BaTiO₃ phase transition at 402 K is not reversible: ferroelectric transition on cooling reveals the two-step nature. Figures 1 and 2 show the results of the simultaneous measurement of heat flux with the dielectric constant and the displacement current along the three crystallographic axes. The single crystal was served by MTI Corporation and its sample quality is excellent: it would be called photoreflective grade if it were poled. It was cut along the crystallographic axes and etched by phosphoric acid to remove strain caused by cutting. The so-called 90° domain pattern is seen even by the naked eyes as shown in Fig. 3. The results in Figs. 1 and 2 mean that the transition accompanies two thermal anomalies and the first anomaly is estimated to be the exothermic heat due to the tetragonal change by the result of the dielectric constant. It is to be noted that few displacement current flows at the first anomaly, which shows negative evidence of the so-called Ti displacement in the unit cell.

Stimulated by the remarkable finding two-step nature, structure study of the single crystal has been made using x-ray precession method necessary for very exact and fundamental work. Figure 4 shows x-ray precession photograph of the b*-plane. Extra spots indicated by arrows are observed near main Bragg spots but they are not observed on the a*- and c*-planes. They are not on a rectangular net but on a parallelepiped net as shown in Fig. 5 and the main and the extra spots are completely superposed on rectangular nets in the a*- and c*-planes, which means existence of a monoclinic structure except a tetragonal. As a conclusion, BaTiO₃ has the coherent hybrid structure composed of the tetragonal and monoclinic forms having the (101) tetragonal face in common as shown in Fig. 6 [2, 3]. The oblique common face is thought to be the domain wall splitting the two kinds of clusters composed of different structures. It may be reasonable that interstitially different domain color is caused by different photo absorption due to different structures. Comparing the structure model with the outlook of the cubed single crystal in Fig. 3, the crystal axes of the sample are fixed so that each data is denoted as in Figs. 1 and 2. Large displacement current flows along the b-axis at the second thermal anomaly, which is thought to be caused by the electric flux change due to the formation of the monoclinic cluster along the b-axis inside the tetragonal crystal, making the domains. Opposite ends of the cubed crystal along the b-axis

will have some pyro-charge if the electric circuit for the measurement is opened. If enough time is allotted at the oral session, the unit cell evolution of BaTiO₃ and its site-disordered structure model of the four phases will also be talked.

[1] A. Kojima *et al*, Rev. Sic. Instrum. **68**, 2301 (1997).

[2] Y. Yoshimura *et al*, Phys. Lett. A, **353**, 250 (2006).

[3] C. Kittel, "Your results are convincing." (reply to sending a reprint of the paper [2]).

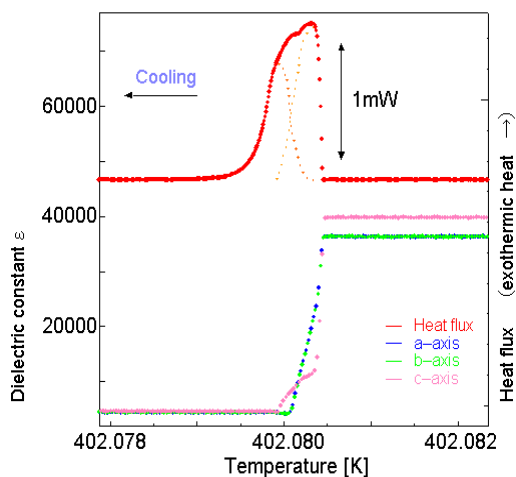


Fig. 1. Heat flux and the dielectric constant.

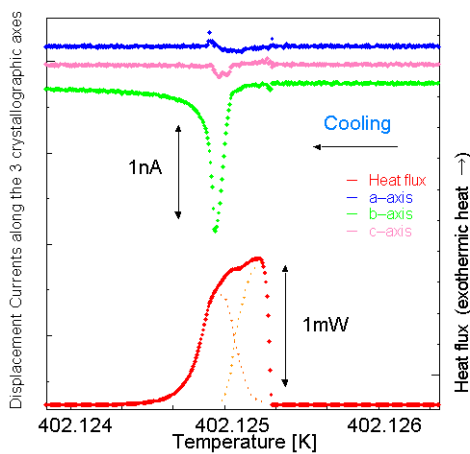


Fig. 2. Heat flux and the displacement current.

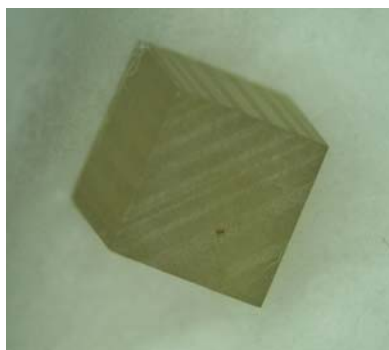


Fig. 3. Outlook of a cubed sample.

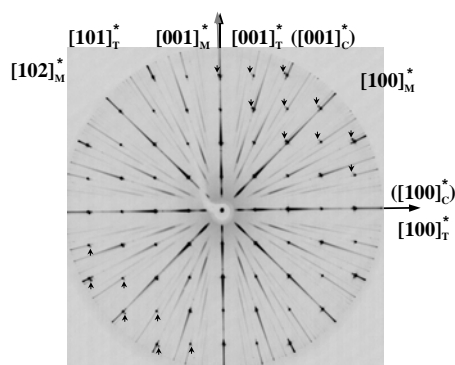


Fig. 4. X-ray precession photo of the b*-plane.

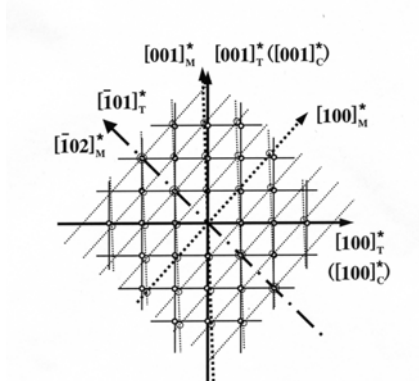


Fig. 5. Schematic illustration of reciprocal nets.

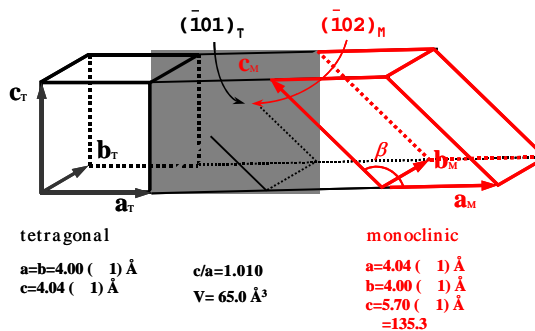


Fig. 6. Hybrid structure model of the ferroelectric phase.

Phase diagram of $\text{Pb}(\text{Zr},\text{Ti})\text{O}_3$ solid solutions from first principles

Igor A. Kornev* and Laurent Bellaïche

Physics Department, University of Arkansas, Fayetteville, Arkansas 72701, USA

P.-E. Janolin and B. Dkhil

*Laboratoire Structures, Propriétés et Modélisation des Solides,
CNRS-UMR8580, Ecole Centrale Paris, 92290 Châtenay-Malabry, France*

E. Suard

*Institut Laue-Langevin, 6 rue Jules Horowitz,
BP 156 38042, Grenoble Cedex, France*

A first-principles-derived scheme, that incorporates ferroelectric (FE) and antiferrodistortive (AFD) degrees of freedom, is developed to study finite-temperature properties of $\text{Pb}(\text{Zr}_{1-x}\text{Ti}_x)\text{O}_3$ (PZT) solid solutions near its morphotropic phase boundary (MPB) [1]. The use of this numerical technique (i) resolves controversies about the monoclinic ground-state for some Ti compositions, (ii) leads to the discovery of an overlooked phase, and (iii) yields three multiphase points, that are each associated with four phases.

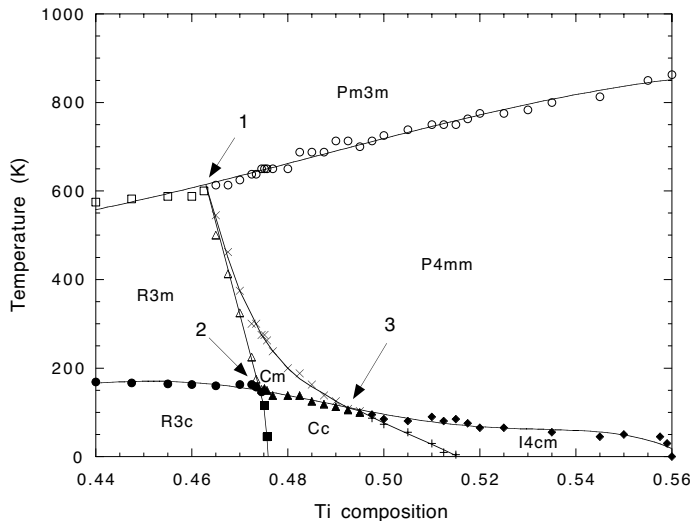


FIG. 1: Phase diagram of PZT near its MPB, as predicted by the present scheme with an applied pressure of -4.68GPa . Symbols display the results of our simulations, while lines are guide for the eyes. Indices 1, 2 and 3 indicate the multiphase points. The uncertainty on the transition temperatures is typically around 13 K, except close to the multiphase points 2 and 3 for which this uncertainty is around 3 K.

the findings of Refs. [4, 5] that the correct space group for the low-temperature phase of $\text{Pb}(\text{Zr}_{0.52}\text{Ti}_{0.48})\text{O}_3$ is Cc rather than Pc , as initially proposed in Ref. [6]. Moreover, the oxygen octahedra in this Cc phase do *neither* rotate about the $[001]$ direction (as thought in

Figure 1 reports the phase diagram of $\text{Pb}(\text{Zr}_{1-x}\text{Ti}_x)\text{O}_3$ near the MPB, as predicted by the present scheme with a -4.68GPa pressure. Seven phases exist within a narrow compositional range. Five of such phases are well-known, namely paraelectric $Pm\bar{3}m$, FE rhombohedral $R3m$, FE tetragonal $P4mm$, FE monoclinic Cm , and the rhombohedral $R3c$ state in which ferroelectricity coexists with AFD motions. The sixth phase is the previously “controversial” Cc phase, and that is the ground-state at intermediate Ti compositions. The monoclinic phases are predicted to exist for the narrow Ti compositional range of 46.3 %–51.5%, which agrees remarkably well with the experimental range of $\simeq 46\%-52\%$ [2, 3]. Furthermore, we confirm

*Also at Novgorod State University, Russia; Electronic address: ikornev@uark.edu

Ref. [6]) nor about the [111] direction (as proposed in Ref. [5]) but rather about an axis that is in-between the [001] and [111] directions (which is in agreement with Ref. [4]). Interestingly, this axis of rotation does *not* precisely coincide with the direction of the polarization which contrasts with the assumption of Ref. [4].

The last phase occurs at small temperature and for the largest displayed Ti compositions, and has never been suggested to be a possible ground-state of PZT (to the best of our knowledge). This phase has a $I4cm$ space group, also involves a coexistence of ferroelectricity and rotation of oxygen octahedra, but is associated with the *tetragonal* symmetry (unlike $R3c$ and Cc). As a result, an increase in Ti concentration from $\simeq 47\%$ to 52% results not only in a spontaneous polarization continuously rotating from [111] to [001] but also to the oxygen octahedra varying their rotation axis from [111] to [001] – via the $[uvw]$ directions in the bridging monoclinic structures Cm and Cc phases.

Other features of Fig. 1 going against common beliefs [4, 5] are the *non-verticality* of the temperature-composition boundary lines separating rhombohedral from monoclinic structures. As a result, *five* different phases emerge for some narrow compositions. For instance, for $x \simeq 47.2\%$, our scheme predicts the $Pm\bar{3}m$, $P4mm$, Cm , $R3m$ and $R3c$ phases when decreasing the temperature. Similarly, a Ti concentration around 47.5% yields a $Pm\bar{3}m - P4mm - Cm - Cc - R3c$ sequence. Finally, Fig. 1 further reveals the existence of three temperature-compositional points, for which *four* phases are very close to each other! The first multiphase point gathers the paraelectric $Pm\bar{3}m$ state and the FE $R3m$, Cm and $P4mm$ phases, and occurs for $T \simeq 610$ K and $x \simeq 46.3\%$. Two purely FE phases meet with two phases exhibiting a coexistence of FE and AFD motions for the other two multiphase points. More precisely, $R3m$, Cm , $R3c$ and Cc all meet at $T \simeq 150$ K and $x \simeq 47.4\%$, while Cm , $P4mm$, Cc and $I4cm$ overlap at $T \simeq 100$ K and $x \simeq 0.495$.

Additional neutron diffraction measurements strongly support some of these predictions. In particular, a Rietveld analysis of neutron data on a $Pb(Zr_{0.49}Ti_{0.51})O_3$ sample confirms the existence of the presently-discovered $I4cm$ structure.

This work is supported by ONR grants N00014-04-1-0413, N00014-01-1-0600 and N00014-01-1-0365, by NSF grant DMR-0404335, and by DOE grant DE-FG02-05ER46188. We thank B. Noheda for useful discussions.

-
- [1] Igor A. Kornev, L. Bellaiche, P.-E. Janolin, B. Dkhil, and E. Suard, *Phys. Rev. Lett.* **97**, 157601 (2006).
 - [2] B. Noheda *et al*, *Phys. Rev. B* **61**, 8687 (2000).
 - [3] K. C. Lima *et al*, *Phys. Rev. B* **63**, 184105 (2001).
 - [4] D.J. Woodward, J. Knudsen and I.M. Reaney, *Phys. Rev. B* **72**, 104110 (2005).
 - [5] B. Noheda, L. Wu, and Y. Zhu, *Phys. Rev. B* **66**, 060103(R) (2002).
 - [6] R. Ranjan, Ragini, S.K. Mishra, D. Pandey and B.J. Kennedy, *Phys. Rev. B* **65**, 060102(R) (2002).

Born-Oppenheimer energy landscapes away from equilibrium: bond breaking and transition states by auxiliary-field quantum Monte Carlo

Henry Krakauer, W. A. Al-Saidi, Shiwei Zhang, and W. Purwanto
Department of Physics, College of William and Mary, Williamsburg, VA 23187-8795.
Phone: 757-221-3520; Fax: 757-221-3540; e-mail: hkrak@wm.edu

Born-Oppenheimer energy landscapes away from equilibrium provide a challenging testbed for all approximate many-body computational methods, since they can mimic different levels of electron correlation. Examples include bond stretching, breaking, and transition states. We report calculations using the recently developed phaseless auxiliary-field quantum Monte Carlo (AF QMC) method [1] on several such systems. To control the sign/phase problem, the phaseless AF QMC method constrains the random walks in Slater determinant space with an approximate phase condition that depends on a trial wave function. With single-determinant unrestricted Hartree-Fock (UHF) trial wave functions, the phaseless AF QMC method yields total energies at equilibrium geometries with typical systematic errors of no more than a few mHa compared to exact results [2]. As bonds are stretched, the method generally gives better overall accuracy and a more uniform behavior than the coupled cluster CCSD(T) method in mapping the potential-energy curve. The use of multiple-determinant trial wave functions from multi-conjugation self-consistent-field (MCSCF) calculations is also explored. The increase in computational cost versus the gains in statistical and systematic accuracy is described. With such trial wave functions, excellent results are obtained across the entire region between equilibrium and the dissociation limit in molecules.

Potential-energy curves of several well-known molecules, including BH, N₂, and F₂ are studied. Figure 1 shows results for the N₂ molecule with a Gaussian basis set computed by AF QMC and state-of-the-art quantum chemistry methods. We have also calculated the transition state of H+H₂ both near the transition state and in the van der Waals limit. Table I shows results for the symmetric collinear H₃ transition state. The AF QMC energies are in excellent agreement with the full conjugation interaction (FCI) energies, which are the exact ground state energies of the system within the defined Hilbert space. The corresponding AF QMC barrier of 0.434(3) eV is in good agreement with the experimental value of 0.421 eV.

TABLE I: Symmetric collinear H₃ transition state total energies using the aug-cc-pVTZ Gaussian basis set [4]. We examined 5 conjugations with $R_1 = R_2 = R$, and we report the unrestricted Hartree-Fock (UHF), full conjugation interaction (FCI), and AF QMC total energies. Bondlengths are in bohr and energies are in Ha. Statistical errors are on the last digit and are shown in parenthesis.

R	UHF	FCI	AF QMC
1.600	-1.599 843	-1.652 219	-1.651 78(7)
1.700	-1.604 162	-1.656 405	-1.655 86(7)
1.757	-1.604 835	-1.657 013	-1.656 52(7)
1.800	-1.604 638	-1.656 770	-1.656 24(8)
1.900	-1.602 269	-1.654 285	-1.653 68(9)

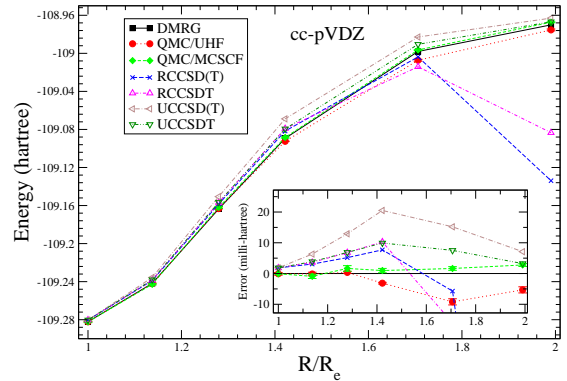


FIG. 1: The potential-energy curve of N₂ with a cc-pVDZ a basis set. We show several coupled-cluster and QMC curves. QMC/UHF energies are obtained using the UHF trial wave function, and QMC/MCSCF are obtained using a multi-determinant trial wave function from MCSCF calculation. We show also the near-exact result obtained using DMRG from Ref. [3], and the inset shows the deviations in mHa of the various methods from the DMRG potential-energy curve.

Finally, we report on a study of bond stretching in a linear chain of hydrogen atoms, H₅₀, within a minimal STO-6G basis set with 50 electrons and 50 orbitals. This system was recently benchmarked using the density-matrix renormalization group (DMRG) method, which was shown to give near-FCI quality energies [5]. As the bond length is stretched, H₅₀ shows typical signatures of a metal-insulator transition, and is a challenging case for correlated methods. Following Ref. [5], we considered both symmetric and asymmetric bond stretching. In the first case, the spacing between H atoms is increased from R=1.0 bohr to R=1.2, 1.4, . . . , 4.2 bohr. The natural structure consists of 50 equidistant, nearly-independent H-atoms on a line. In the case of asymmetric bond stretching, we consider 25 equivalent H₂ molecules with a bondlength of 1.4 bohr, where adjacent hydrogen atoms belonging to two different H₂ molecules are separated by distances of R= 1.4,

TABLE II: Symmetric and asymmetric bond stretching in H_{50} using a minimal STO-6G basis set. We show RHF, UHF, CCSD(T), DMRG, and QMC energies. DMRG and CCSD(T) values are from Ref. [5]. Bondlengths are in bohr and energies are in Ha. Statistical errors are on the last digit and are shown in parentheses.

R	RHF	UHF	CCSD(T)	DMRG	AFQMC
Symmetric					
1.0	-16.864 88	-16.864 88	-17.282 27	-17.284 07	-17.285 2(1)
1.2	-22.461 27	-22.468 05	-22.944 57	-22.947 65	-22.947 5(7)
1.4	-25.029 76	-25.058 91	-25.589 12	-25.593 78	-25.593 3(3)
1.6	-26.062 25	-26.130 19	-26.713 14	-26.719 44	-26.718 8(5)
1.8	-26.265 98	-26.396 69	-27.031 45	-27.038 65	-27.038 8(3)
2.0	-26.008 20	-26.237 77	-26.920 90	-26.926 09	-26.925 6(9)
2.4	-24.835 76	-25.434 02		-26.160 57	-26.159 4(5)
2.8	-23.360 81	-24.634 19		-25.274 80	-25.276 5(7)
3.2	-21.896 33	-24.108 60		-24.568 28	-24.573 3(5)
3.6	-20.574 29	-23.823 26		-24.102 77	-24.108 4(7)
4.2	-18.955 95	-23.634 41		-23.749 71	-23.748 9(4)
Asymmetric					
1.6	-25.963 71		-26.486 01	-26.487 38	-26.486 7(7)
1.8	-26.617 68		-27.126 41	-27.127 16	-27.126 4(9)
2.0	-27.071 82		-27.576 79	-27.577 32	-27.576 9(3)
2.4	-27.609 24		-28.117 27	-28.117 61	-28.116 3(7)
2.8	-27.873 62		-28.386 84	-28.387 07	-28.384 2(5)
3.2	-28.004 68		-28.521 10	-28.521 24	-28.518 9(7)
3.6	-28.069 65		-28.587 28	-28.587 36	-28.584 4(5)
4.2	-28.111 00		-28.628 54	-28.628 58	-28.626 5(5)

1.6, ..., 4.2 bohr. Thus, the final structure consists of 25 equidistant, nearly-independent H_2 molecules at the equilibrium bondlength on a line.

In Table II, we show the results for the symmetric and asymmetric bond stretching, respectively. We show both RHF and UHF energies, as well as our QMC results obtained using the UHF trial wave function, unless a distinct UHF solution could not be found (as in the case of asymmetric bond stretching). For reference, we show the CCSD(T) and DMRG energies as reported in Ref. [5]. In the case of the symmetric stretching, the correlation energy of the system increases as the bond is stretched. As R is increased, the discrepancy between CCSD(T) and DMRG tends to increase. For $R > 2.4$, CCSD(T) failed to converge as reported in Ref. [5]. Our QMC/UHF numbers are in good agreement with DMRG results. The largest discrepancy is about 5 mHa for $R = 3.2$ and $R = 3.6$ bohr. With the asymmetric bond stretching, the RHF trial wave function dissociates properly as R is increased. In this case, CCSD(T) yields results in good agreement with DMRG values. Our QMC energies are also in good agreement with the DMRG values, and the difference between the QMC energies and DMRG is less than $\approx 2 - 3$ mHa.

Bond stretching provides a difficult test for approximate correlated methods. No general method has demonstrated the ability to consistently maintain uniformly high accuracy away from equilibrium. Correlated methods often rely on a trial wave function or on a reference state from which to project the desired solution. While the UHF solution gives a qualitatively correct description of the system in the equilibrium state and in the dissociation limit, in the intermediate region quasi-degeneracies represent a situation analogous to the metal-insulator transition. Thus coupled cluster methods such as CCSD(T), which do remarkably well in describing the equilibrium properties, are less successful in describing systems with quasi-degeneracies such as the case in the breaking of chemical bonds. The present AF QMC results are thus encouraging.

Acknowledgments: Supported by ONR, NSF, DOE CMSN, and ARO.

-
- [1] S. Zhang and H. Krakauer, Phys. Rev. Lett. **90**, 136401 (2003).
[2] W. A. Al-Saidi, S. Zhang, and H. Krakauer, J. Chem. Phys. **124**, 224101(2006).
[3] Garnet Kin-Lic Chan, Nihaly Kallay, and Jürgen Gauss, J. Chem. Phys. **121**, 6110 (2004).
[4] T. H. Dunning, Jr., J. Chem. Phys. **90**, 1007 (1989).
[5] J. Hachmann, W. Gardoén, and G. K-L. Chan, J. Chem. Phys. **125**, 144101 (2006).

First-principles study of electric-field-induced domain evolution in ferroelectric ultrathin films

Bo-Kuai Lai, I. Ponomareva, I. I. Kornev, L. Bellaiche and G. J. Salamo
Physics Department, University of Arkansas, Fayetteville, Arkansas 72701

Ferroelectric thin films are the heart of many applications such as non-volatile memories, communication devices, and microactuators. [1] When experiencing some specific mechanical and electrical boundary conditions, these films can form varieties of domain patterns. Recent experimental results indicate that 180° stripe domains in ferroelectric ultrathin films are rather periodic and have a domain width that can be as small as a few unit cells. Interestingly, the morphology of such nanostripe patterns seem to dramatically depend on the materials: the 180° nanostripes in (001) $\text{Pb}(\text{Zr,Ti})\text{O}_3$ (PZT) and PbTiO_3 thin films [2-4] are known to alternate along the [010] direction while Ref. 5 predicts that such stripes in (001) BaTiO_3 (BTO) ultrathin films alternate along another direction, namely, along [1-10]. The exact reason behind such difference remains to be addressed. The aims of the present study are to use first-principles-based techniques to i) provide atomistic details of domains in BTO ultrathin films; ii) indicate how such domains evolve as a function of applied electric field; iii) compare the properties of BTO ultrathin films with those of PZT ultrathin films, as well as, to discuss and understand their similarities and differences.

Under zero field, it is found that nanostripes in BTO ultrathin films do alternate along [1-10] (as consistent with Ref. 5) while they are known to alternate along [010] in compressively-strained PZT and PbTiO_3 ultrathin films. This difference is traced back to the different balance between dipole-dipole interactions and short-range energies in BTO versus PZT thin films. Moreover, no in-plane dipoles exist at the surface of BTO films, unlike what was predicted in PZT two-dimensional objects – mostly because of energy terms related to the coupling between strain and dipoles. (Dipoles can deviate from the [001] direction by “only” up to 45 degrees at the surfaces of the BTO films).

When applying and increasing an electric field along [001], the evolution of the 180° stripe domains in the BaTiO_3 systems, shown in Figure 1, involves four regions: Region I (Figs. 1a and 1b) for which the magnitude of the “down” dipoles (i.e., those that are antiparallel to the electric field) is reduced, while the domain walls do not move; Region II (Fig. 1c) in which some local down dipoles adjacent to domain walls switch their direction, resulting in zigzagged domain walls – with the overall stripe periodicity being unchanged; Region III (Figs. 1d and 1e) in which nanobubbles are created, then contract along [110] and finally collapse; and Region IV (Fig. 1f) which is associated with a single monodomain. Such evolution differs from that of PZT ultrathin films for which neither Region I nor zigzagged domain walls exist, and for which the bubbles contract along [100]. We hope that our predictions will be confirmed soon, and lead to a deeper knowledge of ferroelectric thin films.

This work is supported by DOE Grant No. DE-FG02-05ER46188, ONR Grants Nos. N00014-04-1-0413 and N00014-01-1-0365 (CPD), and by NSF Grant Nos. DMR-0404335 and DMR-0080054 (C-SPIN). L.B. thanks the twenty-first century professorship in nanotechnology and science education.

- [1] O. Auciello, J. F. Scott and R. Ramesh, *Physics Today* **51**, 22 (1998).
 [2] S. K. Streiffer, J. A. Eastman, D. D. Fong, Carol Thompson, A. Munkholm, M. V. Ramana Murty, O. Auciello, G. R. Bai, and G. B. Stephenson, *Phys. Rev. Lett.* **89**, 067601 (2002).
 [3] I. Kornev, H. Fu and L. Bellaiche, *Phys. Rev. Lett.* **93**, 196104 (2004).
 [4] B.-K. Lai, I. Ponomareva, I. I. Naumov, I. Kornev, H. Fu, L. Bellaiche and G. J. Salamo, *Phys. Rev. Lett.* **96**, 137602 (2006).
 [5] S. Tinte and M. G. Stachiotti, *Phys. Rev. B* **64**, 235403 (2001).

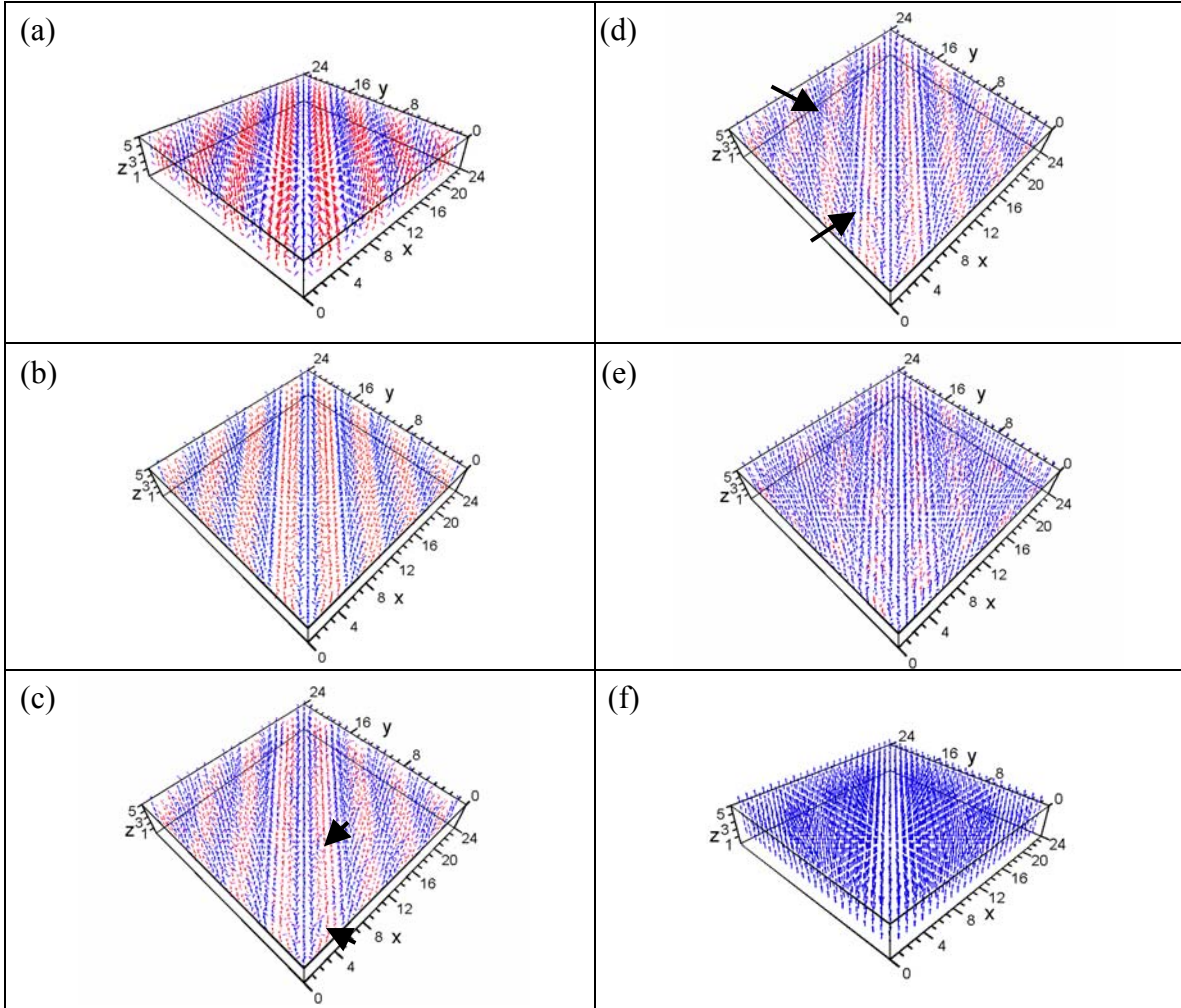


Fig.1. $T=10\text{K}$ three-dimensional polarization patterns in 20 \AA -thick BTO (001) films under a compressive strain of -2.2% and a 80% screening of the maximum depolarizing field, for different external electric field, E_z : stripe domains under (a) $E_z=0$, (b) $E_z=30\times 10^7$ and (c) $E_z=41\times 10^7$ V/m; bubble domains under (d) $E_z=51\times 10^7$ and (e) $E_z=71\times 10^7$ V/m; and monodomain under (f) $E_z=104\times 10^7$ V/m. Blue (red) arrow characterizes local dipoles having a positive (negative) component along the z -axis. The arrows in (c) and (d) indicate some representative switched dipoles (that lead to zigzagged domain walls) and pinching of stripes (that generates nanobubbles), respectively.

Strain-polarization coupling in epitaxial perovskites: A comparison between A-site and B-site driven ferroelectrics

H. N. Lee^{1,*}, S. Nakhmanson^{2,†}, M. F. Chisholm¹, H. M. Christen¹, K. M. Rabe², and D. Vanderbilt

¹Materials Science and Technology Division, Oak Ridge National Laboratory, TN 37831

²Department of Physics and Astronomy, Rutgers University, Piscataway, NJ 08854-8019

[†]Present address: Argonne National Laboratory, Argonne, IL 60439

*E-mail: hnlee@ornl.gov

Biaxial strain induced in epitaxial thin films due to lattice mismatch between the film and the substrate is known to result in highly enhanced ferroelectric and dielectric responses in certain ferroelectric perovskites. Moreover, based on recent experimental observations of high polarization enhancement in BaTiO₃-based heterostructures and superlattices as well as multiferroic BiFeO₃ thin films, it is tempting to assume that such strong sensitivity of physical properties to epitaxial strain is common to all perovskite compounds. However, here we clarify and experimentally verify earlier theoretical predictions that such strong sensitivity of polarization to epitaxial strain is not universal. A comparison of the properties of relaxed (tetragonality $c/a \approx 1.05$) and highly-strained ($c/a \approx 1.09$) PbZr_{0.2}Ti_{0.8}O₃ (PZT) films shows that the polarization is almost independent of epitaxial strain (Fig. 1), while being amongst the highest reported for PZT or PbTiO₃ in either film or bulk forms ($P_r \approx 82 \mu\text{C}/\text{cm}^2$). Such a lack of polarization enhancement is quite striking in a material *praised* for its “strong tetragonal strain-polarization coupling” and high piezoelectric coefficients. Our first-principles calculations (Fig. 2) show that epitaxial strain does not have the same strong effect on the polarization

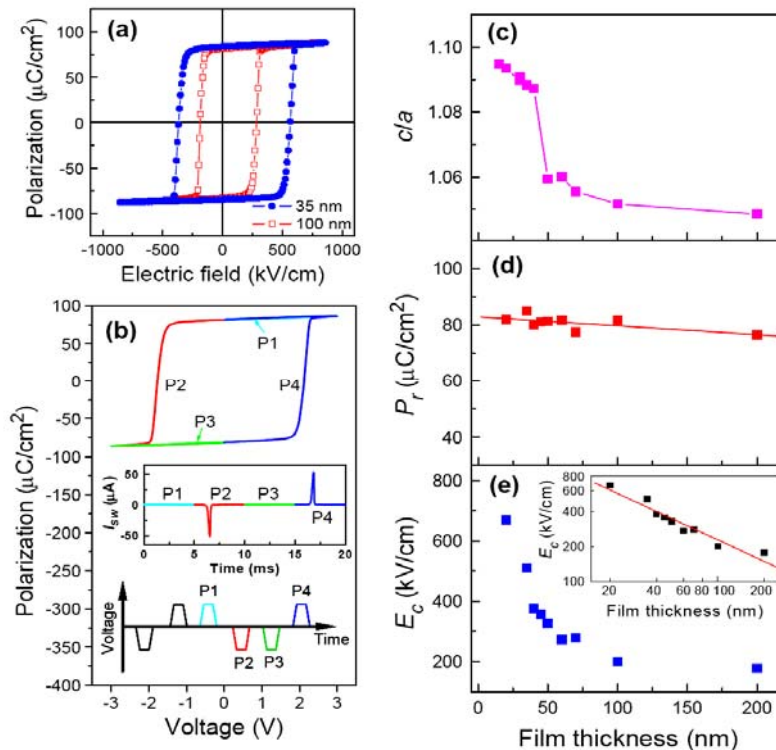


Figure 1. (a) $P(E)$ hysteresis loops at 100 Hz from 35 and 100 nm thick PZT films. (b) Simultaneously-measured pulse polarization and switching current (inset) by applying trapezoid pulses (P1 to P4), showing neither non-switching current nor non-switching polarization. Pulse measurements in (b) were performed at 3 V with 2.5 ms of write/read-pulse time and one second write-pulse delay. Tetragonality (c), remanent polarization (d), and coercive field (e) as a function of film thickness. The slope (-0.61 ± 0.07) in the inset of (e) is in good agreement with the classical scaling behaviour ($E_c \propto d^{2/3}$).

in A-site driven ferroelectrics with already large ferroelectric atomic displacements, such as PZT and PbTiO_3 as it does in less polar B-site driven perovskites, for which it can lead to a substantial polarization increase. In this work, the combined experimental and computational investigations of the coupling between polarization and epitaxial strain in the highest-quality ferroelectric PZT thin films grown by pulsed laser deposition will be presented, showing a suppressed dependence of ferroelectric polarization on epitaxial strain in highly-polar ferroelectric thin films.

Research sponsored by the Division of Materials Sciences and Engineering, Office of Basic Energy Sciences, U.S. Department of Energy, under contract DE-AC05-00OR22725 with Oak Ridge National Laboratory, managed and operated by UT-Battelle, LLC and by the Center for Piezoelectrics by Design (CPD) under ONR Grant N00014-01-1-0365.

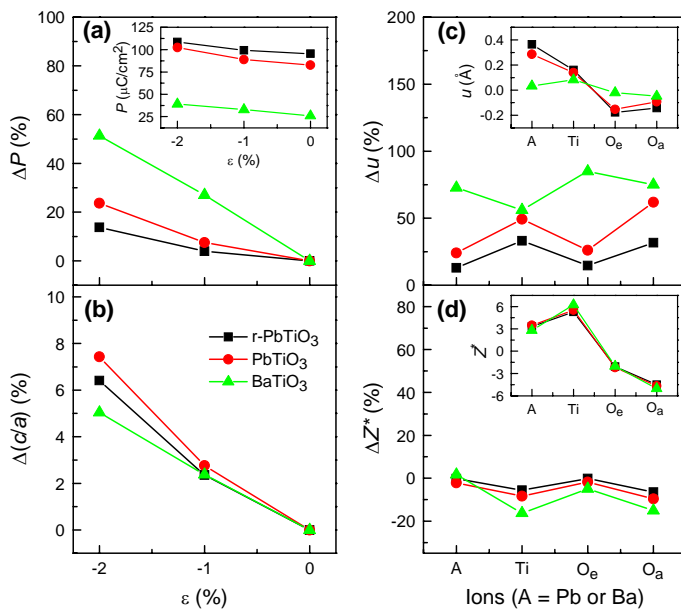


Figure 2. Ferroelectric and structural properties from first-principles calculations. Polarization enhancement (a), tetragonality enhancement (b), and polarization [inset in (a)] as a function of epitaxial strain ϵ in $r\text{-PbTiO}_3$, PbTiO_3 , and BaTiO_3 . The enhancement of ferroelectric displacement (u) and effective charge (Z^*) by epitaxial strain $\epsilon = -2\%$ is shown in (c) and (d), respectively. Insets in (c) and (d) are the values of u and Z^* , respectively, at zero strain. O_e and O_a refer to equatorial and apical oxygens, respectively. Rescaled PbTiO_3 ($r\text{-PbTiO}_3$), whose in-plane lattice constant tuned by hand to match the tetragonality of PZT, is used to mimic the properties of PZT.

First-principles Study and Atomistic Modeling of $(\text{BiScO}_3)_{1-x}-(\text{PbTiO}_3)_x$ Solid Solutions

Yajie Lei^{1,2}, R. E. Cohen², James Lee¹ and Youping Chen³

¹Department of Mechanical and Aerospace Engineering, The George Washington University, Washington, DC 20052

²Carnegie Institute of Washington, Washington, DC 20015

³Department of Mechanical and Aerospace Engineering, University of Florida, Gainesville, Florida 32611

Phone: 202-994-7172; Fax: 202-994-0238; e-mail: yajielei@gwu.edu

The high temperature perovskite ferroelectrics $(\text{BiScO}_3)_{1-x}-(\text{PbTiO}_3)_x$ (BS-PT) solid solutions are drawing more and more attention and extensive investigations since they were identified [1]. The enhanced piezoelectric properties for composition near the morphotropic phase boundary (MPB) ($x = 0.64$) were found to be comparable to soft PZT. The Curie temperature $T_c > 723\text{K}$ is more than 100K higher than in commercial PZT, which makes this material a promising candidate for high temperature and temperature stable actuators and sensors [2-3].

First-principles computations for BS-PT [4] showed large polarizations and responses induced by the hybridization between Bi-6p and O-2p orbitals, as opposed to hybridization of O-2p with B cation d -bands as is typical of most other ferroelectric perovskites. The tetragonal phase of BS shows large strain and deep energy wells with respect to the cubic phase ($c/a = 1.29$ for the tetragonal phase of BS, compared with 1.042 for PT; ΔE_{tet} of BS are one order of magnitude larger than that of PT [5]).

In this work, within local density approximation (LDA), the total energy as function of volume and phonon dispersion relations of the tetragonal and rhombohedral phases were calculated by the ABINIT package [6] for pure BS. The energy as a function of volume shows a large energy difference between the cubic phase and tetragonal one (Fig.1.). For ferroelectric materials, the presence of structural instability can be revealed by the soft phonon modes in the phonon dispersion relations. First principles linear response calculations of the phonon dispersion curves along $(0,0,0) - (0.5,0.5,0.5)$ direction show the unstable phonon modes existing both in the tetragonal phase (Fig.2.a) and in the rhombohedral phase (Fig.2.b), indicating a structural instability of both phases, and suggesting a new phase to be the ground state of BS.

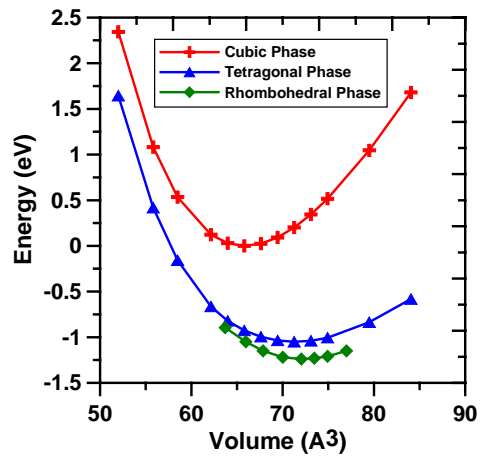


Fig. 1. Total energy as function of volume

In order to extend the first principles studies to finite temperatures and for disordered materials, we are using atomistic modeling based on interatomic potentials fit to first-

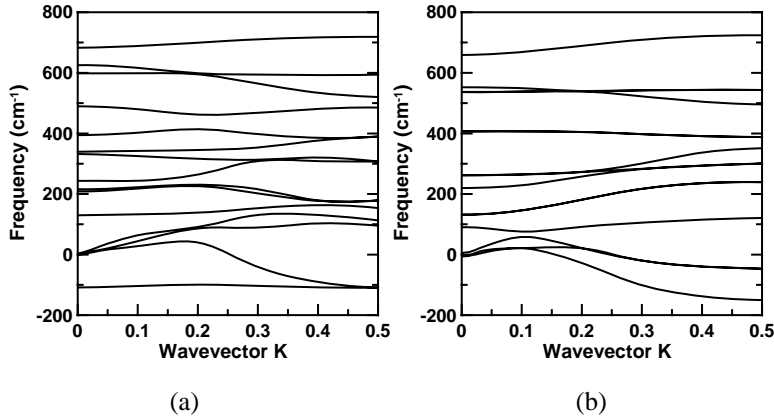


Fig. 2. Phonon dispersion curves of BiScO₃. Imaginary phonon frequencies are represented as negative values. (a) tetragonal phase, (b) rhombohedral phase.

frequencies, dynamical effective charges and dielectric constants are used to fit the potential in the framework of shell model. A combination of the Levenberg-Marquardt method with the singular value decomposition and the method of Nelder-Mead with simulated annealing [7] was employed in the fitting. As the preliminary work of atomistic modeling, the room temperature phase diagram was obtained through MD simulations (Fig. 3.). A rhombohedral to monoclinic MPB was computed over the region $0.60 < x < 0.65$. The large strain and structural instability of BS cause the monoclinic phase to arise and generate MPB in BS-PT solid solution even at zero pressure. Compared with experiment [1], the simulations describe more delicate phase diagram, while the smaller tetragonality at high PT fraction needs to be improved with better potentials.

This work is supported by the National Science Foundation grant CMS-0301539 and CMS-0428419 and Office of Naval Research grant N00014-02-10506 to REC.

principles results. Molecular dynamic (MD) simulations provide atomic-level information, especially showing the advantages for studies of defects, multi-layers and solid solutions. In this work, in order to retain all static and dynamical physical information from first principles calculations, total energies, interatomic forces, stresses, phonon

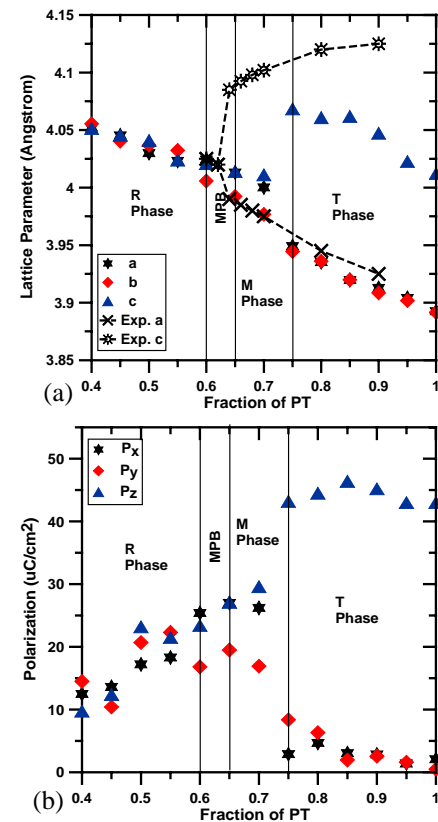


Fig. 3. Room temperature phase diagram. (a) Lattice parameter; (b) Polarization.

1. R. E. Eitel, C. A. Randall, T. R. Shrout, P. W. Rehrig, W. Hackenberger, and S.-E. Park, *Jpn. J. Appl. Phys., Part I* **40**, 5999 (2001); R. E. Eitel, C. A. Randall, T. R. Shrout, and S.-E. Park, *ibid.* **41**, 1(2002).
2. S. Zhang, C. A. Randall and T.R. Shrout, *Appl. Phys. Lett.* **83**, 3150 (2003).
3. R. E. Eitel, S.J. Zhang, T. R. Shrout and C. A. Randall, *J. Appl. Phys.*, **96**, 2828 (2004).
4. J. Iniguez, D. Vanderbilt, and L. Bellaiche, *Phys. Rev. B* **67**, 224107 (2003).
5. Z. Wu and R. E. Cohen, *Phys. Rev. B* **70**, 104112 (2004).
6. The ABINIT code is a common project of the Universite Catholique de Louvain, Corning Incorporated, and other contributors (URL <http://www.abinit.org>).
7. *Numerical Recipes in Fortran 77: The art of scientific computing*, 2nd ed., edited by W. H. Press, S. A. Teukolsky, W. T. Vetterling and B. P. Flannery (Cambridag University Press, 1992).

Thermodynamic stability of ferroelectric lithium niobate surfaces: a theoretical study

Sergey V. Levchenko and Andrew M. Rappe

Makineni Theoretical Laboratories, Department of Chemistry,
University of Pennsylvania, Philadelphia, PA 19104

We present a theoretical study of the thermodynamic stability of the polar (0001) surfaces of ferroelectric lithium niobate LiNbO_3 (LN). We demonstrate that the most stable surfaces are those able to provide surface states to accommodate electrons and holes compensating for the spontaneous polarization and the intrinsic polar stacking termination. The stable electronic surface states are provided by surface oxygen atoms with unsatisfied valency. The low-energy hole surface states are provided by surface cations that are not fully ionized.

We employ plane-wave density functional theory to calculate the electronic structure of LN. Interaction of valence electrons with ionic cores is described by non-local norm-conserving pseudopotentials. Prior to LN calculations, the pseudopotentials were tested by comparison of calculated and experimental lattice parameters and cohesive energies for solid Li, Nb, and Li_2O . The (0001) surfaces of ferroelectric LN are modeled by periodic slab calculations. An example of the unit cell for the slab calculations is shown in Fig. 1. The middle layers

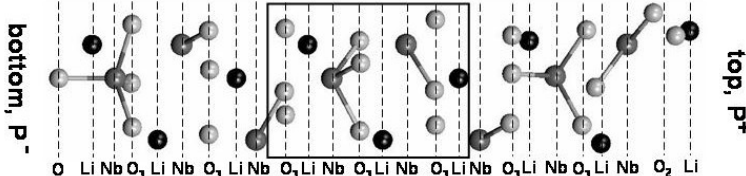


Figure 1: An example of the unit cell for slab calculations of ferroelectric LN. Li (black), Nb (dark grey), and O (light grey) form charge layers (dashed lines) upon periodic repeat in the plane of the slab. This example is the O_2Li top surface and the LiO bottom surface. The c -axis (symmetry axis, horizontal) is perpendicular to the slab surface.

within the black rectangular are fixed at the calculated ferroelectric bulk positions. The rest of both the top and bottom layers are allowed to fully relax. The calculations were converged with respect to the number of fixed layers, the number of layers allowed to relax, and the thickness of the vacuum layer.

Stability of the surfaces is characterized by surface free energy per unit cell defined as

$$\gamma(T, p) = E(N_{\text{Nb}}, N_{\text{Li}}, N_{\text{O}}) - \mu_{\text{Nb}}(T, p)N_{\text{Nb}} - \mu_{\text{Li}}(T, p)N_{\text{Li}} - \mu_{\text{O}}(T, p)N_{\text{O}}$$

where E is the calculated total energy of a slab, μ_i and N_i are chemical potential and number of atoms of element i ($i = \text{Nb}, \text{Li}, \text{O}$), and T and p are temperature and pressure of ambient oxygen. Since the surfaces of a ferroelectric slab are not equivalent, only the sum of the surface free energies can be calculated. The surfaces with smaller free energy are more stable. We compare surface free energies for slabs with different terminations within a range of chemical potentials limited by physical constraints, extending the method used on binary oxides in [1-4] to ternary compounds [5].

Our results clearly demonstrate that accommodation of the surface-charge screening electrons and holes by surface states plays a crucial role in stabilizing certain surface terminations. About one electron per in-plane unit cell is forced to be transferred from one surface to the other by the potential difference created by the stacked alternating layers of anions and cations. Our results suggest that reconstruction and partial coverage should be expected as a result of interplay between thermodynamics and electrostatics in ionic solids.

Fig. 2 shows which surfaces of LN have minimum surface free energy at the given chemical potentials of Li and O. The colored area corresponds to the range of chemical potentials where the solid LN is thermodynamically stable. Only surfaces which gain an electron to screen the electrostatic potential are considered. The stoichiometry of the other surface (losing one electron) is the same for all slabs. The different parts of the colored area correspond to different terminations of the surface. As can be seen in the figure, the LiO -terminated

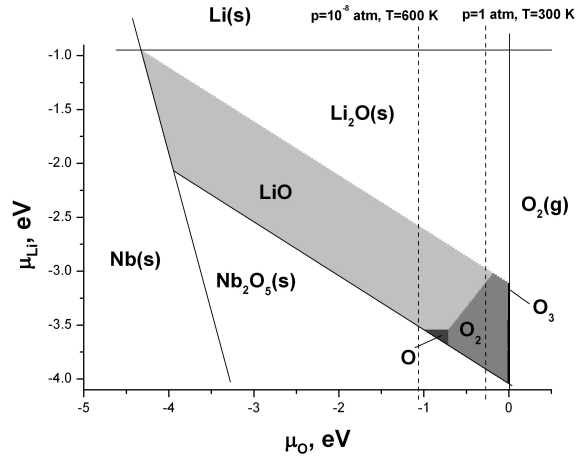


Figure 2: The stable electron-accommodating surfaces of LN. These surfaces are stable because they provide surface states to accommodate about one electron, at the same time allowing the surface species to be in a preferred charged state.

surface is stable in a wide variety of conditions. This can be explained by the fact that the LiO^- species at the surface are stable. However, as the oxygen chemical potential increases (as the oxygen pressure increases and/or temperature decreases), more oxygen precipitates on the surface. Calculated relaxed geometries show that oxygen forms stable O_2^- and O_3^- species rather than a layer of separated oxygen atoms. Similar results were obtained for the surface which loses one electron, as shown in Fig. 3

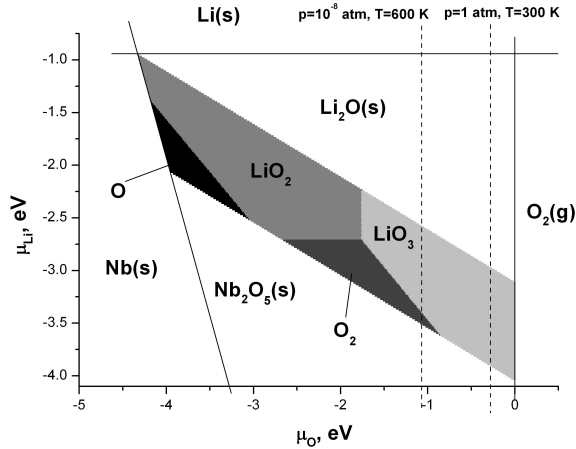


Figure 3: The stable hole-accommodating surfaces of LN. These surfaces are stable because they provide low-lying surface states to accommodate about one hole, at the same time allowing the surface species to be in a preferred charged state.

Using accurate theoretical calculations, we have demonstrated how polarization, polar stacking, and ambient conditions combine to determine surface stoichiometry. We have shown that when the potential created by polarization and polar stacking across the material is compensated by electrons and holes, the most stable surfaces are those which provide low-energy surface states for the compensating charges. The charged species at the surfaces can be stabilized by an appropriate reconstruction.

1. K. Reuter and M. Scheffler, Phys. Rev. B 65, 035406 (2002).
2. K. Reuter and M. Scheffler, Phys. Rev. Lett. 90, 046103 (2003); Phys. Rev. B 68, 045407 (2003).
3. K. Reuter, D. Frenkel, and M. Scheffler, Phys. Rev. Lett. 93, 116105 (2004).
4. C. Stampfl, Catalysis Today 105, 17 (2005).
5. S. J. Jenkins, Phys. Rev. B 70, 245401 (2004).

Ferroelectric instabilities in CaTiO_3 nanoparticles from first principles

Shen Li, Karin M. Rabe

Rutgers University, Piscataway, NJ 08854

Phone: 732-445-4197; e-mail: shenli@physics.rutgers.edu

Ferroelectric instabilities of nanoparticles are expected to be markedly different from those of the constituent bulk material, due to the influence of the particle surface and to characteristic changes in the electrical and mechanical boundary conditions. In many cases, these factors appear to weaken the ferroelectric instability or suppress ferroelectricity altogether [1], although there is no clear reason why this should always be the case [2]. Previous first-principles studies have shown that bulk cubic CaTiO_3 has a strongly polar zone-center instability, which is suppressed by the stronger oxygen octahedron-rotational instabilities, yielding a nonpolar orthorhombic Pbnm ground state [3]. To investigate the possibility that the nanoparticle configuration could weaken or eliminate the octahedron rotation, favoring a ferroelectric state, we performed first-principles calculations for a single-unit-cell cluster, containing one oxygen octahedron, using a real-space pseudopotential density-functional-theory method (PARSEC) [4].

The real-space technique is ideally suited to calculations for finite systems, with no complications introduced by a net charge or dipole moment. The boundary condition is that of zero charge density on the surface of a large sphere enclosing the cluster. The cluster considered here is based on a single perovskite unit cell, which includes 8 Ca, 6 O and one Ti, and has a net charge of +8 to preserve the formal valence (Fig. 1). The cube edge is taken to be equal to the theoretical lattice constant of cubic CaTiO_3 .

To investigate the possibility of a ferroelectric instability, we first moved the Ti atom along a chosen direction while keeping the other atoms fixed.

For an electrically isolated cluster, the symmetric nonpolar state is found to be stable and the dipole moment created by the displacement of the Ti atom is very small. Examination of the charge density indicates that some valence electrons move along with the Ti core as it displaces. The electrons around the oxygen atoms at the surface are almost unchanged. This can be attributed to the high energy cost for an isolated dipole, corresponding to a large depolarization field.

In the laboratory, the depolarization field would be expected to be screened by ambient charges or a conducting matrix for the nanoparticles. In the calculations, we directly compensate the depolarization field by adding an opposite applied field term to the Hamiltonian in the Kohn-Sham equations. The Hamiltonian with depolarization field can be expressed as $H = H_0 - \vec{E}_d \cdot \vec{r}$, where H_0 is the Hamiltonian with zero internal field. So $H_0 = H + \vec{E}_d \cdot \vec{r}$. The depolarization field can be approximated as $\vec{E}_d = \frac{\vec{P}_{dip}}{3\epsilon_0 V}$, where \vec{P}_{dip} is the dipole moment

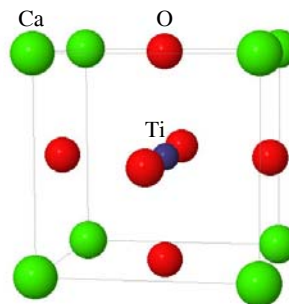


Figure 1: Structure of CaTiO_3 cluster.

and V is the volume of the cluster. Since it is difficult to define the ‘true’ volume of the cluster, we treat it as variable, as a fraction of the large real-space boundary sphere with a factor of α , αV_{sphere} . For each value of α , we solve H_0 self-consistently. The dipole moment \vec{P}_{dip} is calculated from the charge density obtained from the previous loop.

After screening, the plot of the total energy versus the displacement of Ti atom shows a double well when α is smaller than 0.05 (Fig. 2). The effective charge of Ti is 8.7 for $\alpha = 0.049$. Examination of the charge density shows that with screening, fewer electrons move along with the Ti atom; electrons around the oxygen atoms at the surface also move to increase the dipole moment. When $\alpha = 0.049$, 75% of the electrons are included within the sphere of volume αV_{sphere} .

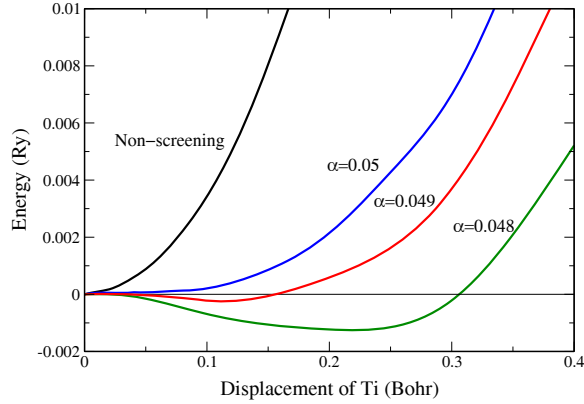


Figure 2: Evolution of the energy as a function of the displacement of Ti.

We also enlarged the lattice constant by 10% along the displacement direction to help stabilize the ferroelectric state. In this case, the ferroelectric instability occurs when α is smaller than 0.067. For $\alpha = 0.067$, the effective charge of Ti is 5.3 and 88% of the electrons are included within the sphere of volume αV_{sphere} .

Our results suggest that for the single-unit-cell CaTiO_3 cluster, a ferroelectric instability could exist under the condition of full compensation of the depolarization field. Our results are consistent with the recent findings regarding the central importance of compensation of the depolarization field in the ferroelectricity of perovskite oxide thin films and nanostructures.

References

- [1] M. E. Lines and A. M. Glass, “Principles and applications of ferroelectrics and related materials” (Clarendon Press, Oxford, 1977).
- [2] P. Ghosez and K. M. Rabe, *Appl. Phys. Lett.* **76**, 2767 (2000).
- [3] E. Cockayne and B. P. Burton, *Phys. Rev. B*, **62**, 3735 (2000).
- [4] J. R. Chelikowsky, N. Troullier and Y. Saad, *Phys. Rev. Lett.* **72**, 1240 (1994); see <http://www.ices.utexas.edu/parsec/>.

Finite-temperature properties of epitaxial BaTiO₃/SrTiO₃ superlattices from first principles

Sergey Lisenkov and L. Bellaïche

Physics Department, University of Arkansas,

Fayetteville, Arkansas 72701, USA

Phone: +1-479-575-5596 ; Fax: +1-479-575-4580 ; e-mail: slisenk@uark.edu

The fabrication of artificial superlattices (SL) consisting of alternating layers of two or more ferroelectric oxides is nowadays possible. In particular, BaTiO₃/SrTiO₃ is the most widely investigated SL in both experiment and theory (see, e.g. Refs. [1–3] and references therein). Such heterostructures may possess properties that dramatically differ from those of bulk ferroelectrics, since, e.g., physical properties of ferroelectric superlattices should be very sensitive to the epitaxial strain arising from the substrate on which the superlattice is grown.

Determining the temperature-misfit strain diagram of superlattices is thus of considerable importance. Here, a first-principles-based effective Hamiltonian approach (that has been recently developed and successfully tested for disordered or ordered Ba_xSr_{1-x}TiO₃ systems [4]) is used within Monte-Carlo simulations to determine such phase diagram in epitaxially strained [BaTiO₃]_n/[SrTiO₃]_n SL having n layers of BaTiO₃ (BT) alternating with n layers of SrTiO₃ (ST) along the [001] direction – which is chosen to be the z axis. We focus on two different superlattice periods, corresponding to $n=2$ [ultrashort SL] and $n=10$ [longer SL]. Moreover, the predictions to be shown below for [BaTiO₃]₂/[SrTiO₃]₂ and [BaTiO₃]₁₀/[SrTiO₃]₁₀ correspond to the use of 12x12x4 (2880 atoms) and 12x12x20 (14400 atoms) periodic supercells, respectively. The epitaxial situations were mimicked by freezing some strain variables, in order to impose that *each* layer in the strained superlattice has the same in-plane lattice constant than the chosen substrate [4].

Figure 1(a) shows our predicted temperature-misfit strain phase diagram for the ultrashort [BaTiO₃]₂/[SrTiO₃]₂ superlattice. The η_{misfit} misfit strain is defined as “ $a_{sub}/a_{BST} - 1$ ”, where a_{sub} is the in-plane lattice constant of the substrate while a_{BST} ($=7.454$ Bohr) is the effective Hamiltonian-predicted lattice constant of *cubic* disordered Ba_{0.5}Sr_{0.5}TiO₃ alloy interpolated down to 0 K. This phase diagram is similar to the one of ultrathin [001] BaTiO₃ thin films under short-circuit-like conditions [5, 6], since it contains a paraelectric phase (denoted as p) at high enough temperature, and three ferroelectric phases having different macroscopic symmetry (but all exhibiting an homogenous polarization): a ferroelectric *tetragonal* phase (denoted by c and for which the polarization is oriented along the growth, z , direction), a ferroelectric *orthorhombic* phase (denoted by aa , and for which the polarization lies along the in-plane [110] direction), and a ferroelectric *monoclinic* phase (that can be further separated into two sub-phases labelled as r_c and r_{aa} , depending if the z -component of the polarization is larger or smaller than its x - and y -components, respectively). Interestingly and as consistent with the previous 0 K first-principles calculations of Refs.[2, 3] for ultrashort superlattices, the polarization in the SrTiO₃ layers is only slightly smaller than the polarization in the BaTiO₃ layers, in this c phase, and the dipoles in the ST layers rotate faster towards [110] than the dipoles in the BT layers in the r_c and r_{aa} phases.

We now turn our attention to the [BaTiO₃]₁₀/[SrTiO₃]₁₀ superlattice, i.e. to the SL having a longer period. Its simulated phase diagram is shown on Fig. 1(b), and dramatically differs from the phase diagram of the ultrashort superlattice because of the existence of domain states. In fact, in addition to the p phase that occurs at high enough tem-

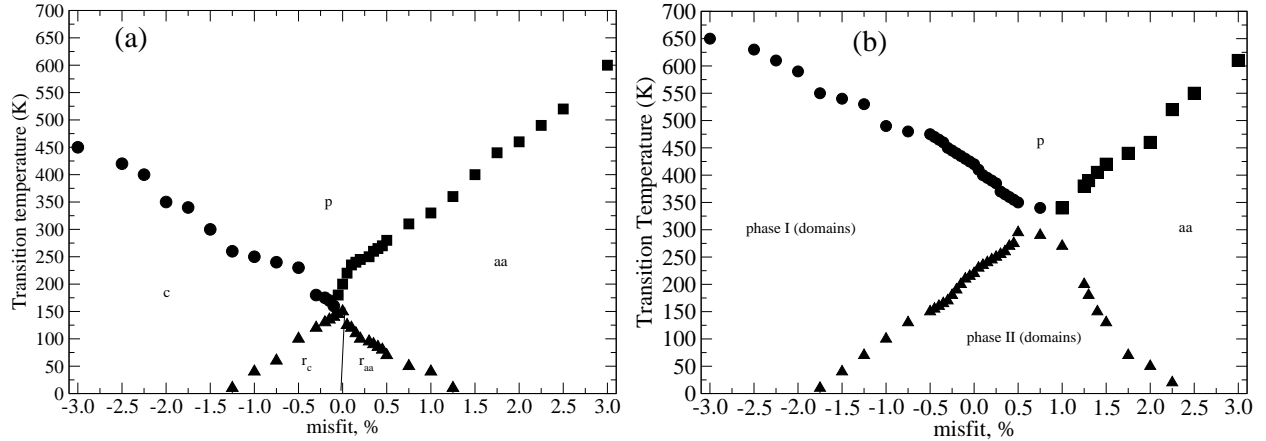


FIG. 1: Temperature-misfit strain phase diagram of the (a) - ultrashort ($n=2$) $[\text{BaTiO}_3]_2/[\text{SrTiO}_3]_2$; (b) - longer ($n=10$) $[\text{BaTiO}_3]_{10}/[\text{SrTiO}_3]_{10}$ superlattices.

perature for any misfit strain, the only state that exists in both $[\text{BaTiO}_3]_2/[\text{SrTiO}_3]_2$ and $[\text{BaTiO}_3]_{10}/[\text{SrTiO}_3]_{10}$ is the orthorhombic aa phase. For a large compressive strain (namely, $\eta_{\text{misfit}} \leq -2.00\%$), the $[\text{BaTiO}_3]_{10}/[\text{SrTiO}_3]_{10}$ superlattice undergoes a single phase transition from the p state to a state denoted as phase I, below a critical temperature. This phase I consists of 180° periodic nanostripes – i.e., with dipoles mostly aligned along the $+z$ or $-z$ direction – alternating along the $[1\bar{1}0]$ direction, and does not exhibit any macroscopic polarization. Phase I thus bears resemblance with the domain state found in compressed $[001]$ BaTiO_3 thin film under open-like electrical boundary conditions [7]. For temperature below 300 K, decreasing η_{misfit} from -2.0% towards positive value results in the occurrence of a state denoted as phase II and which is a domain state that has never been reported in ferroelectrics (to the best of our knowledge). More precisely, phase II still exhibits 180° periodic nanostripes (for their z -dipoles) alternating along the $[1\bar{1}0]$ direction, as in phase I. However, unlike in phase I, a spontaneous polarization also develops along $[110]$ in phase II, that is along an *in-plane* direction that is *perpendicular* to the direction of alternance of the stripes for the z -dipoles. This in-plane polarization mostly originates from the ST layers. Phase II occurs in $[\text{BaTiO}_3]_{10}/[\text{SrTiO}_3]_{10}$ up to a tensile strain of $\simeq 2.25\%$ (see Fig. 1(b)). Further increasing η_{misfit} leads to the disappearance of z -domains in favor of the aa phase in which all dipoles point along $[110]$.

If time allows, we will also report and discuss the unusual evolution of phases I and II when the SL is under an external electric field.

This work is supported by ONR grants N00014-01-1-0365, N00014-04-1-0413 and N00014-01-1-0600, by NSF grant DMR-0404335, and by DOE grant DE-FG02-05ER46188.

-
- [1] A. Jiang, J. Scott, H. Lu, and Z. Chen, J. Appl. Phys. **93**, 1180 (2003).
 - [2] J. Neaton and K. Rabe, Appl. Phys. Lett. **82**, 1586 (2003).
 - [3] K. Johnston, X. Huang, J. Neaton, and K. Rabe, Phys. Rev. B **71**, 100103(R) (2005).
 - [4] L. Walizer, S. Lisenkov, and L. Bellaiche, Phys. Rev. B **73**, 144105 (2006).
 - [5] B.-K. Lai, I. Kornev, L. Bellaiche, and G. Salamo, Appl. Phys. Lett. **86**, 132904 (2005).
 - [6] O. Dieguez, S. Tinte, A. Antons, C. Bungaro, J. B. Neaton, K. Rabe, and D. Vanderbilt, Phys. Rev. B **69**, 212101 (2004).
 - [7] S. Tinte and M. G. Stachiotti, Phys. Rev. B **64**, 235403 (2001).

Investigation of BaTiO₃ Nanowires from First Principles

L. Louis¹, I. Ponomareva¹, L. Bellaiche¹, W. Ma³, P. Gmeiner², B. Dkhil², G. Geneste²

¹*Physics Department, University of Arkansas, Fayetteville AR 72701*

²*Laboratoire Structure, Propriétés et Modélisation des Solides, Ecole Centrale Paris, CNRS-UM8580, Grande Voie des Vignes 92295, Chatenay-Malabry Cedex, France*

³*Ceramic Laboratory, Swiss Federal Institute of Technology (EPFL), CH-1015 Lausanne, Switzerland*

Barium titanate (BaTiO₃) nanowires are investigated using a first-principle-based effective Hamiltonian approach. The purpose of this work is to predict the structural phase transitions occurring in these systems and to determine any size dependency.

The simulated nanowires are stress-free and under short-circuit electrical boundary conditions. Two different kinds of studies are performed. First of all, the nanowires are cooled down from high temperature to 5K. Secondly, the same systems are subjected to a 1.7×10^9 V/m electric field applied along the [111] direction at 5K, and then upon the removal of the field the samples are heated up to 500K – 700K (depending on the system's size).

These two different kinds of study lead to different phase diagrams! More precisely, cooling down the sample generates the following phase transition sequence (as the temperature decreases): paraelectric state – ferroelectric orthorhombic state 1 -- ferroelectric orthorhombic state 2 -- ferroelectric orthorhombic state 3 exhibiting domains. On the other hand, the second study generates the following transition sequence: paraelectric state – ferroelectric orthorhombic state 1 -- ferroelectric orthorhombic state 2 -- ferroelectric *monoclinic* state. In other words, these two kinds of study reveal that BaTiO₃ nanowires contain at least two energetically close minima at low temperature: one that favors a domain configuration (see Fig. 1a) and another one favoring a more homogeneous monoclinic state (see Fig. 1b). They also reveal that the phase diagram of BaTiO₃ nanowires differs from that of BaTiO₃ bulk. A discussion will be provided to explain these findings.

We will also present the size dependency of the transition temperatures, and compare our predictions with preliminary experimental results.

This work is supported by ONR Grants Nos. N00014-01-1-0365 and N00014-04-1-0413, by DOE Grant No. DE-FG02-05ER46188, and by NSF Grants Nos. DMR-0404335 and DMR-0080054.

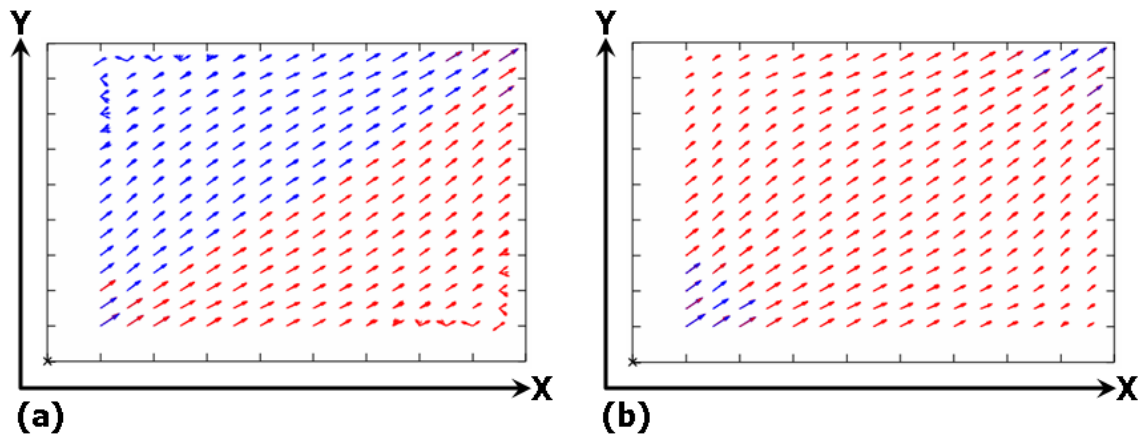


Figure 1: $T = 5\text{K}$ two-dimensional polarization patterns for BaTiO_3 nanowire with $6.4\text{ nm} \times 6.3\text{ nm}$ cross-section. (a) sample is cooled down to 5K (b) second study. Red (blue) arrow characterizes local dipoles having a positive (negative) component along the z -axis.

First-principles study of polarization and piezoelectric properties of $\text{Zn}_{1-x}\text{Mg}_x\text{O}$

Andrei Malashevich and David Vanderbilt

Rutgers University, Piscataway, NJ 08854-8019

Phone: (732) 445-4735; e-mail: andreim@physics.rutgers.edu

Wurtzite ZnO can be substituted with up to $\sim 30\%$ MgO to form a metastable $\text{Zn}_{1-x}\text{Mg}_x\text{O}$ alloy while still retaining the wurtzite structure. Because this alloy has a larger band gap than pure ZnO, $\text{Zn}_{1-x}\text{Mg}_x\text{O}/\text{ZnO}$ quantum wells and superlattices have been much studied recently [1] as promising candidates for applications in optoelectronic and electronic devices.

We report the results of an *ab-initio* study of the spontaneous polarization of $\text{Zn}_{1-x}\text{Mg}_x\text{O}$ alloys as a function of their composition [2]. This is an important property to study, since if an interface occurs between a ZnO region and a $\text{Zn}_{1-x}\text{Mg}_x\text{O}$ region within a superlattice or quantum-well structure, bound charges are expected to appear at the interface. These charges, in turn, will create electric fields that are likely to affect the electrical and optical properties of the quantum well devices.

In this work we consider six models of $\text{Zn}_{1-x}\text{Mg}_x\text{O}$ with different magnesium concentrations (up to 50%). Calculations of the crystal structure are based on density-functional theory in the local-density approximation, and the polarization is calculated using the Berry-phase approach [3]. We decompose the changes in polarization into purely electronic, lattice-displacement mediated, and strain mediated components. We consider both free-stress and epitaxial-strain elastic boundary conditions. In Table 1, we give the results of calculation of polarization, and the results of decomposition of polarization are given in Table 2.

	x	P_{free}	P_{epit}	$P_{\text{epit}}^{\text{est}}$
ZnO	0.0	-0.0322	-0.0322	
Model 1	0.17	-0.0423	-0.0277	-0.0279
Model 2	0.25	-0.0501	-0.0247	-0.0247
Model 3	0.25	-0.0470	-0.0244	-0.0250
Model 4	0.33	-0.0565	-0.0230	-0.0239
Model 5	0.5	-0.0789	-0.0199	-0.0222
Model 6	0.5	-0.0699	-0.0202	-0.0225

Table 1: Calculated values of total polarizations of $\text{Zn}_{1-x}\text{Mg}_x\text{O}$ alloy models (C/m^2). Subscript ‘free’ indicates zero-stress elastic boundary conditions, while ‘epit’ indicates that a is constrained to be identical to that of bulk ZnO. Superscript ‘est’ indicates value estimated by the model of Eq. (1).

	x	ΔP_{elec}	ΔP_{ion}	ΔP_{piezo}	ΔP_{tot}
ZnO	0.0	0.0	0.0	0.0	0.0
Model 1	0.17	0.0001	-0.0022	-0.0081	-0.0101
Model 2	0.25	0.0018	-0.0023	-0.0175	-0.0180
Model 3	0.25	0.0000	-0.0027	-0.0122	-0.0148
Model 4	0.33	0.0009	-0.0038	-0.0214	-0.0243
Model 5	0.5	0.0023	-0.0063	-0.0427	-0.0467
Model 6	0.5	-0.0019	-0.0062	-0.0296	-0.0377

Table 2: Theoretical values of electronic, ionic, piezoelectric and total contributions to polarization (C/m²) for each model, relative to bulk ZnO.

Our results indicate a roughly linear dependence of spontaneous polarization on Mg concentration, although the sign of the linear coefficient is opposite in the free-stress and epitaxial-strain cases. We also found that the strain mediated component of the polarization is dominant. This means that the change in polarization is mostly governed by piezoelectric effects connected with the x -dependent changes of the a and c lattice constants. We also show that many of the polarization-related properties of the Zn_{1- x} Mg $_x$ O alloy can be estimated by using a model based on the piezoelectric effect alone. For example, one might hope that $\delta P = P_{\text{epit}} - P_{\text{free}}$, the difference between the epitaxially constrained and free-stress polarizations at a given x , could be estimated by a linear approximation of the form

$$\delta P = 2e_{31} \frac{a_{\text{epit}} - a_{\text{free}}}{a_{\text{free}}} + e_{33} \frac{c_{\text{epit}} - c_{\text{free}}}{c_{\text{free}}}. \quad (1)$$

In fact, we find that this is the case even if we use the piezoelectric constants of bulk ZnO. The results of this approximation are also given in Table 1.

References:

- [1] A. Ohtomo *et. al.* Appl. Phys. Lett. **72**, 2466 (1998).
- [2] A. Malashevich and D. Vanderbilt, Phys. Rev. B **75**, 045106 (2007).
- [3] R. D. King-Smith and D. Vanderbilt, Phys. Rev. B **47**, 1651 (1993).

Nearest B-Neighbor Effects on B-site Electric Field Gradients in Perovskites

D. Mao, E. J. Walter, and H. Krakauer

Department of Physics, College of William and Mary, Williamsburg, VA 23187-8795.
Phone: 757-221-3552; Fax: 757-221-3540; e-mail: dxmao@wm.edu

Piezoelectric and dielectric properties of Pb-based complex ferroelectric alloys with the $A(B'B''B''')O_3$ perovskite structure depend on the composition and the local ordering of the B-site cations. For example, $Pb(Sc_{1/2}Ta_{1/2})O_3$ (PST) is a normal ferroelectric when the B atoms are ordered and becomes a relaxor when they are disordered. By contrast, disordered $Pb(Zr_{1-x}Ti_x)O_3$ (PZT) is a normal ferroelectric. As a good probe of the local structure, electric field gradients (EFG) are very sensitive to variations in chemical environments, and they can be measured using high-field nuclear magnetic resonance experiments.

We examined PST and PZT(50/50) supercells with [001]1:1 B-site ordering, imposing Cm and $P4mm$ symmetries, as well as [111]1:1 B-site ordering with $R3m$ imposed symmetry. PZT contains homovalent Zr^{4+} and Ti^{4+} B cations, while PST has heterovalent Sc^{3+} and Ta^{5+} B cations. We also studied two 30-atom PSW supercells and a 60-atom PMN supercell both based on the ‘‘random site’’ model [1]. Calculations of EFGs are presented using the LAPW method [2] within the local density approximation. The volumes of all supercells are fixed at the experimental volume, but the atomic positions are relaxed.

Our computed pair distribution functions (PDF) [3] of PZT and PST supercells agree very well with the experimental results of Dmowski *et al.* [4, 5]. Calculated EFG’s for B atoms in [001]1:1 and [111]1:1 ordered PZT and PST supercells are presented in Table I, as well as their off-centering against the oxygen octahedra. In both PZT and PST, EFGs of the heavier and more polarizable atoms, Zr and Ta, are larger in magnitude compared to Ti and Sc. The Ta EFG’s are especially large among all the B atoms. Fig. 1 displays B cation EFGs of [001]1:1 PZT and PST with imposed Cm and $P4mm$ symmetries, as a function of c/a . For six-fold coordination, the ionic radii of Zr^{4+} in PZT and Sc^{3+} in PST are 0.72\AA and 0.745\AA respectively, and the EFGs of these two cations are similar in both magnitude and behavior as c/a changes. The ionic radii of Ti^{4+} in PZT and Ta^{5+} in PST are 0.605\AA and 0.64\AA respectively, smaller than Zr and Sc. Although their EFG values are very different, Ti and Ta both have large anisotropy parameter $\eta \sim 0.6$. Table I also shows that all B atoms experience their smallest V_{zz} value in the [111]1:1 ordering supercells with $R3m$ symmetry imposed. In such rocksalt structures, every B atom is surrounded symmetrically by six B’ atoms. However, little correlation is seen between the B atom off-centerings and their EFG’s based on our results.

Calculated B-atom EFGs for the PSW 30-atom random site model supercells are listed in Table II. Depending on

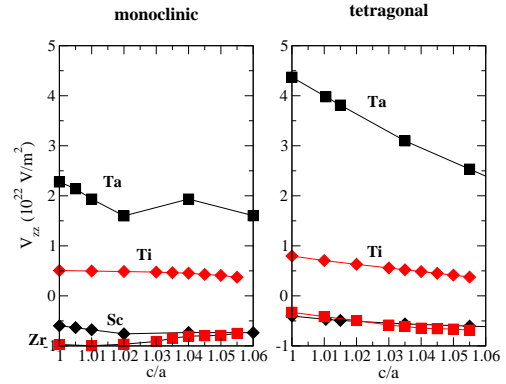


FIG. 1: Calculated V_{zz} as a function of c/a for [001]1:1 ordered PZT and PST with imposed Cm and $P4mm$ symmetries. The black squares are for Ta, black diamonds for Sc, red squares for Zr, and red diamonds for Ti.

TABLE I: Calculated EFGs (V_{zz}) in units of $10^{22}V/m^2$ and the off-centering (δ_{off}) with respect to surrounding oxygen octahedra for monoclinic, tetragonal, and rhombohedral PZT and PST. For PZT, we used $c/a = 1.02, 1.045, \text{ and } 1.00$ for monoclinic, tetragonal, and rhombohedral, respectively. For PST, $c/a = 1.00, 1.055, \text{ and } 1.00$ were used, respectively. R_i is the six-coordinated ionic radius of each atom, and NN is the number of the nearest B neighbors.

	[001] monoclinic					[001] tetragonal				[111] rhombohedral			
	$R_i(\text{\AA})$	V_{zz}	η	NN(Zr/Ti)	$\delta_{off}(\text{\AA})$	V_{zz}	η	NN(Zr/Ti)	$\delta_{off}(\text{\AA})$	V_{zz}	η	NN(Zr/Ti)	$\delta_{off}(\text{\AA})$
Zr/PZT	0.72	-0.967	0.040	4/2	0.312	-0.656	0.000	4/2	0.387	-0.393	0.000	0/6	0.237
Ti/PZT	0.605	0.486	0.679	2/4	0.285	0.450	0.000	2/4	0.225	-0.229	0.000	6/0	0.239
	$R_i(\text{\AA})$	V_{zz}	η	NN(Sc/Ta)	$\delta_{off}(\text{\AA})$	V_{zz}	η	NN(Sc/Ta)	$\delta_{off}(\text{\AA})$	V_{zz}	η	NN(Sc/Ta)	$\delta_{off}(\text{\AA})$
Sc/PST	0.745	-0.598	0.343	4/2	0.207	-0.605	0.000	4/2	0.298	-0.159	0.000	0/6	0.234
Ta/PST	0.64	2.276	0.628	2/4	0.268	2.534	0.000	2/4	0.190	-0.934	0.000	6/0	0.214

TABLE II: Same as Table I for Sc and W atoms in two PSW 30-atom supercells.

Atom	$R_i(\text{\AA})$	V_{zz}	Imm4			Immm			
			η	NN(Sc/W)	$\delta_{\text{off}}(\text{\AA})$	V_{zz}	η	NN(Sc/W)	$\delta_{\text{off}}(\text{\AA})$
Sc ₁	0.745	-0.238	0.758	6/0	0.189	-0.244	0.329	6/0	0.231
Sc ₂	0.745	-0.805	0.100	4/2	0.167	-0.307	0.372	2/4	0.186
Sc ₃	0.745	0.479	0.428	1/5	0.238	-0.312	0.587	2/4	0.204
Sc ₄	0.745	0.459	0.385	1/5	0.203	0.619	0.319	2/4	0.256
W ₁	0.60	-0.725	0.609	6/0	0.194	0.726	0.724	6/0	0.158
W ₂	0.60	1.151	0.789	6/0	0.144	0.618	0.817	6/0	0.150

TABLE III: Same as Table I for Nb and Mg atoms in the PMN 60-atom unit cell.

Atom	$R_i(\text{\AA})$	V_{zz}	η	NN(Mg/Nb)	$\delta_{\text{off}}(\text{\AA})$
Nb ₁	0.64	-1.089	0.872	3/3	0.157
Nb ₂	0.64	0.483	0.458	1/5	0.219
Nb ₃	0.64	-0.825	0.742	3/3	0.281
Nb ₄	0.64	-0.861	0.132	5/1	0.185
Nb ₅	0.64	-0.790	0.181	5/1	0.190
Nb ₆	0.64	-0.814	0.527	3/3	0.270
Nb ₇	0.64	0.421	0.561	1/5	0.199
Nb ₈	0.64	-1.091	0.847	3/3	0.205
Mg ₁	0.72	-0.394	0.530	0/6	0.172
Mg ₂	0.72	0.454	0.834	0/6	0.109
Mg ₃	0.72	-0.388	0.710	0/6	0.099
Mg ₄	0.72	-0.400	0.512	0/6	0.177

the different arrangements of the Sc and W atoms in the mixed layer, the supercell can have various symmetries like *Immm* and *Imm4* when all atoms are at their ideal cubic positions. We relaxed these two types of structures to *P1* symmetry, but in Table II, they are still referred as *Immm* and *Imm4* supercells. In PSW, W atoms always have 6 Sc as their nearest neighbor B-atoms (nnB), while Sc nnB configurations are more varied. Like the B atoms in PZT and PST, Sc atoms in PSW also have the smallest EFG's when surrounded by the most isotropic B shell (all Sc nnB's), and the Sc EFG's increase as the nnB shell becomes more anisotropic. Furthermore, Sc atoms with a W-rich nnB shell tend to have smaller EFGs than those with Sc-rich nnB's. And we note that the similarity of the EFG's of W in PSW and Ta in *R3m* PST correlates with their similar rocksalt-like nnB environments and ionic radii.

Table III presents the B-atom EFGs of various nnB configurations in a 60-atom "random-site" PMN supercell given by Grinberg and Rappe [6]. Similar to the cations with smaller ionic radii in PST and PSW, Nb⁵⁺ in PMN also possess larger EFGs than Mg²⁺. Like Sc atoms in PSW, Nb atoms in PMN with 5 Nb's and 1 Mg nnB have the smallest EFGs, and the EFGs of those with 5 Mg's and 1 Nb nnB are much larger. This Nb sensitivity to the nnB has also been observed in a NMR experiment on PMN powder sample by Zhou *et al.* [7].

Our results indicate that the heavy atoms with smaller ionic radii tend to have larger EFGs in perovskites. And the EFGs of the B atoms are very sensitive to their nearest neighbor B environment. The isotropic B shell always results in the smallest EFG of the centered atom. When surrounded by more B neighbors with smaller ionic radii, the centered atom has smaller EFGs. On the other hand, in all the solid solutions we studied, there seems to be little direct relationship between the B atom EFGs and their off-centerings.

Acknowledgments: Supported by ONR. Calculations were performed on Center of Piezoelectric by Design (CPD).

-
- [1] P. K. Davies and M. A. Akbas, *J. Phys. Chem. Solids* **61**, 159 (2000).
 - [2] D. Singh, *Planewaves, Pseudopotentials and the LAPW Method* (Kluwer Academic Publishers, 1994).
 - [3] T. Proffen and S. J. L. Billinge, *PDFFIT, a program for full profile structural refinement of the atomic pair distribution function* (1999).
 - [4] W. Dmowski, T. Egami, L. Farber, and P. K. Davies, in *Fundermental Physics of Ferroelectrics* (2001), p. 33.
 - [5] W. Dmowski, M. K. Akbas, P. K. Davies, and T. Egami, *J. Phys. Chem. Solids* **61**, 229 (2000).
 - [6] I. Grinberg and A. M. Rappe, *Phys. Rev. B* **70**, 220101 (2004), and private communication.
 - [7] D. H. Zhou, G. L. Hoatson, and R. L. Vold, *J. Magn. Reson.* **167**, 242 (2004).